Helsinki University of Technology
Low Temperature Laboratory
Espoo 2005

QUANTUM DEVICE APPLICATIONS OF MESOSCOPIC SUPERCONDUCTIVITY

Mika Sillanpää

Dissertation for the degree of Doctor of Science in Technology to be presented with due permission of the Department of Engineering Physics and Mathematics for public examination and debate in Auditorium F1 at Helsinki University of Technology (Espoo, Finland) on the 1st of April, 2005, at 12 o'clock noon.

Helsinki University of Technology
Department of Engineering Physics and Mathematics
Low Temperature Laboratory

Teknillinen korkeakoulu
Teknillisen fysiikan ja matematiikan osasto
Kylmälaboratorio

Distribution:
Helsinki University of Technology
Low Temperature Laboratory
P.O. Box 2200
FIN-02015 HUT
Tel. +358-9-451-4909
Fax. +358-9-451-2969
E-mail: Mika.Sillanpaa@iki.fi
This dissertation can be read at http://lib.hut.fi/Diss/

ISBN 951-22-7567-8
ISBN 951-22-7568-6 (pdf)

Otamedia Oy
Espoo 2005

HELSINKI UNIVERSITY OF TECHNOLOGY P.O. BOX 1000, FIN-02015 HUT http://www.hut.fi	ABSTRACT OF DOCTORAL DISSERTATION

Author Sillanpää, Mika Antero

Name of the dissertation

Quantum device applications of mesoscopic superconductivity

Date of manuscript 14.12.2004	Date of the dissertation April 1st 2005
☐ Monograph	☑ Article dissertation (summary + original articles)

Department	Department of Engineering Physics and Mathematics
Laboratory	Low Temperature Laboratory
Field of research	Experimental condensed-matter physics
Opponent(s)	Prof. Hans Mooij
Supervisor	Prof. Martti M. Salomaa
(Instructor)	Prof. Pertti J. Hakonen

Abstract

The work involves a study of physical phenomena that take place at very small length scales, below one micro-meter. At temperatures roughly below one degree Kelvin, quantum-mechanical effects may rule in electronic transport. Macroscopic quantum-coherent effects that occur in metallic superconducting microstructures, are particularly intriguing. Large-scale quantum information processing is widely believed to be attainable utilizing such physical systems.

This work concentrates on answering the question of how the described quantum-mechanical systems may be used as sensitive measuring devices. Considerable attention is paid to energy-storing metallic microstructures whose electrical properties resemble those of the familiar inductor or capacitor. This research involves primarily experimental investigations conducted around temperatures of 0.1 Kelvin. Methods both at low and at radio frequencies have been used. The experimental findings have been modelled theoretically, and theoretical concepts for new physical phenomena have been introduced.

An inductively measured radio-frequency Cooper-pair transistor, the L-SET, has been developed and experimentally verified in this work. Being highly sensitive, fast, and non-invasive, the L-SET appears to be the most promising method for measuring electric charge. Sensitivity in charge measurements of 20 millionths of the electron charge (micro-e) within one second, and an input bandwidth of 100 MHz, have been demonstrated. It has been shown theoretically that the ultimate measurement accuracy is about 0.1 micro-e within a second. A new phase detector based on the Cooper-pair transistor has been proposed. This system has also been shown to be potentially usable as a quantum bit. A new type of radio-frequency single-electron transistor built using a multi-walled carbon nanotube has been fabricated and operated.

Technologies have been developed in order to make the physical nano- or microstructures. A method has been presented to fabricate non-superconducting tunnel junctions. Consequences of the inverse superconducting proximity effect on the studied superconducting structures were considered. Measurement procedures were investigated for a new low-noise nanoamplifier, the Bloch-oscillating transistor. Single superconducting tunnel junctions were tested as detectors of energy states of the environment, or of noise.

Keywords High-frequency techniques, single-electron transistor, quantum measurement

UDC	Number of pages 208
ISBN (printed) 951-22-7567-8	ISBN (pdf) 951-22-7568-6
ISBN (others)	ISSN

Publisher Otamedia Oy

Print distribution

☑ The dissertation can be read at http://lib.hut.fi/Diss/

Acknowledgements

LET me first thank my collaborators. I have benefitted from the input of a great number of people and organizations. I cannot individually acknowledge all of you. I have been fortunate to labour in the prestigious Helsinki Low Temperature Laboratory founded by the late academician Olli V. Lounasmaa. It is a pleasure to thank the present director, professor Mikko Paalanen, for the opportunity.

My instructor, professor Pertti Hakonen, guided us with his enthusiastic example and incredible knowhow. I owe much to my smart team Leif Roschier at the nano-rf cryostat. Tero Heikkilä had the theoretical capability to cheer me up a few times.

I have gained much from communication with the following scientific collaborators in the lab: Markus Ahlskog, Anne Anthore, Julien Delahaye, Antti Finne, Jouni Flyktman, Jani Kivioja, Kolja Kopnin, Teijo Lehtinen, René Lindell, Juha Martikainen, Tommi Nieminen, Antti Niskanen, Antti Paila, Ülo Parts, Jari Penttilä, Jukka Pekola, Sasha Savin, Eduard Sonin, Reeta Tarkiainen, Erkki Thuneberg, Jussi Toppari, Janne Viljas, Wu Fan, and Takahide Yamaguchi.

Outside the lab, I have benefited and enjoyed communication with Hervé Courtois, Uri Gavish, Sophie Gueron, Juha Hassel, Göran Johansson, Sasha Korotkov, Yuriy Makhlin, Bernard Pannetier, Gerd Schön, Heikki Seppä, Viktor Sibakov, Markku Stenberg, and Jani Tuorila. I thank my supervisor professor Martti Salomaa for comments on the manuscript.

The cooperative effort of the technical staff at the lab is greatly appreciated, most notably that of the workshop, led by Seppo Kaivola, and Arvi Isomäki at the liquifier. I am grateful also to the lab administration, Tuire Koivisto and Pirjo Kinanen in particular. I am pleased to acknowledge the Emil Aaltonen Foundation for a personal grant tailored for young researchers.

Heartfelt thanks to my parents Eila and Heikki!

Otaniemi, December 2004

Mika Sillanpää

List of abbreviations

A	surface area
AC	alternating current
B	bandwidth
BCS	Bardeen-Cooper-Schrieffer theory of superconductivity
BNC, MCX, SMA	types of microwave connectors
BOT	Bloch-oscillating transistor
CSET	quantum capacitive phase detector
CW	continuous wave
C	capacitor or capacitance
C_c	coupling capacitor
C_{eff}	observable quantum capacitance
C_g	gate capacitance
C_Q	quantum capacitance
C_Σ	island capacitance
d	asymmetry of Josephson energies of an SCPT
DC	direct current
DCB	DC-block
DOS	density of states
e	absolute value of electron charge, $e \simeq 1.6022 \times 10^{-19}$ Coulomb
E_0	lowest energy band of an SCPT
E_1	first excited energy band of an SCPT
E_C	charging energy of Cooper-pair transistor, $E_C = e^2/(2C_\Sigma)$
E_{C0}	charging energy of a single junction
E_J	Josephson energy of a single junction
E_J^*	effective Josephson energy of a Cooper-pair transistor
E_L	energy scale of an inductor, $E_L = \Phi_0^2/(8\pi^2 L)$
FWHM	full width at half maximum (of a resonance)
f_0	resonant frequency of an LC oscillator, $f_0 = \omega_0/(2\pi)$
f_p	frequency of the Josephson plasma resonance, $f_p = \omega_p/(2\pi)$
g	transfer function
g_m	the maximum value of transfer function with respect to gate
HP	high pass

h	Planc constant, $h \simeq 6.62608 \times 10^{-34}$ Js
$\hbar$	$h/(2\pi) \simeq 1.0546 \times 10^{-34}$ Js
I_1	current at the drive frequency
I_C	critical current of Josephson junction
I_C^*	effective critical current of an SCPT
IV	current-voltage
JJ	Josephson junction
k_B	Boltzmann constant, $k_B \simeq 1.3807 \times 10^{-23}$ J K^{-1}
L-SET	inductive single-electron transistor
L_J	Josephson inductance of single junction
L_J^*	effective Josephson inductance of SCPT
LO	local oscillator
$L_{\rm tot}$	total inductance of the L-SET
LP	low pass
MAA	methacrylic acid
N	non-superconducting (normal) metal
NIN	normal-insulator-normal (tunnel junction)
PMGI	polydimethylglutarimide
PMMA	polymethyl methacrylate (plexiglass)
P_C	critical power
q	quasicharge of a single JJ
Q	real charge on a capacitor
Q_i	internal quality factor
Q_I	charge of an island
Q_L	loaded quality factor
q_g	gate charge, $q_g = C_g V_g/e$
R	resistance in general
RF	radio frequency
RF-SET	radio-frequency single-electron transistor
RMS	root-mean-square
RT	room temperature
R_K	quantum resistance, $R_K = h/e^2 \simeq 25.8$ kΩ
R_Q	quantum resistance of Cooper pairs, $R_Q = h/(4e^2) \simeq 6.45$ kΩ
R_{SET}	effective quasiparticle resistance of a SET
R_T	tunneling resistance of a single junction
SCPT	single Cooper-pair transistor
SEM	scanning electron microscope
SET	single-electron transistor
SIS	superconductor-insulator-superconductor junction
SM	surface mount

SNR	amplitude signal-to-noise ratio
SS	stainless steel
s_q	charge sensitivity
SQUID	superconducting quantum interference device
s_φ	phase sensitivity
T	temperature in general
T_N	amplifier noise temperature
UHV	ultra high vacuum
V	voltage in general
V_1	voltage amplitude at the drive frequency
V_B	bias voltage
V_{CV}	critical voltage amplitude of a JJ, for voltage bias
V_{CI}	critical voltage amplitude of a JJ, for current bias
V_g	gate voltage
V_{in}	amplitude of an incoming voltage wave
V_I	island voltage amplitude
V_{out}	amplitude of an outgoing voltage wave
V_R	voltage amplitude over a parallel resonator
V_S	switching voltage amplitude, at the first maximum of Z_1
Z	impedance in general (also impedance of the L-SET)
ZEP	chloromethacrylate and -methylstyrene
Z_0	transmission line impedance, $Z_0 = 50\,\Omega$
Z_1	impedance of a JJ at drive frequency
Z_R	impedance of a parallel resonator
β_0	current gain
Γ	microwave voltage reflection coefficient
Δ	superconductor energy gap
ε_0	permittivity of vacuum $\varepsilon_0 \simeq 8.8542 \times 10^{-12}$ F m^{-1}
ε_r	relative permittivity
θ	SCPT island phase
Θ	qubit mixing angle
ξ_S	superconductor coherence length in the dirty limit
τ	time constant
Φ	magnetic flux
Φ_0	quantum of magnetic flux, $\Phi_0 = h/(2e) \simeq 2.0678 \times 10^{-15}$ Wb
φ	phase of the superconductor order parameter
ω_{01}	qubit level spacing, $\hbar\omega_{01} = E_1 - E_0$

Appended papers

This thesis is based on the following eleven original publications.

[P1] M. A. Sillanpää, T. T. Heikkilä, R. K. Lindell, and P. J. Hakonen, *Inverse proximity effect in superconductors near ferromagnetic material*, Europhysics Letters **56**, 590 (2001).

[P2] M. A. Sillanpää and P. J. Hakonen, *Titanium single-electron transistor fabricated by electron-beam lithography*, Physica E **15**, 41 (2002).

[P3] J. Delahaye, J. Hassel, R. Lindell, M. Sillanpää, M. Paalanen, H. Seppä, and P. Hakonen, *Low-Noise Current Amplifier Based on Mesoscopic Josephson Junction*, Science **299**, 1045 (2002).

[P4] R. Lindell, J. Penttilä, M. Sillanpää, and P. Hakonen, *Quantum states of a mesoscopic SQUID measured using a small Josephson junction*, Physical Review B **68**, 052506 (2003).

[P5] L. Roschier, M. Sillanpää, T. Wang, M. Ahlskog, S. Iijima, and P. Hakonen, *Carbon Nanotube Radio-Frequency Single-Electron Transistor*, Journal of Low Temperature Physics **136**, 465 (2004).

[P6] M. A. Sillanpää, L. Roschier, and P. J. Hakonen, *Inductive Single-Electron Transistor*, Physical Review Letters **93**, 066805 (2004).

[P7] M. A. Sillanpää, L. Roschier, and P. J. Hakonen, *Dynamics of the Inductive Single-Electron Transistor*, to appear in "Quantum information and Decoherence in Nanosystems", proceedings of the Vth Rencontres de Moriond in Mesoscopic Physics, edited by D. C. Glattli, M. Sanquer and J. Trân Thanh Vân (The GIOI Publishers, 2005).

[P8] M. A. Sillanpää, L. Roschier, and P. J. Hakonen, *Direct measurements of tunable Josephson plasma resonance in the L-SET*, to appear in "Quantum Computation: solid state systems", proceedings of the IV International workshop on Macroscopic Quantum Coherence and Computing, edited by P. Delsing, C. Granata, Y. Pashkin, B. Ruggiero and P. Silvestrini (Kluwer Academic Plenum Publishers 2005).

[P9] L. Roschier, M. Sillanpää, and P. Hakonen, *Quantum capacitive phase detector*, Phys. Rev. B **71**, 024530 (2005).

[P10] M. A. Sillanpää, L. Roschier, and P. J. Hakonen, *Charge sensitivity of the Inductive Single-Electron Transistor*, Low Temperature Laboratory Publications TKK-KYL-013, R2005017 (2005); submitted to Applied Physics Letters.

[P11] R. K. Lindell, J. Delahaye, M. A. Sillanpää, T. T. Heikkilä, E. B. Sonin, and P. J. Hakonen, *Observation of shot-noise-induced asymmetry in the Coulomb blockaded Josephson junction*, Physical Review Letters **93**, 197002 (2004).

Author's contribution

The primary contribution by the author of this thesis is the experimental study of the charge-dependent Josephson plasma resonance and its device application, the Inductive Single-Electron Transistor. My direct input has been decisive at every stage of this project. The author was responsible for the evaluation of the initial idea, preparation of the samples, and of the cryogenic setup for this project. I made the measurements, analyzed the data, developed theory, carried out the calculations, and wrote the publications ([P6] , [P7] , [P8] , [P10]). For the theory paper [P9] on the quantum capacitive phase detector, I made calculations and wrote parts of the publication. For [P5] , I built the setup and ran measurements together with L. Roschier, and also checked calculations. For the papers [P1] and [P2] , the author made all excluding the theory in [P1] , and some writing.

In the rest of the publications, my biggest input has been more practical. The author has been heavily involved in setting up and developing the everyday laboratory practices, such as the sample fabrication process, cryogenics, and data acquisition, as well as maintenance and update of the numerous equipment we used. Research reported in publications [P3] , [P4] and [P11] relies much on the functioning laboratory infrastructure. I also made the following direct contributions: In [P4] I participated in sample fabrication, and design and running of the measurements. In [P3] I made measurements on the amplifier parameters (section 4.3.2), and noise measurements. For [P11] , I carefully constructed a low-noise DC measurement setup (Fig. 2.2).

Contents

Chapter 1

Overview of this work

I will first introduce some main principles of this thesis work in simple terms.

The modern western society and our way of life owes a great deal to the development of physics in the 20th century. This may not be obvious to everyone. In particular, our civilization relies heavily on electrical digital technology. Its basis was created by physicists making breakthroughs with basic research in their laboratories. Basic research is the most fundamental research effort aiming at understanding the laws that nature obeys. Engineers then took the knowledge into use to create device applications that are currently employed in our everyday life.

This thesis represents basic research in a new and growing field of physical science, commonly termed *nanotechnology*, which may in the future belong to everyday life in a manner similar to computers do today. The present work involves exploration of certain weak physical phenomena which become apparent only if disturbances coming from the environment are sufficiently attenuated. In practice, this means a very low temperature not more than one tenth of a degree above the absolute zero at -273.15 degrees Celsius, and a size below a thousandth of a millimeter, one micrometer (μm). On this length scale, physical structures resemble large clusters measuring a few hundreds of atoms across.

At yet smaller size scale, at the level of a single atom or molecule, phenomena radically differ from those in our macroscopic world. In the latter, physical phenomena such as the running of a car engine, or space-ship motion in outer space, are immensely accurately described by Newton's laws of mechanics. However, the description of elementary particles which constitute atoms, works correctly only with Schrödinger's equation which is a quantum-mechanical counterpart of Newtons' equation of motion. According to the quantum description, elementary particles resemble *waves*, such as we

see, for instance, on the surface of water. These waves are commonly called matter waves, or denoted with an abstract *wave function* $|\Psi\rangle$.

Like ordinary waves, matter waves can interfere, that is, strengthen or weaken each other. The total wave of an electronary particle can also be a sum, or as it is commonly called, a superposition, of two or more distinct waves. For instance, the wave $|\Psi\rangle$ of an electron can be the sum of waves going to the left and to the right. Mathematically, this is expressed as $|\Psi\rangle = |0\rangle + |1\rangle$. The symbols $|0\rangle$ and $|1\rangle$ mean the two waves, respectively. The symbols are actually nothing more than names for the waves. The message, nevertheless, is that the electron is simultaneously going to the left and to the right, which contradicts common sense.

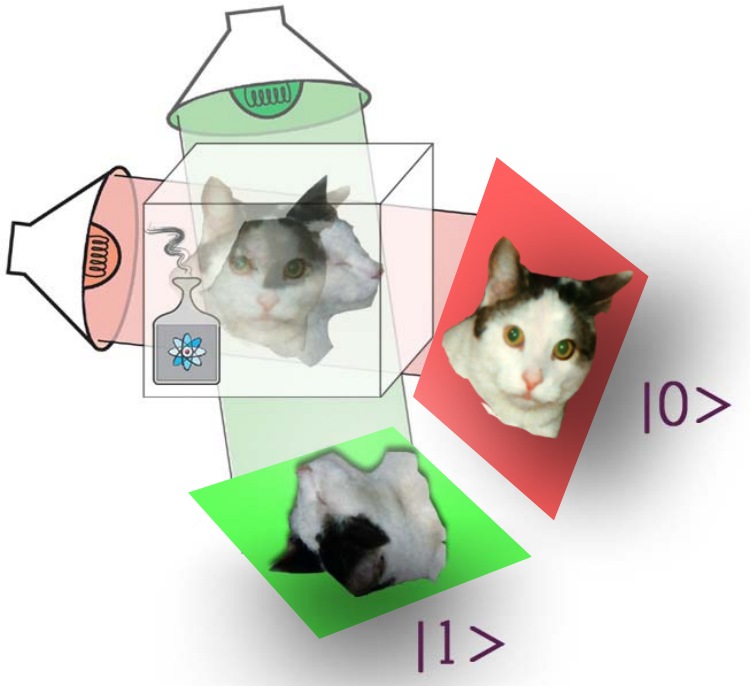

Figure 1.1: Erwin Schrödinger presented in 1935 a paradox of a quantum-mechanical cat [1]. The thought experiment (hopefully nobody will attempt to do the experiment) involves sealing a cat and a bottle of lethal poison into a tight box. Once triggered by the decay of a radioactive atom at a random instant of time, the bottle will open, release the poison, and kill the poor cat. The cat, the radioactive atom, and the bottle of poison evolve into a special kind of quantum state known as entangled state, where the atom is simultaneously decayed and not decayed, and hence the cat is simultaneously dead and alive. Only a "measurement" which means opening the box and looking in, makes the cat dead or alive.

However, when someone actually measures into which direction the electron is going (it can be performed, though it may not be easy), then, according to the principles of quantum mechanics, the total wave $|\Psi\rangle$ *collapses* into either $|0\rangle$ or $|1\rangle$ and hence we are left with an electron wave going either to the left or to the right, but not both.

Nothing as such limits interference of matter waves to happen only in the microscopic world of elementary particles. Because of the linearity of the Schrödinger equation, sum waves of elementary particles, such as atoms, molecules, tennis balls, or humans, obey the same wave laws. However, various disturbances of environment effectively "measure" these kind of macroscopic quantum waves such that quantum superpositions do not usually exist *in practice* in the macroscopic world. For example, the superposition of, say, a cat-size object (like the one in Fig. 1.1), collapses within roughly 10^{-22} seconds which is the time it takes for a single particle of light, a photon, to hit it!

Moderately large objects can, nevertheless, have quantum mechanical features, but typically this requires good shielding from disturbances. A famous example is the phenomenon of superconductivity (Fig. 1.2) which takes place at low temperatures. Electrical current is carried by electrons which are detached from their host atoms and move relatively freely through solid matter. In a normal electrical conductor the waves of electrons oscillate out of rhythm. In a superconductor, however, the electron waves have a common rhythm and therefore they strengthen each other [2].

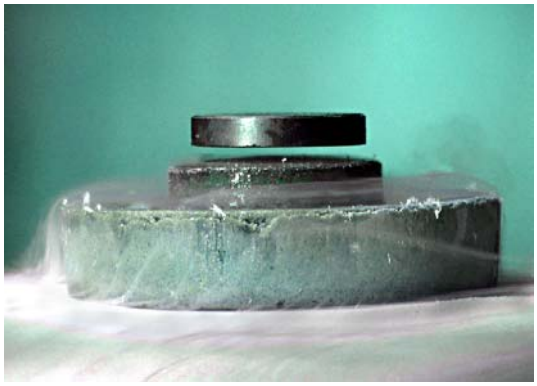

Figure 1.2: Permanent magnet levitates above a superconductor. The famous phenomenon is due to the so-called Meissner effect characteristic to all superconductors. "High temperature" superconductors, such as the piece of Yttrium Barium Copper Oxide (YBCO) here, can display full superconducting properties at as "high" a temperature as that of the boiling point of nitrogen (-196^{o} C).

If a superconducting wire is cut, but the ends are kept a few nanometers (millionth of a millimeter) apart from each other, electron waves can cross the gap, as illustrated in Fig. 1.3. This peculiar phenomenon is called tunneling, and the famous structure is named a Josephson junction after Brian D. Josephson who predicted it theoretically in 1962 [3] and was awarded the Nobel Prize in physics for the discovery only eleven years later.

Thousands of scientific articles have been written on Josephson junctions since then. This thesis deals mostly with very small Josephson junctions, in which quantum-mechanical interference effects are especially strong.

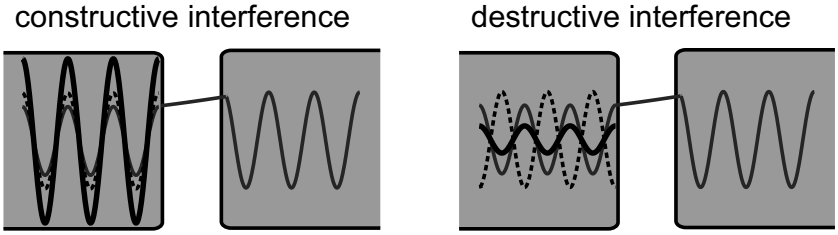

Figure 1.3: Schematic illustration of a superconducting tunnel junction (Josephson junction). Depending on the phase of waves on different sides of a narrow gap in the superconductor, the sum wave (strong line) may become stronger (left), or weaker (right).

One such structure consists of a tiny piece, an "island", of a superconductor, less than μm across, and two Josephson junctions. The quantum state of the small island can now be a superposition of whether or not one single pair of superconducting electrons have tunneled into the island, as shown in Fig. 1.4. Since this single pair can also control the flow of billions of other electrons, the quantum state of the island is a macroscopic superposition, like that of the famous Schrödinger cat.

Quantum-mechanical phenomena in Josephson junctions may in the future be used to build an ultimate device for mankind: a quantum computer.

Ordinary bits are always either 0 or 1. Nobel Laureate Richard Feynman proposed in early 1980's a bit [4] which would be *simultaneously* 0 and 1. This is a quantum-mechanical bit, or qubit. Qubit values are the quantum states $|0\rangle$ and $|1\rangle$ and can also be, according to the principles of quantum mechanics, a superposition of them. A computer composed of at least a few hundred qubits, if ever to be built, is the quantum computer. Because of the superposition, a quantum computer would calculate the outputs for all possible inputs in a single run (quantum parallelism), and hence it would be immensely faster than any supercomputers ever built using ordinary bits.

Small Josephson junctions, such as those in Fig. 1.4, may be used in several ways as building blocks of a quantum computer. After the quantum

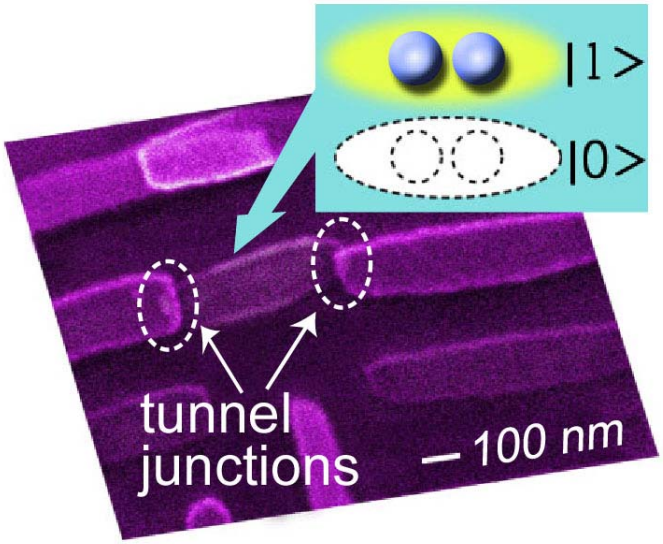

Figure 1.4: Electron microscope image of an actual sample studied in this work. A pattern consisting of aluminium wires 100 nm wide (size of a typical virus) has been fabricated by evaporation on the surface of a smooth silicon chip (750 similar wires would fit the diameter of human hair, 75 μm on the average). One pair of superconducting electrons $|1\rangle$, or zero pairs $|0\rangle$, may have tunneled into an isolated grain through the Josephson junctions.

computation, value of each qubit should be measured. This step is the main concern of this thesis. The L-SET device described, for instance, could be useful for that purpose. In quantum mechanics, measurement has a special role. One could imagine the difficulty of measuring, say, the position of a wavelike entity. This also turns out to be the case. One of the most famous results in quantum mechanics is the Heisenberg uncertainty principle. It states that for any conceivable object, such as an atom, a tennis ball, or a human being, whose energy is E, this energy fluctuates by an amount ΔE during a time interval Δt such that

$$\Delta E \Delta t > h/(4\pi), \tag{1.1}$$

where h is a fundamental constant of nature, whose value in the SI-units is roughly 6.626×10^{-34} Joule-seconds, and is called the Planck's constant. The Heisenberg uncertainty principle, Eq. (1.1), and a couple of similar others, state that quantities like energy and time cannot be measured simultaneously arbitrarily accurately because they do not even have well defined values at the same time. Although this kind of fundamental limitations are of little observable significance in our everyday life, in quantum-mechanically behav-

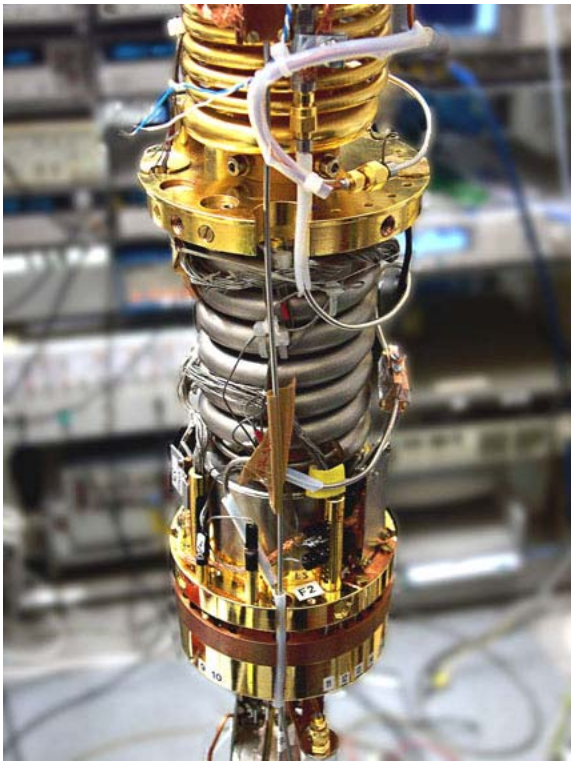

Figure 1.5: Powerful dilution refrigerator used in this work reaches temperatures as low as 9 milli-Kelvins. Some electrical measuring equipment are seen on the background.

ing systems, such as small Josephson junctions, they may have very well observable consequences related to physical phenomena, their measurement in particular.

For the experiments done in this thesis, the studied micro-structured samples must be extremely carefully isolated from electrical noise. They must also be cooled down to well below one degree Kelvin, because temperature is also a form of noise. The cooling is done using a so-called dilution refrigerator (it is shown in Fig. 1.5), where "cold is produced" by circulation, powered by strong pumps, of a mixture of the two helium isotopes, ^{3}He and ^{4}He.

Chapter 2

Technological aspects

THE research described in this thesis is primarily experimental. Accordingly, we will discuss some techniques developed which have proven particularly useful over the years.

2.1 Measurement setup

In this section, we will briefly describe the schematics of the electrical measurements, and the related cryogenic apparatus.

2.1.1 Low-frequency measurements

By low-frequency electrical measurements we here mean those whose band is limited by wiring capacitance and sample resistance, or preamplifier, down to typically below 10 kHz. These are also referred to as DC measurements. Publications [P1] , [P2] , [P3] , [P4] , [P11] are exclusively based on data gathered in these types of measurements.

Several different DC measurement schemes were tested at different cryogenic sites which varied, for instance, with respect to environmental disturbances (50 Hz and its harmonics), and the quality of grounding. In every case, success was estimated in terms of the voltage width of the smallest features in the IV-curve. In a DC-measurement, this indicates the amount of unwanted AC voltage, due to noise and pickup, over the sample.

A home-made optoisolator based on a commercial optical isolation amplifier (Fig. 2.1) turned out to be useful in order to get rid of disturbances due to ground loops.

The best setup, used by co-workers to measure the data in [P11] using the lines 12, 21, 22 and the sample holder in Fig. 2.3 (a) is described in Fig.

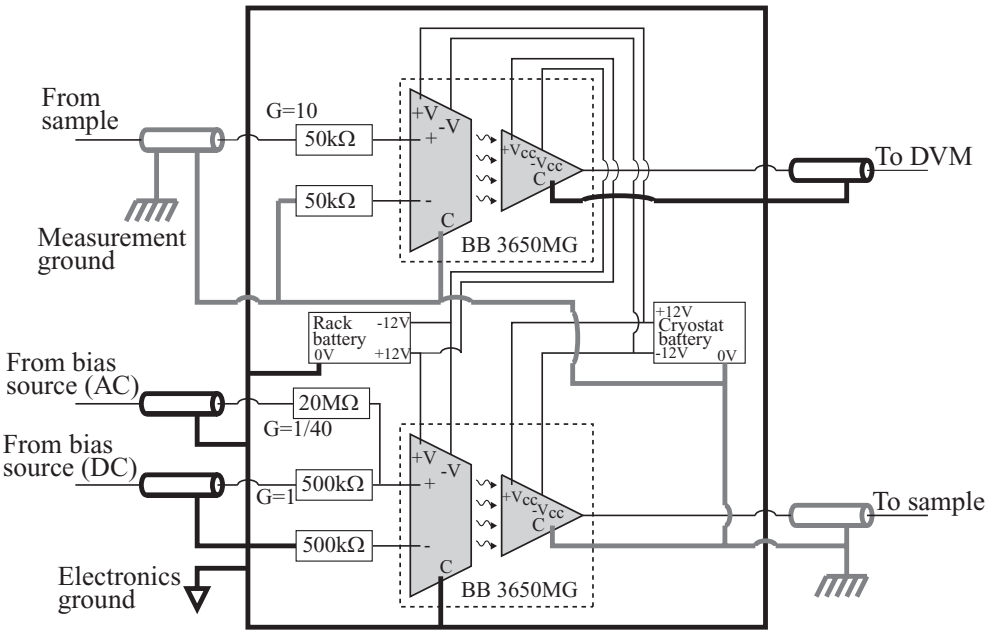

Figure 2.1: Optoisolator for low-frequency measurements. The separated grounds are marked in black and gray.

2.2. The optoisolator was used for both input and output leads. The current amplifier Ithaco 1211 yielded the best results.

Thermocoax cable (diameter 0.5 mm, inner conductor resistivity $\sim 50\ \Omega/\mathrm{m}$) plays an important role in sample holder design. Its main function is to filter noise above 1 GHz [6]. Unfortunately, its processing requires special tricks because it is made of stainless steel.

In the best sample holder (Fig. 2.3 (a)), 1.1 meters of Thermocoax was wound around the Cu holder for each line, and attached by silver soldering. The Thermocoaxes were terminated into MCX connectors which were soldered to the cable outer shield using a special soldering flux. Inner conductors (IC) of Thermocoax were soldered either by first silver coating, or directly tin-soldered using the special flux and 40 μm bare Cu wire wound 10-20 turns around the IC. The fluid and tin solder alone, without the Cu wire, do not suffice to wet the IC properly.

Adverse resonances at $1 \sim 10$ GHz in the wiring were quite successfully eliminated by engineering an impedance match on the path, and reducing path length, between the sample and the Thermocoax cable that also acts to dampen these resonances. Contact problems have so far not been encountered in the described wiring.

Noise attenuation of the DC wiring above 10 MHz is efficient (Fig. 2.4)

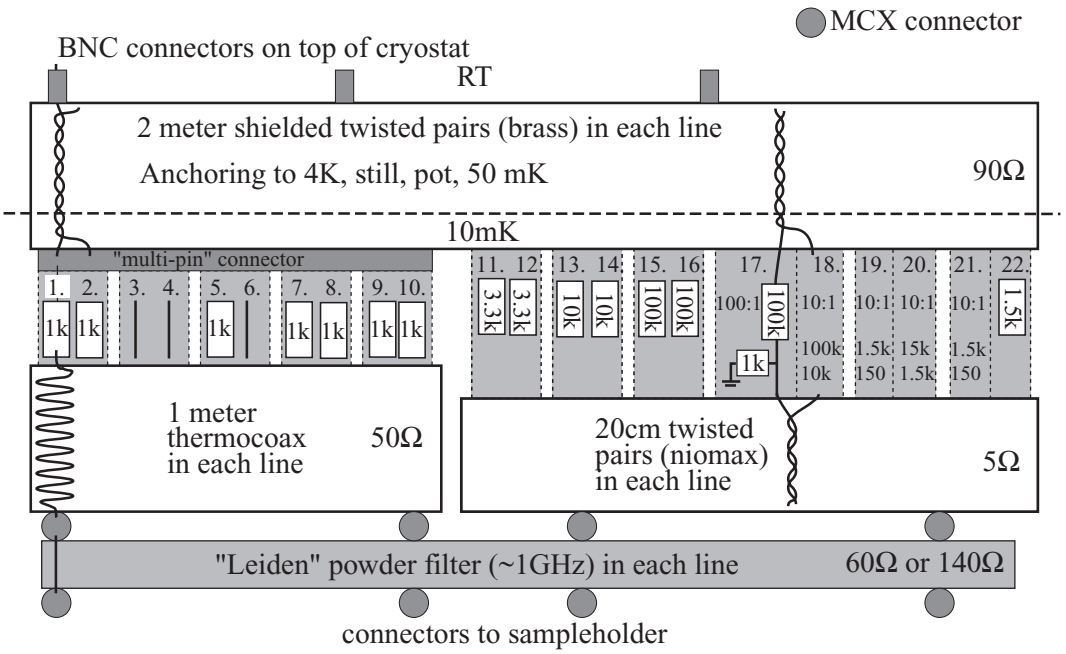

Figure 2.2: DC wiring in the Leiden MNK126-150/700 cryostat. Shown are series resistors or voltage dividers consisting of tiny $0.3 \times 0.8 \times 1.6$ mm SM resistors [5]. Minicircuits *LC* filters Low Pass 1.9 MHz were used atop the cryostat.

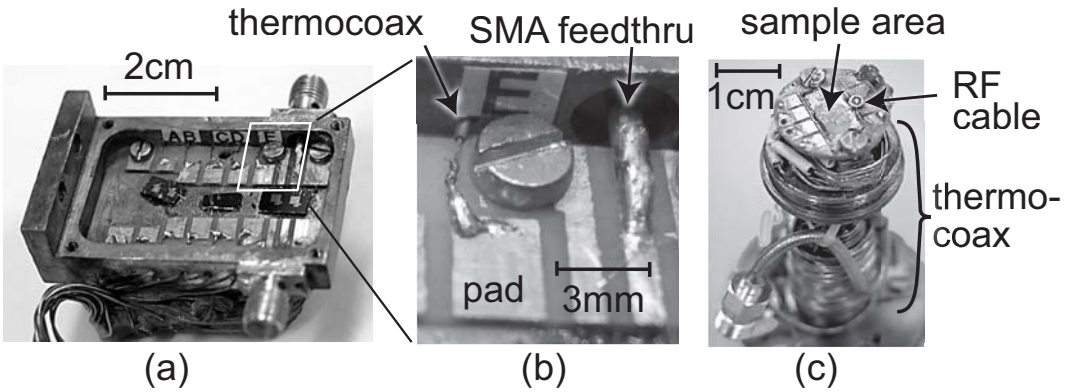

Figure 2.3: Photographs of sample holders used in this research; (a) the best holder (see text); (b) detail of its Thermocoax - bonding pad connection; (c) another holder which had a special installation of an RF cable: the sample pad was bonded directly to its inner conductor.

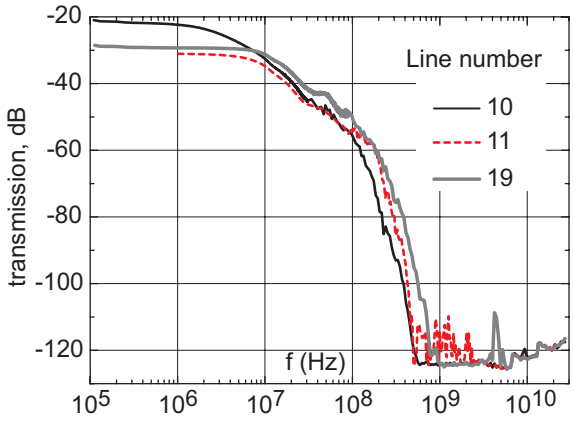

Figure 2.4: Power transmission of the described DC wiring in a 50 Ω system. The line numbers refer to Fig. 2.2.

independent of the voltage divisions. Further filtering of noise and pickup at the lowest frequencies was attempted with tough *LC* filters packed into a BNC case [7], but their high reactance caused the amplifiers to oscillate.

2.1.2 Radio-frequency measurements

Measurement cables should be carefully constructed also at radio frequencies (around 1 GHz). Our cables [8] with typically home installed SMA connectors exhibit the first resonances around 22 GHz, above which transmission rapidly weakens. It is often also desired to band-pass filter around the desired operation frequency in order to suppress noise. This was done using commercial *LC* filters [9]. They worked without change down to 25 mK.

The final version of the cabling (Fig. 2.6) was used in the latest L-SET experiments (sample E, see Sec. 5). Determination of the power reaching the sample through the numerous cables and other components whose attenuation depends on temperature, is a matter of some concern. We measured the setup attenuation, from the cryostat top down to the sample, at RT. The attenuation was estimated to reduce about 3 dB at the base temperature. For the setup in Fig. 2.6, the attenuation finally amounts to −66 dB.

Success of the L-SET experiments heavily relied on the microwave circulator (Fig. 2.5) whose S-parameters were measured in a separate cooldown. For the low-temperature test, port 3 was terminated with a matched 50 Ω load. At RT, the insertion loss S_{21} within the circulator band was 0.5 dB. At cryogenic temperatures, it is not known accurately. The increase in S_{21} in Fig. 2.5 (b) at low temperatures is likely to be due to decrease of cable

attenuation. Above the operation band at 1 GHz − 6 GHz, both S_{12} and S_{21} were $-30... - 15$ dB. Based on the circulator test, we conclude that the circulator performs even better at cryogenic temperatures, although its band changes moderately.

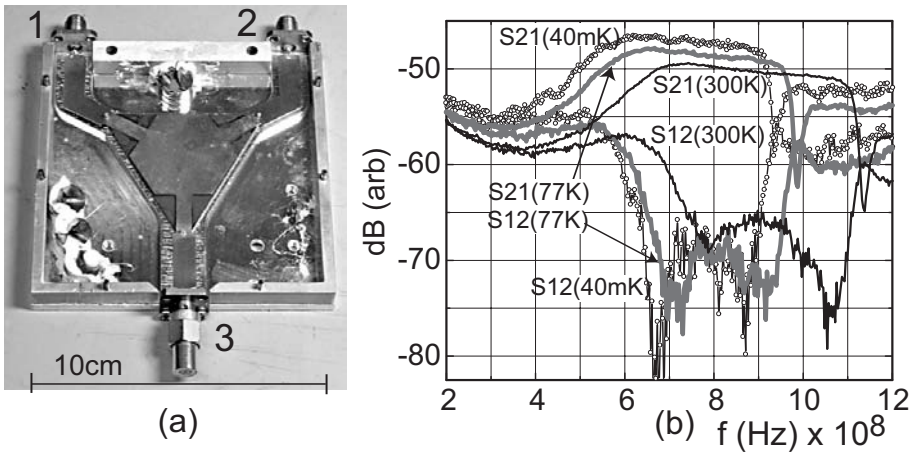

Figure 2.5: (a) Photograph of partially disassembled Pamtech UTE1255K circulator; (b) its S-parameters measured at RT, 77 K, and 40 mK.

Performance of the RF setup was first investigated with RF-SETs fabricated from Al, or from carbon nanotubes [10], as discussed in [P5] . Problems arose because certain aluminium cables broke after a couple of full thermal cycles from RT down to to 4 K. Similarly, the performance of pressed contacts in the Anritsu bias-T K251 and the Krytar directional coupler sometimes degraded during cooldown (note that the cabling setup for the RF-SET differs from that of the L-SET in Fig. 2.6).

The RF-SET [11] is based on the famous sequential tunneling SET [12] (either normal or superconducting). In the RF-SET setup, a SET is coupled to an LC tank circuit, resonant at the angular frequency ω_0, in the scheme shown for instance in Fig. 1 of [P5] . The SET resistance R_{SET} depends on the gate charge, which affects dissipation in the resonator circuit. The advantage of the RF-SET scheme is based on making an impedance match from high-impedance SET into a low-impedance transmission line capable of transmitting very high frequencies. This enables high sensitivity and high speed, where the latter is determined by the loaded quality factor, $\sim \omega_0/Q_L$. The system is probed by reflection measurement (for a review of these standard techniques, see e.g., Ref. [13]).

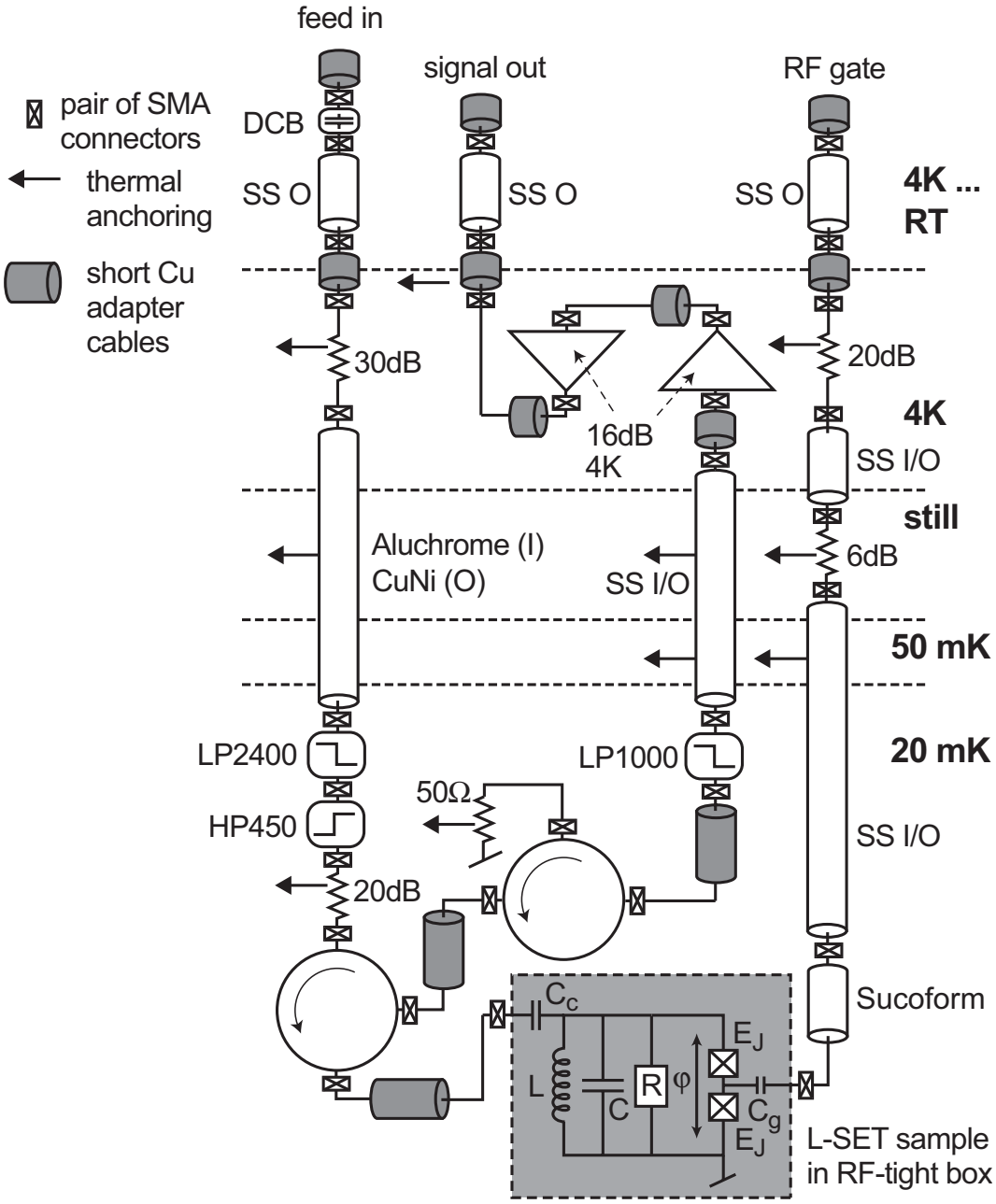

Figure 2.6: Improved cabling used in RF studies of the Josephson plasma resonance in the Leiden MNK126-150/700 cryostat. Two circulators at the base temperature had at least a total of 40 dB backwards isolation within the 630 MHz − 900 MHz band. Filter cut-offs are expressed in MHz.

Let us denote the resonator impedance, including the SET, by Z, and the wave impedance of transmission lines by Z_0, here $Z_0 = 50\,\Omega$. The AC voltage reflection coefficient $\Gamma = |\Gamma| \exp(\mathrm{i} \arg(\Gamma))$

$$\Gamma = \frac{Z - Z_0}{Z + Z_0} \tag{2.1}$$

is quite sensitive to Q_L

$$Q_L = \frac{R_{SET}\omega_0 C}{1 + Z_0 R_{SET}/(\omega_0 L)^2}. \tag{2.2}$$

Electrometer performance of the RF-SET is a compromise between charge sensitivity s_q and bandwidth. The best experimentally demonstrated numbers are $3.2 \times 10^{-6} e/\sqrt{\mathrm{Hz}}$ and 7 MHz [14], or $1.2 \times 10^{-5} e/\sqrt{\mathrm{Hz}}$ and 100 MHz [11] for s_q and bandwidth, for slow and fast devices, respectively. Our carbon nanotube RF-SETs, with a measured $s_q \sim 2 \times 10^{-5} e/\sqrt{\mathrm{Hz}}$ and estimated bandwidths on the order of 50 MHz hence perform fairly well.

2.2 Sample fabrication

The metallic sub-micron samples studied in this thesis were patterned using rather well-established procedures of electron-beam lithography and shadow evaporation [15]. Contribution by the author was to push this technology against its limits by (1) increasing the charging energy E_C by reducing overlay junction size; (2) increasing the Josephson energy E_J at a given E_C by reducing thickness of the insulating Al_2O_3. Choice of the fabrication method turned out to be crucial for fulfilling these criteria which resulted in a successful demonstration of the charge-tunable Josephson inductance (Sec. 5).

The probability that a particle with mass m and energy E penetrates a potential barrier $V(x)$ is in the WKB approximation given by the expression

$$P = \exp\left\{-\frac{4\pi}{h}\int_{x_1}^{x_2} \sqrt{2m(V(x) - E)}dx\right\}. \tag{2.3}$$

In the theory of Simmons [16], this leads to a low-voltage conductance per unit area of a tunnel junction having the barrier height V_0, width d, and area A:

$$(R_T A)^{-1} = \frac{e^2\sqrt{2mV_0}}{h^2 d} \exp\left(-2d\sqrt{2mV_0}/\hbar\right). \tag{2.4}$$

Quite often one wants to maximize both E_J and E_C. This leads to the maximization of their product which turns out to be independent of junction area. Using Eqs. (2.4) and (5.2) we have

$$E_J E_C = \frac{e^2\sqrt{2mV_0}\Delta \exp\left(-2d\sqrt{2mV_0}/\hbar\right)}{16\epsilon_r\epsilon_0 h}. \quad (2.5)$$

Inserting the values $V_0 = 2\,e$V, $\Delta = 0.2$ meV, $\epsilon_r = 4$ in Eq. (2.5) (note that it is not very sensitive to these parameters), we find $E_J E_C \sim 6$ or ~ 1.5 for $d = 0.5$ nm or 0.6 nm, respectively. This is roughly the thickness of *a single molecular layer* of Al_2O_3, and hence it seems that $E_J E_C \gg 1$ is impossible to achieve using Al. As will become apparent below, this limit has probably been reached in our samples. Recently, similar figures for the junction resistivities were reported in Ref. [17].

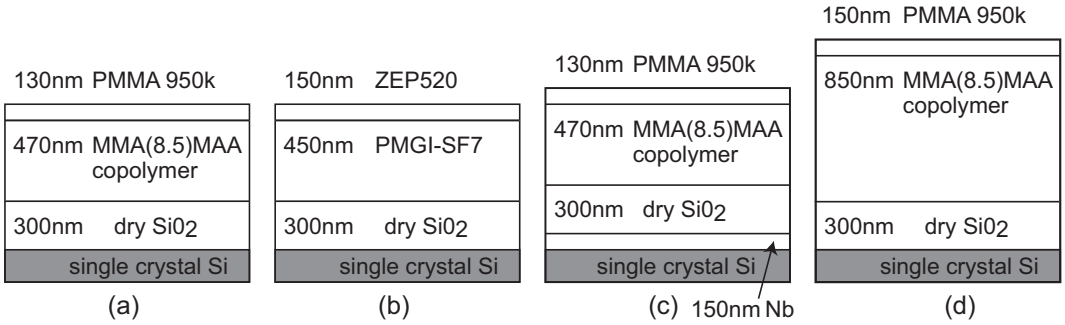

Figure 2.7: Resists used for fabricating L-SET samples. The silicon wafer in (a), (b) and (d) was "High purity silicon", 1800-3900 Ohm cm from Topsil. Only substrates (a) and (d) resulted in good devices.

We used two different resists and several substrates for sample fabrication. Those used in the L-SET experiment (see Sec. 5) were as shown in Fig. 2.7. Resist (c) had a nearby Nb ground plane in order to reduce cross-coupling from gates. The average tunnel oxide parameters resulting from use of the two tested resists, PMMA/MAA and ZEP/PMGI, are listed in Table 2.1.

resist	$R_T A$ (in units of k$\Omega \times 100$nm^2)	$E_J E_C$ (K^2)
PMMA/MAA	6 ± 3	2.1 ± 1.8
ZEP/PMGI	22 ± 10	0.5 ± 0.2

Table 2.1: Average tunnel junction resistivity parameters, and their standard deviation, for the two tested resists. For discussion, see text.

For the L-SET samples, we used a quite minimal oxidation of 40-80 mTorr for 30-40 s. Resistivity was not found to noticeable depend on the exact oxidation pressure or time. We conclude that ZEP/PMGI (substrate (b)) resulted in a $E_J E_C$ four times lower than that for PMMA/MAA, likely due

to thicker oxide caused by stronger outgassing of the former resist. It would be unlikely, using this resist, to successfully fabricate an L-SET having both E_J and E_C high enough.

The measured and functioning samples of the L-SET experiment are listed in Table 2.2. In addition, there was one sample measured which did not indicate any gate modulation. We believe it had one junction short-circuited.

L-SET sample	A	B	C	D	E
resist (Fig. 2.7)	b	a	d	c	a
R_{SET} (kΩ)	4.2	9.6	22	17.5	22
E_J (K)	3.5	1.6	0.65	0.87	0.68
E_C (K)	0.17	0.92	5.4	2.3	2.6
E_J/E_C	20 (max)	1.7	0.12	0.38	0.26
$E_J E_C$ (K^2)	0.62	1.5	3.5	2.0	1.8
E_C/Δ	0.07	0.4	2.2	0.9	1.0
$\min L_J^*$ (exp., nH)	8	19	260	65	66
$\min L_J^*$ (theory, nH)	5.1	15	47	33	43
$\Delta L_J^*/(\min L_J^*)$ (exp., %)	0	16	50	20	340
$\Delta L_J^*/(\min L_J^*)$ (theory, %)	0	15	760	190	320
L (nH)	3	7.4	34	28	28
C (pF)	22	8.4	1.6	2.7	1.2
C_c (pF)	0.72	0.72	0.23	0.5	0.5
gate period	$-$	$2e$	e	e	$2e$
f_0 (MHz)	610	614	646	570	726
f_p (max, MHz)	707	723	690	735	870
Q_i	13	18	27	15	16
Q_L (at $\min L_J^*$)	11	15	26	12	9
P_c (exp., dBm)	-102	-116	$-$	-117	-112
P_c (theory, dBm)	-96	-104	-109	-108	-112
s_q (exp., $e/\sqrt{\text{Hz}}$)	$-$	2.0E-3	$-$	6E-4	7E-5
s_q (theory, $e/\sqrt{\text{Hz}}$)	$-$	5E-4	8E-6	4E-5	3E-5
s_q (exp. anharm., $e/\sqrt{\text{Hz}}$)	$-$	1.4E-4	$-$	1E-4	3E-5

Table 2.2: Summary of parameters and experimental results of the measured L-SET samples and their tank LC oscillators. For samples C and D, the small values of L_J^* were cut off due to quasiparticle poisoning.

Determination of the important parameters in this experiment is not entirely straightforward. Here, E_C is deduced from the total surface area of the tunnel junctions (SEM image), assuming a specific capacitance of $\sim 0.4-0.5$

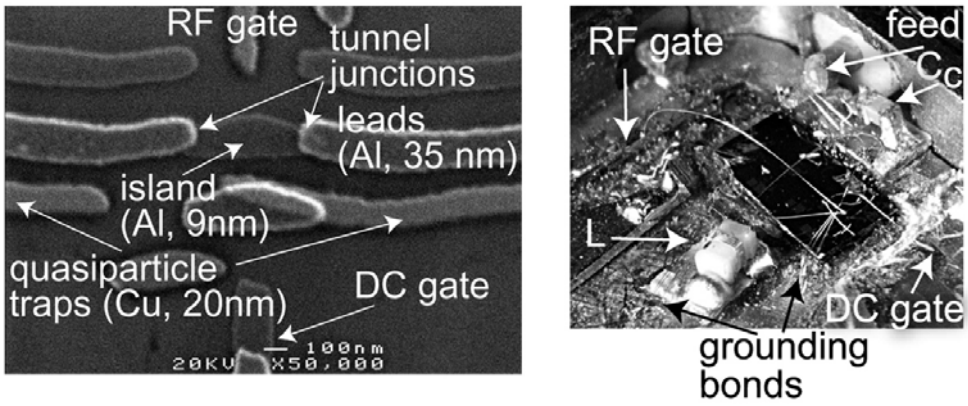

Figure 2.8: Left: SEM image of an L-SET sample (E). Layer thicknesses are indicated. The Cu traps were in contact with the leads 5 μm from the junctions. Right: An earlier L-SET sample placed into a holder.

fF for 100 nm^2 [18]. The shunting capacitance C was formed by a bonding pad, or by a cm-sized metal-coated chip connected by bonding for samples A and B. The inductance L consisted of a surface-mount (SM) Cu-wire inductor and the bond wire (the latter contributing $5-10$ nH), or only of the bond wire (samples A and B). The coupling capacitor C_c was a ceramic SM capacitor [19], or an interdigital one patterned directly on-chip (sample C).

It was estimated that the figures of the SM capacitors reduce by 15% when cooled. The value of L can also be determined quite accurately as the sum of the SM inductor and the piece of bond wire (~ 10 nH/cm). The capacitance C is difficult to determine independently, but once the resonance frequency f_0 is checked, it can be easily calculated. In this way, we expect an accuracy of about $10-20\%$ for the listed parameter values.

Values for the observable SCPT Josephson inductance L_J^*, and its modulation depth, are extracted from the measured frequency of the Josephson plasma resonance f_p (using Eq. (5.10)), assuming it is determined by $L_{\rm tot} = L \parallel L_J^*$.

For the L-SET sample E (Fig. 2.8 (a)), it was attempted to make the superconductor energy gap Δ on the island larger than that in the leads in order to suppress quasiparticles to a minimum [20]. Since Δ is expected to enhance with reducing grain size [21], island of the SCPT was deposited only 9 nm thick. The island was also deposited first such that it would become dirtier than the leads due to a worse vacuum [22, 23]. Both factors tend to increase Δ. However, it is questionable whether the procedure had any effect. Although sample E was notoriously free from quasiparticle poisoning even in time-averaged measurements, so was also sample B which was not fabricated

following the special recipe.

In certain applications [24,25] it would be highly advantageous to employ an NIN tunnel junction in contrast to SIS. The latter almost unavoidably results when using a process based on oxidation of Al. Accordingly, we developed a lithographic NIN process based on oxidation of titanium [26, 27]. Superconductivity of Ti got suppressed below 100 mK because Ti films became very disordered even though they were deposited under UHV, $\sim 10^{-8}$ mBar. We demonstrated the method by fabricating a working SET out of Ti, as detailed in Publication [P2] .

2.3 Superconducting proximity effect

In our samples, non-superconducting (normal, N) metal is often placed within a mesoscopic distance from the superconducting junctions being studied. It is therefore important to understand its possible negative impact on superconductivity.

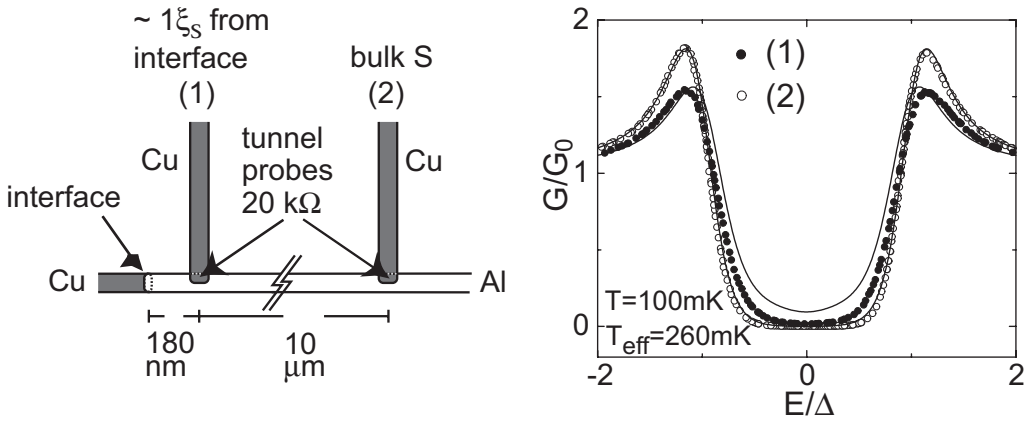

Figure 2.9: Experimental layout used in the study of the inverse proximity effect, and the measured differential conductance, with best fits to theory (solid lines). For discussion, see text.

We characterized the "inverse proximity effect" using tunnel spectroscopy [25,28]. Electronic density of states (DOS) was measured close to a transparent interface with an N metal (copper), or F metal (ferromagnet, nickel). The case of F is interesting also because some measurements [29, 30] indicated a possibility of a long-range proximity effect into F, in contrast a simple model. F results from our experiments were reported in [P1] . For N, the data is displayed in Fig. 2.9. We found that in both cases, the DOS shows a clear signature of the inverse proximity effect up to a distance of $\sim \xi_S$ from the

interface. The interfaces were made without delay, using the normal sample-fabrication process in UHV. Here, $\xi_S = \sqrt{\hbar D/(2\Delta)}$ is the coherence length of the superconductor in the dirty limit. In our Al films, we calculated $\xi_S \sim 160$ nm using the measured diffusion constant $D = l_e v_F/3 \sim 0.016$ m^2/s, where $l_e \simeq 30$ nm, and $v_F \sim 1.57 \times 10^6$ m/s.

The fit curves in Fig. 2.9 were calculated from the DOS using thermal smearing at $T_{eff} = 260$ mK owing to heating due to the probing current. The bulk probe (2) was well fitted to the BCS DOS $\propto |E|(E^2 - \Delta^2)^{-1/2}$. For probe (1), the DOS was calculated [31] using quasiclassical Green's function theory [32, 33], similarly as in [P1] . Non-ideality of the interface was taken into account by the interface parameter $r_b = R_B/R_\xi$, where R_B is resistance of the interface, and R_ξ is the resistance of a piece of N lead having the length ξ_S. Here we used $r_b = 3$ which was in agreement with values estimated from the sample. However, the fit of curve (1) is poor below the gap. The subgap fits well with as large as $r_b = 10$, however, the BCS peaks do not.

We interpret that the poor fit is due to intermixing of Cu and Al close to the interface. Although bulk interdiffusion even at RT is known to occur only at a distance of at most a few tens of nm, the significantly more rapid grain boundary interdiffusion can reach saturation levels of approximately 1 % of Al in Cu at RT [34, 35]. The amount of Al in Cu would increase the extent of proximity effect into N, thus reducing the inverse effect.

Based on these findings we conclude that the inverse proximity effect is unlikely to have an adverse influence on the superconducting properties provided that the SN contact is located several μm away.

Chapter 3

Conventional Josephson effect

THE description of the tunneling of supercurrent is based on the two Josephson equations [3]:

$$I = I_C \sin(\varphi) \tag{3.1}$$

$$\dot{\varphi} = \frac{2e}{\hbar} V. \tag{3.2}$$

The first equation is actually only a statement of the explicit form of the supercurrent-phase relationship. Significant deviations from the $\sin(\varphi)$ form can occur, for instance, if the tunnel resistance is very small, and Eq. (3.1) should then be replaced by a more appropriate one taking into account higher harmonics [36, 37]. Equation (3.2), however, arises from the very basics of quantum mechanics and holds for any junction.

The AC Josephson effect has been known since the original paper by Josephson. A related phenomenon, Shapiro steps [38], which forms the basis of a voltage standard, is thoroughly studied as well (see, e.g., the reviews in Refs. [39–41]). However, as we shall shortly discuss, some important aspects of the AC Josephson effect seem to have escaped explicit notice in the literature.

3.1 The concept of "critical voltage"

Let us start the discussion by considering a Josephson junction (JJ), biased with an AC current of magnitude at most the critical current, $I(t) = I_1 \sin(\omega t)$, where $I_1 \leq I_C$. Phase then evolves as $\varphi(t) = \sin^{-1}\left(I(t)/I_C\right)$, and voltage is obtained as $V(t) = \hbar/(2e)\dot{\varphi}(t)$. Altogether, we find for the voltage

$$V(t) = \frac{\hbar}{2e}\frac{d}{dt}\sin^{-1}\left(\frac{I_1}{I_C}\sin(\omega t)\right) = \frac{\hbar}{2e}\frac{I_1}{I_C}\frac{\omega\cos(\omega t)}{\sqrt{1-(I_1/I_C)^2\sin^2(\omega t)}}. \quad (3.3)$$

Let us now consider the special case of a critical AC current flowing through the JJ, i.e., $I_1 = I_C$. As discussed below, this is an important situation experimentally. For the AC voltage corresponding to the critical AC current we then have from Eq. (3.3)

$$V_C(t) = \frac{\hbar\omega}{2e}\frac{\cos(\omega t)}{|\cos(\omega t)|} = \frac{\hbar\omega}{2e}\left(\frac{4}{\pi}\sum_{k=1,3,..}\frac{1}{k}\sin(k\omega t)\right). \quad (3.4)$$

The result is a *square wave* of amplitude $\hbar\omega/(2e)$, and the last form is its Fourier expansion.

It is interesting to note that unlike the critical current, the critical voltage V_C does not depend on junction-specific properties, but is universal to all JJ's independent of their structure or transmission.

In experiment, we are mostly interested in voltage at the basic frequency; therefore, we take the 1st Fourier component of Eq. (3.4), and thus for current bias,

$$V_{CI} = \frac{2\hbar\omega}{\pi e}. \quad (3.5)$$

A full current bias may not be realized in practice. A similar calculation can be done, first of all, for a voltage biased JJ, with $V(t) = V_1\sin(\omega t)$, which yields $\varphi(t) = 2e/\hbar\int V(t')dt' = 2e/(\hbar\omega)V_1\cos(\omega t)$. When inserted into $I = I_C\sin(\varphi)$, this gives

$$I(t) = I_C\sin\left(\frac{2e}{\hbar\omega}V_1\cos(\omega t)\right). \quad (3.6)$$

Critical current is reached when the argument of the sine in Eq. (3.6) reaches the value $\pi/2$. This happens at the critical AC voltage for voltage bias,

$$V_{CV} = \frac{\pi\hbar\omega}{4e}, \quad (3.7)$$

whereupon the current has a somewhat rounded square-wave form $I(t) = I_C\sin(\pi/2\cos(\omega t))$.

It is also important to consider what the critical voltage is in the most general case when neither current nor voltage AC bias is realized. This can be done numerically in the scheme of Fig. 3.1.

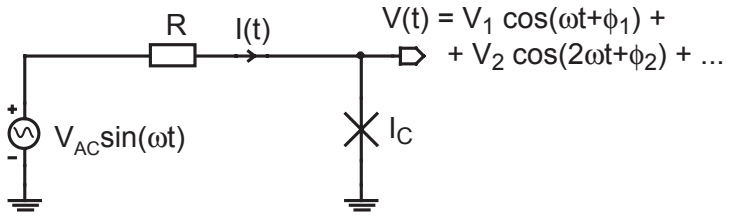

Figure 3.1: Schematic of a JJ in series with a voltage generator and a resistance R.

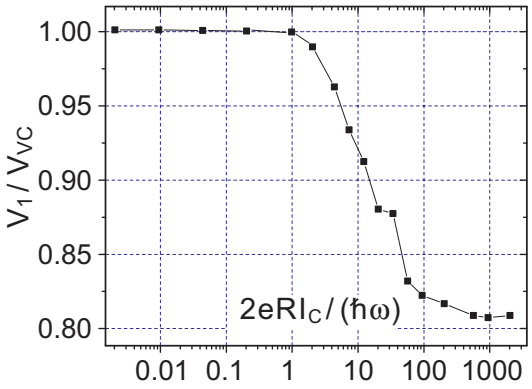

Figure 3.2: Critical voltage of a JJ as a function of the series resistance R computed numerically in the circuit of Fig. 3.1.

A convenient measure of the biasing scheme is the ratio of the external impedance to the JJ linear impedance $b \equiv 2eRI_C/(\hbar\omega)$ which vanishes for a voltage bias, equals 1 at a maximally mixed bias, and diverges at current bias. The outcome of a calculation run using harmonic balance with 20 upper tones in the Aplac circuit simulator is shown in Fig. 3.2. According to the calculation, the critical voltage interpolates smoothly between Eqs. (3.5), (3.7) as a function of biasing.

A few waveforms of the critical voltage and critical current are plotted in Fig. 3.3. Note that although V_C occasionally exceeds 1, its first Fourier component does not.

In order to appreciate these results in a wider scope, let us next examine in more detail a JJ biased both by DC and AC voltages, $V(t) = V_{DC} + V_1 \sin(\omega t)$. Phase evolves in time as $\varphi(t) = 2e/(\hbar\omega)V_1 \cos(\omega t) + 2e/\hbar V_{DC} t$. Current through the JJ is $I(t) = I_C \sin(\varphi(t))$, which can be evaluated using trigonometric expressions and the following formulas

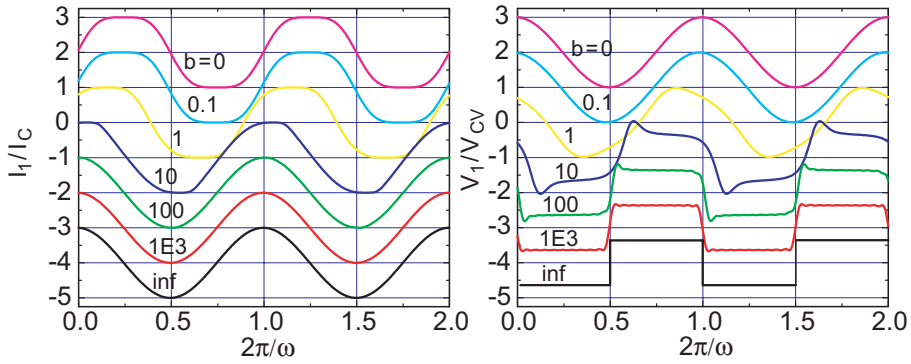

Figure 3.3: Waveforms of critical current and critical voltage of a JJ at different biasing schemes as denoted. The curves have been shifted vertically for clarity.

$$\sin\left(A\cos(\omega t)\right) = 2\sum_{k=0}^{\infty}(-1)^k J_{2k+1}(A)\cos\left((2k+1)\omega t\right) \tag{3.8}$$

$$\cos\left(A\cos(\omega t)\right) = J_0(A) + 2\sum_{k=1}^{\infty}(-1)^k J_{2k}(A)\cos\left(2k\omega t\right) \tag{3.9}$$

where J_k are Bessel functions of the first kind and of order k. An important expression is then obtained for the current [39],

$$I(t)/I_C = 2\cos\left(\frac{2e}{\hbar}V_{DC}t\right)\sum_{k=0}^{\infty}(-1)^k J_{2k+1}\left(\frac{2e}{\hbar\omega}V_1\right)\cos\left((2k+1)\omega t\right) + \\ + \sin\left(\frac{2e}{\hbar}V_{DC}t\right)\left[J_0\left(\frac{2e}{\hbar\omega}V_1\right) + 2\sum_{k=1}^{\infty}(-1)^k J_{2k}\left(\frac{2e}{\hbar\omega}V_1\right)\cos\left(2k\omega t\right)\right], \tag{3.10}$$

which yields, for instance, a DC current at DC voltages satisfying $V_{DC} = k\hbar\omega/(2e)$. This is the phenomenon of Shapiro steps which is easily detected in a standard DC transport measurement when the JJ is irradiated with microwaves. The amplitude $I_{0,k}$ of the k^{th} DC current step depends on the drive strength as

$$I_{0,k}/I_C = J_k\left(\frac{2e}{\hbar\omega}V_1\right). \tag{3.11}$$

Let us now examine the case of a pure AC bias, $V_{DC} = 0$. Then the 2nd term in Eq. (3.10) drops out, and the currents I_k at the basic frequency $k = 1$ and at all its higher harmonics are simply

$$I_k/I_C = 2J_k\left(\frac{2e}{\hbar\omega}V_1\right), \quad \text{for odd } k, \tag{3.12}$$

while the even harmonics are zero. A useful quantity is the impedance of the JJ at the basic frequency,

$$Z_1 = \frac{V_1}{I_1} = \mathrm{i}\frac{V_1}{2I_C J_1\left(\frac{2e}{\hbar\omega}V_1\right)}, \tag{3.13}$$

where the imaginary unit means that the current has a $\pi/2$ phase shift with respect to the voltage bias. The inverse of Eq. (3.13) is the admittance Y_1, and it generalizes to the admittance at an arbitrary harmonic:

$$|Y_k| = \frac{I_k}{V_1} = \frac{2I_C J_k\left(\frac{2e}{\hbar\omega}V_1\right)}{V_1}. \tag{3.14}$$

The JJ impedance, Eq. (3.13), is asymptotically periodic with respect to the drive amplitude V_1 with the period $4\,V_{CV}$ at large V_1. Note also that Z_1 changes sign twice per period, in other words, alternates between inductive and capacitive reactance, as seen in Fig. 3.4. We define a "switching voltage" $V_S \simeq 2.44\,V_{CV}$ (note that it is different from the critical voltage) to correspond to the first maximum of Eq. (3.13). At V_S, the JJ impedance is very high. In the experiment on the inductively shunted junction (Chapter 5) this is the value of the AC drive voltage V_1 when the resonance frequency meets f_0.

The periodicity of the current with respect to V_1 can be seen to bear similarity with the well-known Shapiro steps. While the Shapiro steps appear in the DC current for certain DC voltages, there now occurs correspondingly a periodic structure in the AC response.

The described new phenomenon, let us call it "AC waves", cannot be observed directly in usual DC measurements. However, the predicted phenomenon was clearly detected in the measurements done in this thesis, which exclusively probe the system at the drive frequency.

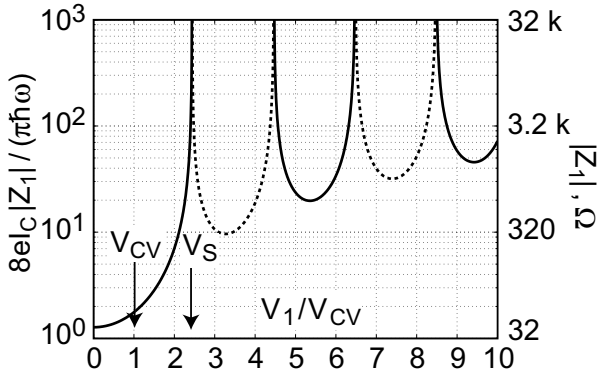

Figure 3.4: Absolute value of the JJ impedance, Eq. (3.13), plotted as a function of drive amplitude. Dashed lines mark areas where $\mathrm{Im}(Z_1)$ is negative. The critical voltage V_{CV} and switching voltage V_S are indicated. The rhs scale shows the impedance in Ω if $I_C = 50$ nA and $\omega/(2\pi) = 1$ GHz.

3.2 Experimental studies of driven Josephson junctions

In the experiments, the driven Josephson plasma resonance [42–44] was studied in the same experimental setup as the L-SET (see Figs. 2.6, 5.1). The appearance of the high-drive AC response in this scheme is calculated similarly to the response of the L-SET circuit, that is, the JJ impedance, Eq. (3.13) is inserted into the circuit formulae, equivalent of Eq. (5.7). Note that although in experiment we have an SCPT (double junction) in contrast to a single JJ, the former behaves effectively as a single, gate-tunable junction having the effective Josephson inductance L_J^*.

Let us now discuss the (AC) voltages in the L-SET circuit, Fig. 5.1 (a), using the same notation: Z_R is the resonator impedance without the coupling capacitor C_c, while Z is the total impedance when looking from the feedline. V_{in} (V_{out}) is the amplitude of the incoming (outgoing) voltage wave, and V_R is the voltage amplitude over the JJ.

It is important to realize that the physics as described previously is determined by V_R, while in experiment we are aware only of V_{in}.

Let us denote $V_0 = V_{\mathrm{in}} + V_{\mathrm{out}} = (1 + |\Gamma|)V_{\mathrm{in}}$. Division (or typically, amplification) of the voltages by the resonator used in the L-SET is then $V_R = V_0 Z/Z_R$, and hence

$$\frac{V_R}{V_{\mathrm{in}}} = (1 + |\Gamma|)\left|\frac{Z_R}{Z}\right| = \left|\frac{2Z_R}{Z + Z_0}\right|, \tag{3.15}$$

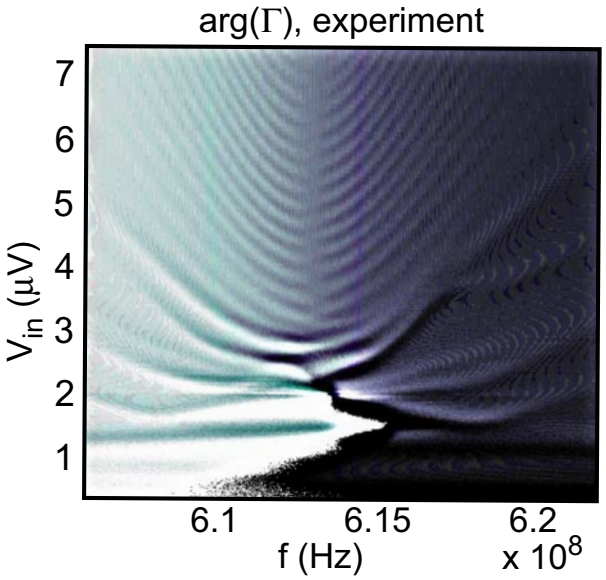

Figure 3.5: Contrast-enhanced plot portraying the AC-waves, here in arg(Γ) (the L-SET sample B) around the tank circuit resonance at $f_0 = 614.3$ MHz.

where we have used Eq. (2.1) for Γ. The voltage division, Eq. (3.15), is sensitive to the frequency and the internal quality factor Q_i of the resonator, which complicates the analysis. In the case relevant for our experiment, Eq. (3.15) reduces to a simple formula. At $V_R \gg V_{CV}$, $Q_i \sim 1000$ is very high and constant (because the dissipation within the SCPT is effectively cancelled), and the resonator becomes strongly overcoupled. It holds then at $f = f_0$ that $\mathrm{Re(Z_R)} \ll \mathrm{Im(Z_R)}$. Also, since $Z \sim 0$, $\mathrm{Im(Z_R)} = (\omega \mathrm{C_c})^{-1}$ and Eq. (3.15) yields

$$V_R = V_{\mathrm{in}} \frac{2}{\omega_0 C_c Z_0}. \tag{3.16}$$

When this is inserted into Eq. (3.13), the response, such as the AC waves, can be easily calculated as a function of the drive amplitude V_{in}.

The experimental data in Fig. 3.5 serves to verify the existence of the AC waves. The waves are curved because the voltage amplification decreases rapidly on both sides around f_0 (see Fig. 5.8).

In Fig. 3.6 (a), there are plotted data at a fixed frequency, and at two values of L_J^*. In accord with theory, the period does not noticeably depend on L_J^*. The data also verifies the concept of a critical voltage. The linear regime of plasma resonance ends at $V_C \sim 1\,\mu$V. The phase jumps roughly at $V_S \sim 2\,\mu$V. From Eq. (3.7) we find $V_{CV} = 2.4\,\mu$V for $\omega/(2\pi) = 730$ MHz. The measured value is low probably because of noise, see Sec. 5, which causes a

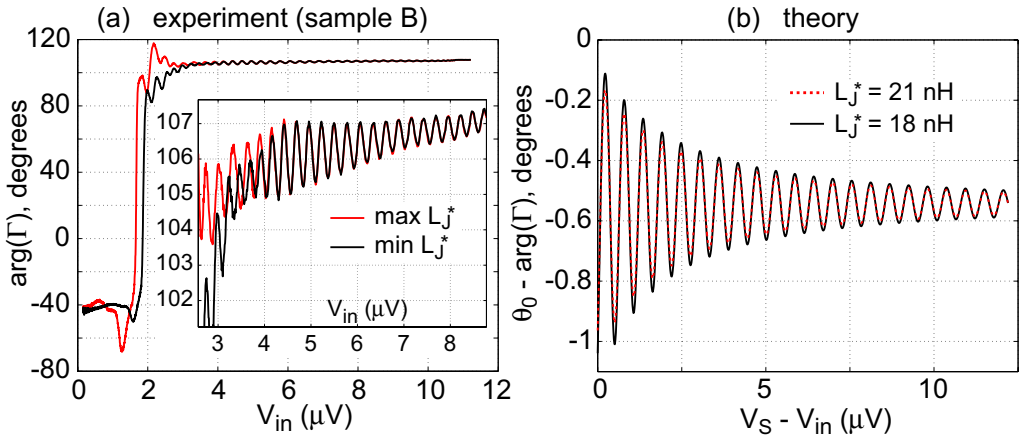

Figure 3.6: arg(Γ) plotted as a function of drive amplitude at fixed $f_0 = 614.3$ MHz, and at two extreme DC gate values. The inset is a magnification showing the AC waves of a JJ.

kind of "premature switching" having a direct correspondence to DC-biased junctions [45–47], as discussed in [P8] .

In Fig. 3.6 (b) is shown a corresponding calculation of the AC waves above the switching voltage V_S. When comparing theory and experiment, one sees that the theory predicts a period too large by a factor of 2. This can be due to the fact that the value of $V_{\rm in}$ is difficult to determine in experiment. Here it was deduced from the cable attenuation measured at room temperature, minus a 3 dB decrease towards the base temperature. The biasing scheme, though it alternates between voltage and current bias, however, should only have a minor effect according to the calculations (see Fig. 3.2).

Though some discrepancy remains, based on the qualitative similarity, we are confident that we have detected the new phenomenon describe above, the "AC waves" of a Josephson junction.

Chapter 4

Quantum mechanics of superconducting junctions

ALTHOUGH Josephson tunneling is a truly quantum-mechanical phenomenon in its microscopic origin, the degree of freedom due to quantum interference, the phase difference φ, typically obeys classical equations of motion [40]. This means that the operator properties of φ are of little significance. This was the approach of the previous Chapter 3.

However, it was realized in the 80's that φ can itself behave quantum-mechanically if disturbances from the environment are sufficiently attenuated [48, 49]. φ is then called a secondary macroscopic quantum variable. This limit was first encountered in Josephson junctions in the form of macroscopic quantum tunneling of the phase [50–52]. Energy-level quantization was discovered a few years later [53, 54].

In mid 90's it was verified indirectly in several experiments [55–57] that the ground state of a small superconducting grain can be a coherent superposition of macroscopically distinct states, a property predicted earlier by Averin and Likharev [58]. The latest breakthrough took place in 1999, when the time control a secondary macroscopic quantum state of the Cooper-pair box was demonstrated by Nakamura *et al.* [59]. This landmark work initiated an intense research aiming on constructing a quantum computer (see, e.g., Ref. [60]) based on the quantum states of Josephson junctions. These aspects are discussed in some detail in Secs. 5.4.1 and 6.2.

4.1 Single junction

A single JJ having the capacitance C and Josephson energy E_J (Fig. 4.1) has the Lagrangian function

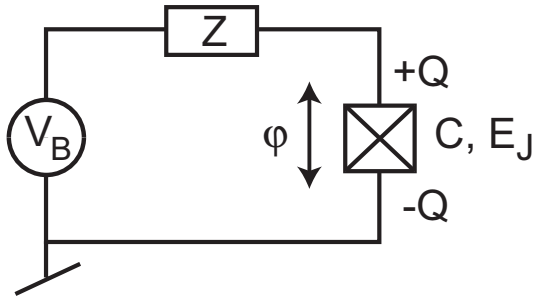

Figure 4.1: Schematics of a single Josephson junction in an electrical circuit having the impedance Z.

$$L = \frac{Q^2}{2C} + E_J \cos(\varphi). \tag{4.1}$$

In Eq. (4.1), we have implicitly chosen the last term as the potential energy. This is common practice though not the only possibility, since we are here dealing only with an analogy to mechanics. We choose the phase φ as the canonical coordinate. It is related to the magnetic flux through

$$\varphi = \frac{2\pi}{\Phi_0}\Phi \tag{4.2}$$

The "momentum" conjugate to φ is, according to definition, $p_\varphi = \partial L/(\partial\dot{\varphi}) = Q\Phi_0/(2\pi)$. Using the definition of the Hamiltonian, $H = p_\varphi\dot{\varphi} - L$, we immediately find $H = \frac{Q^2}{2C} - E_J\cos(\varphi)$. Note that simply writing $H = T - V$ does not make it immediately clear that charge and phase are the canonical coordinates, or, in what follows, the operators that do not commute.

According to the established recipe of canonical quantization, $Q\Phi_0/(2\pi)$ and φ are then replaced by the operators $\hat{\mathrm{Q}}\Phi_0/(2\pi)$ and $\hat{\varphi}$ that obey the commutation relations presented by Anderson [61]

$$\left[\left(\frac{\Phi_0}{2\pi}\right)\hat{\mathrm{Q}},\ \hat{\varphi}\right] = \left[\hat{\mathrm{Q}},\ \hat{\Phi}\right] = \mathrm{i}\hbar \ \Rightarrow\ \left[\hat{\mathrm{Q}},\ \hat{\varphi}\right] = 2e\mathrm{i}. \tag{4.3}$$

Eq. (4.3) means that the charge on a JJ and the phase difference across it are canonically conjugate variables in the same way as the momentum and the position of a particle are. This result was later justified to hold in spite of the inevitable coupling to microscopic sources of dissipation [62].

Defining phase as a time integral of voltage, $\varphi = (2\pi/\Phi_0)\int_0^t U(t')dt'$, Eq. (4.3) can be shown to hold not only for a JJ, but also more generally in electric circuits. The expectation values of charge and phase then obey the uncertainty principle

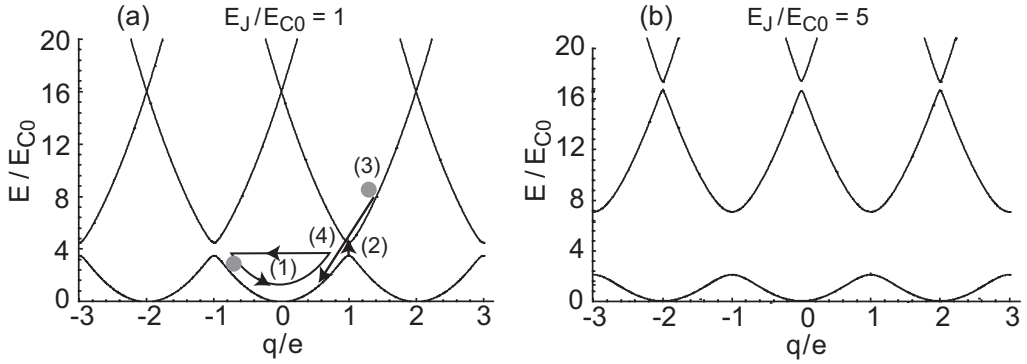

Figure 4.2: Energy bands of a single JJ calculated from Eq. (4.7). In (a), operation sequence of the Bloch Oscillating Transistor (BOT, see Sec. 4.3.2) is also shown.

$$\Delta Q\, \Delta\varphi \geq e. \tag{4.4}$$

Equation (4.4) can have substantial consequences if, by some means, fluctuations of either charge or phase are forced close to zero. This squeezing of quantum fluctuations of one quadrature at the expense of the other (see further discussion in Sec. 4.3) is another possibility to see secondary macroscopic quantum effects in a JJ, in addition to energy level quantization. This effect was observed experimentally in JJ systems in the late 80's [63–65].

Using $\hat{\mathrm{Q}} = -2e\mathrm{i}\frac{\partial}{\partial\varphi}$, the quantized Hamiltonian of a JJ is [66, 67]

$$\hat{H} = \frac{\hat{\mathrm{Q}}^2}{2C} - E_J\cos(\hat{\varphi}) = -4E_{C0}\frac{\partial^2}{\partial\hat{\varphi}^2} - E_J\cos(\hat{\varphi}), \tag{4.5}$$

where the single-junction charging energy is defined by $E_{C0} = e^2/(2C)$. Inserting the Hamiltonian into the Schrödinger eigenvalue equation $\hat{H}\Psi = E\Psi$ we obtain the Mathieu equation

$$4E_{C0}\frac{\partial^2\Psi(\varphi)}{\partial\varphi^2} + \left(E_J\cos(\varphi) + E\right)\Psi(\varphi) = 0. \tag{4.6}$$

Using $a = E/(4E_{C0})$, $-2p = E_J/(4E_{C0})$, and $\Phi(\varphi) = \Psi(2\varphi)$, this can be cast in the standard form of a Mathieu equation: $y''(z) + [a - 2p\cos(2z)]y(z) = 0$, and we get

$$\Phi''(\varphi) + \left(\frac{E}{4E_{C0}} + \frac{E_J}{4E_{C0}}\cos(2\varphi)\right)\Phi(\varphi) = 0. \tag{4.7}$$

The eigenvalues of Eq. (4.7) are the standard Mathieu function [68] characteristic values $a(q, p)$, where $q \in [-\infty, \infty]$. The new parameter q is called

"quasicharge". A few of the lowest bands are plotted in Fig. 4.2 for two E_J/E_{C0} ratios.

4.2 Cooper-pair transistor

A superconducting SET, or Bloch transistor, hereafter called the single Cooper-pair transistor (SCPT) [56, 69, 70], consists of two small Josephson junctions (Fig. 4.3). We denote by $C_\Sigma = C_1 + C_2 + C_g$ the island total capacitance, and d reflects the small asymmetry of the junction resistances. Unfortunately, different notations for E_J and E_C exist in the literature. Here, by E_J (with $d = 0$) we mean the Josephson energy of one junction, and $E_C = e^2/(2C_\Sigma)$ is the total charging energy of the SCPT.

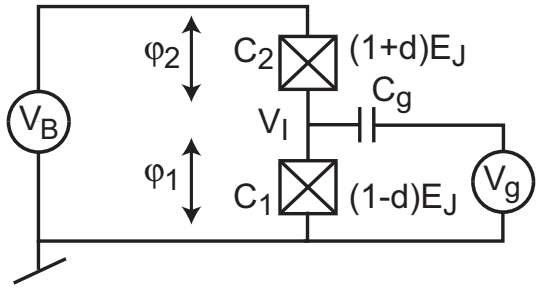

Figure 4.3: Schematics of the single Cooper-pair transistor. The junctions are allowed asymmetrical in their Josephson energies and capacitances.

Potential energy of the system in Fig. 4.3 is due to the Josephson energy:

$$V = -E_J(1-d)\cos(\varphi_1) - E_J(1+d)\cos(\varphi_2). \tag{4.8}$$

The phase across the transistor $\varphi = \varphi_1 + \varphi_2$ is assumed to be a classical control parameter, which means that the environment should have a sufficiently low impedance to fix the phase. A second quantity which does not have such a constraint is defined as $\theta = \frac{1}{2}(\varphi_2 - \varphi_1)$. We choose θ as the canonical coordinate. Its conjugate variable p_θ is then a number operator corresponding to the excess number of particles on the island.

Phases over the junctions can now be written as $\varphi_1 = \frac{1}{2}\varphi - \theta$, and $\varphi_2 = \frac{1}{2}\varphi + \theta$. Making this change of variables in Eq. (4.8) we find

$$V = -2E_J\cos(\varphi/2)\cos(\theta) + 2dE_J\sin(\varphi/2)\sin(\theta). \tag{4.9}$$

Electric field energy in the three capacitors is the kinetic energy:

$$T = \frac{1}{2}C_1V_I^2 + \frac{1}{2}C_2(V_B - V_I)^2 + \frac{1}{2}C_g(V_g - V_I)^2. \tag{4.10}$$

We substitute Eq. (4.10) with $V_I = \hbar/(2e)\dot{\varphi_1} = \hbar/(2e)(\frac{1}{2}\dot{\varphi} - \dot{\theta})$, and $V_B = \hbar/(2e)\dot{\varphi}$. The momentum conjugate to θ is by definition $p_\theta = \partial L/(\partial\dot{\theta}) = \partial T/(\partial\dot{\theta})$. Here, the Lagrangian is $L = T - V$. Calculating p_θ using Eq. (4.10) and solving for $\dot{\theta}$ we get

$$\dot{\theta} = \frac{\dot{\varphi}(C_1 - C_2 + C_g) - 2C_g V_g(2e)/\hbar + 2p_\theta(2e)^2/\hbar^2}{2C_\Sigma}. \tag{4.11}$$

We aim at the Hamiltonian $H = p_\theta\dot{\theta} - L$. We insert Eq. (4.11) into Eq. (4.10), and after substantial algebra the result simplifies into

$$\begin{aligned} H = \frac{((2e)p_\theta/\hbar - C_g V_g)^2}{2C_\Sigma} - 2E_J\cos\left(\frac{\varphi}{2}\right)\cos(\theta) + \\ + 2dE_J\sin\left(\frac{\varphi}{2}\right)\sin(\theta) - \frac{1}{2}C_g V_g^2, \end{aligned} \tag{4.12}$$

where it is assumed that $V_B = 0$. The case of small bias corresponds to making the Born-Oppenheimer approximation [71], so that the fast degrees of freedom (θ, p_θ) are assumed to be decoupled from the slow ones controlled by the external circuit. This is quite well justified, since the relevant frequencies we use for driving φ in the experiment on the inductively read Cooper-pair transistor (L-SET, see Sec. 5) are of the order ~ 1 GHz, while the scale for the fast variables is $\sim E_C \sim 20$ GHz.

p_θ and θ are then substituted via the number and phase operators, $\hat{n} \equiv 2\hat{p_\theta}/\hbar$ and $\hat{\theta}$, respectively. We further define the reduced gate voltage $q_g \equiv C_g V_g/e$. Then,

$$\hat{H} = E_C(\hat{n} - q_g)^2 - 2E_J\cos\left(\frac{\varphi}{2}\right)\cos(\hat{\theta}) + 2dE_J\sin\left(\frac{\varphi}{2}\right)\sin(\hat{\theta}) - \frac{1}{2}C_g V_g^2. \tag{4.13}$$

For numerical diagonalization, the Hamiltonian is usually written in the eigenbasis of $\hat{n}$ which is denoted as $|n\rangle$. Using $\exp(\pm i\hat{\theta})|n\rangle = |n \pm 1\rangle$ and dropping the constant term in Eq. (4.13), the Hamiltonian of an SCPT is written as

$$\begin{aligned} \hat{H} = \sum_n \Big\{ E_C(n - q_g)^2|n\rangle\langle n| - \left(E_J\cos\left(\frac{\varphi}{2}\right) - \mathrm{i}dE_J\sin\left(\frac{\varphi}{2}\right)\right)|n\rangle\langle n+1| \\ - \left(E_J\cos\left(\frac{\varphi}{2}\right) + \mathrm{i}dE_J\sin\left(\frac{\varphi}{2}\right)\right)|n+1\rangle\langle n| \Big\}, \end{aligned} \tag{4.14}$$

which is convenient for numerical calculations. The required number of charge states is at least $n > \max\{5, E_J/E_C\}$. Note that asymmetry in the junction capacitances cancels in Eq. (4.14). The asymmetry in Josephson energies, $d \neq 0$, turns out to lift the degeneracy between the bands $n = 0$ and $n = 1$ at $\varphi = \pm\pi$, $q_g = \pm 1$, and it is important only for $E_J/E_C \gtrsim 1$. A gallery of the first two bands of an SCPT at different E_J/E_C is shown in Fig. 4.4.

Provided $E_J/E_C \ll 1$, Eq. (4.14) with $d = 0$ can be diagonalized analytically using a two charge state restriction [72]. The band energies are then given by [70]:

$$E_{0,1} = E_C(q_g^2 - 2q_g + 2) \mp \sqrt{\left(E_J \cos(\varphi/2)\right)^2 + \left(2E_C(1 - q_g)\right)^2} \qquad (4.15)$$

More or less direct evidence of the band structure due to macroscopic quantum coherence of charge has been obtained in experiment since the mid-90's in the frequency domain [57, 69, 73]. Corresponding properties have also been demonstrated for the phase degree of freedom [74, 75].

4.3 Environmental effects on Cooper-pair tunneling

In the previous two sections, quantum mechanics of Cooper-pair tunneling was discussed without paying attention to the external impedance Z (as in Fig. 4.1), thus in effect putting $Z = 0$. However, in practice this condition is never fully satisfied. At the relevant frequencies $\sim 1\ \mathrm{K}/h \sim 20\ \mathrm{GHz}$, Z is typically real and of the order the impedance of free space $\sqrt{\mu_0/\epsilon_0} \approx 377\,\Omega$, and thus the interaction and energy exchange between tunneling Cooper pairs and the environment can add significant terms into the Hamiltonian. A full quantum-mechanical treatment of the system of the JJ plus the circuit is then needed [76].

4.3.1 $P(E)$-theory

It can be shown that the probability $P(E)$ that a tunneling Cooper pair exchanges an energy E with Z is [77, 78]

$$P(E) = \frac{1}{2\pi\hbar} \int_{-\infty}^{\infty} dt \exp\left[4J(t) + \mathrm{i}Et/\hbar\right], \qquad (4.16)$$

where the phase correlator $J(t) \equiv \langle\varphi(t)\varphi(0)\rangle - \langle\varphi(0)\varphi(0)\rangle$ becomes

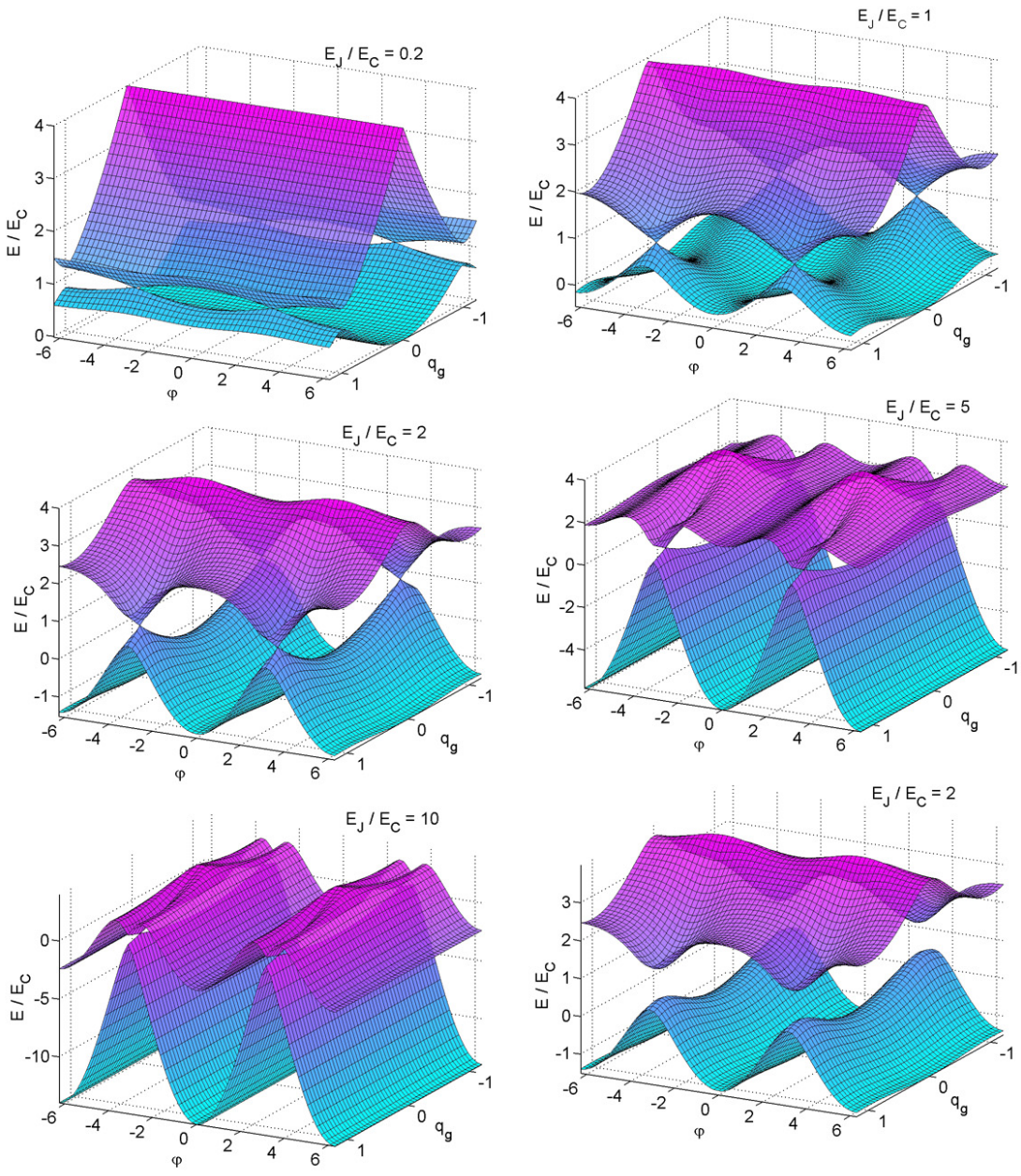

Figure 4.4: Two lowest energy bands E_0 and E_1 of the single Cooper-pair transistor, calculated from Eq. (4.14), for the indicated E_J/E_C ratios. Except for the lowest graph on the rhs ($d = 0.2$), all the graphs are for symmetric SCPT, i.e., with $d = 0$.

$$J(t) = 2\int_0^\infty \frac{d\omega}{\omega}\frac{\mathrm{Re(Z}(\omega))}{R_K}\left\{\coth(\hbar\omega/(2k_BT))[\cos(\omega t)-1] - \mathrm{i}\sin(\omega t)\right\}. \tag{4.17}$$

The tunneling current of Cooper pairs can now be expressed as

$$I(V) = \frac{\pi e E_J^2}{\hbar}\left(P(2eV) - P(-2eV)\right), \tag{4.18}$$

where the first and the second terms represent the tunneling Cooper pair emitting or absorbing the energy $E = 2eV$, respectively.

We thus see that via the phase correlation function, Eq. (4.17), the tunneling supercurrent carries information about the spectrum of environmental dissipation [79, 80]. This has been applied in [P4] to study the energy levels of a mesoscopic SQUID.

4.3.2 Applications of an isolated junction

The band structure of a single JJ becomes particularly apparent if charge fluctuations are suppressed by a high resistance of the environment, $\mathrm{Re}(Z) \gg R_Q = h/(4e^2) \simeq 6.5$ kΩ. According to the uncertainty principle, Eq. (4.4), phase is then strongly fluctuating. The Coulomb blockade of Cooper-pair tunneling is important under these conditions [81–83]. Transport involves a cycle of Bloch oscillations [67, 84], where the quasicharge oscillates back and forth in the first Brilloun zone. The voltage across the JJ, $V_I = dE/dq$, oscillates also. However, if $V_I < \max(dE/dq) \equiv V_{CB}$, which defined the Coulomb blockade voltage V_{CB}, the current does not flow.

The Bloch oscillating transistor (BOT)

A low-noise current amplifier based on "band engineering" of a secondary macroscopic quantum degree of freedom, namely the discussed band structure of an isolated JJ, was suggested in Ref. [85] and implemented as a part of this work in [P3]. Further analysis of the device is in Refs. [86–88]. The operation sequence of the BOT was illustrated previously in Fig. 4.2 (a), which is used here as a reference.

In short, the cycle of Bloch oscillations (1) becomes occasionally stopped if Zener tunneling (2) to the second band happens, where the system remains Coulomb blockaded (3) if the transport voltage is suitably chosen, i.e., if $V_c < V_{CB}$. The cycle of Bloch oscillations can be recovered by injecting a

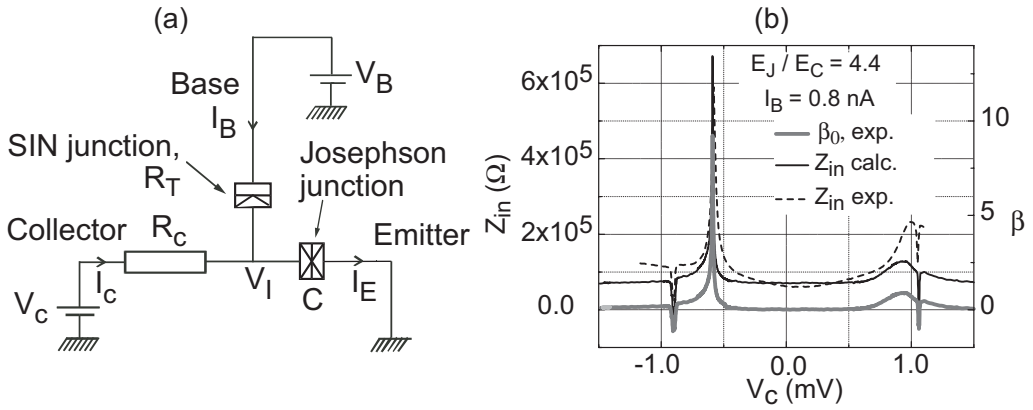

Figure 4.5: (a) Schematics of the Bloch oscillating transistor (BOT); (b) measured input impedance, compared to the presented model. The active bias region is around -0.6 mV where the quantities peak.

quasiparticle into junction (4), because this corresponds to relaxation. Current gain $\beta_0 = \Delta I_c/(\Delta I_B)$ comes from the number Bloch oscillation cycles, each transferring a charge of $2e$, triggered by a single quasiparticle.

The actual device consists of a JJ, an SIN junction, and a high resistance $R_c \gg R_Q$ to suppress fluctuations of charge on the JJ. The SIN junction serves as the injection junction of the control quasiparticles mentioned, and therefore it is the logical input of the device.

Next we will briefly show how the BOT can be handled as a general three-terminal device, neglecting its exotic internal operation principle. With the symbol definitions as in Fig. 4.5 (a), we get

$$R_c I_c = V_c - V_I \tag{4.19}$$
$$R_T I_B = V_B - V_I \tag{4.20}$$

The input impedance is defined as $Z_{\rm in} = \partial V_B/(\partial I_B)$. We find $\partial V_B/(\partial I_B) = R_T + R_c \partial I_c/(\partial I_B)$, and hence

$$Z_{\rm in} = R_T + \beta_0 R_c. \tag{4.21}$$

Equation (4.21) is compared to experimental data in Fig. 4.5 (b). The values of $Z_{\rm in}$ and β_0 were measured by applying a small AC excitation and measuring the response in accord to the definition of the quantities. A good agreement of independently determined β_0 and $Z_{\rm in}$ shows that BOT is a device with an "intermediate" input impedance around ~ 1 MΩ, in between the corresponding values for the SET [89] (high $|Z_{\rm in}| \sim 1$ GΩ), and the

SQUID [90] (low $|Z_{\rm in}| \sim 1\,\Omega$). This makes it suitable for general readout applications in mesoscopics, where quite often the impedance levels are in the range considered.

Noise spectroscopy

Conductance in the blockade region, $V_I < V_{CB}$, is highly sensitive to fluctuations. The conductance has been predicted to increase as a power law as a function of temperature [91] having an exponent of $2\rho-2$, where $\rho = R_c/R_Q$, due to noise in R_c. Therefore, if $\rho \gg 1$, conductance is highly sensitive to noise and can be used for noise detection in general [92]. Recently, the study of higher moments of noise [93–95] has attracted a plenty of attention, since noise provides further information, not carried by the first moments (the average voltage and current), of the transport processes [96].

An intuitively appealing picture for noise detection using a Coulomb-blockaded JJ is then to add a noise temperature T_N due to the external noise to the physical temperature T. Conductance would then be proportional to $\propto (T + T_N)^{2\rho-2}$. In the case that the external noise is shot noise, as in the setup of Fig. 4.5 (a), where the SIN junction serves as the shot noise source, the contribution $J_N(t)$ to the phase correlator due to the shot noise is [97]

$$J_N(t) = \frac{\pi I_B}{e}\left(\frac{R_c}{R_Q}\right)^2 \int_0^\infty \frac{d\omega}{\omega^2}\frac{\cos(\omega t)-1}{1+(\tau\omega)^2}, \tag{4.22}$$

where $\tau = R_c C$. Consequently, $T_N = eI_B R_c/(2k_B)$.

However, in the relevant case $\rho \gg 1$, the simple picture fails because of asymmetry (the non-Gaussian property) of the shot noise. Indeed, as shown in Ref. [98], the effect of the shot noise then becomes sensitive to exactly these properties and can be used for their study. The following effects are expected according to the theory [98]; the increase of zero-bias conductance G from a "background" G_0 should be linear in the shot noise power:

$$G = G_0 + \frac{\pi^{5/2}}{32\sqrt{2\ln(\rho)}}\left(\frac{E_J}{E_{C0}}\right)^2 \frac{e}{E_{C0}}\rho^{3/2}|I_B|. \tag{4.23}$$

The conductance should also become asymmetric such that there is an extremum at the transport voltage V_c given by

$$V_c = \mathrm{sign}(I_S)\frac{2E_{C0}\ln(\rho)}{\pi^2 e\rho}. \tag{4.24}$$

Although the shot noise pulses do not flow through the JJ, they act as a kind of conveyor belt to make the JJ conduct during them. The third effect hence carries the name "ratchet effect", and it contributes a DC current

$$I_{DC} = \frac{\pi^2}{32}\left(\frac{E_J}{E_{C0}}\right)^2 \rho I_B. \tag{4.25}$$

It is worth pointing out that the present method does not allow to separate the effect of the different higher moments $\langle \delta I^n \rangle$ where $n > 2$, but it provides the important information that some of them are non-zero.

In order to observe the delicate effects of shot noise in experiment, special attention should be paid to filtering of external noise. Indeed, in a setup other than that in Fig. 2.2, which was lacking a low-temperature voltage division and powder filters, the ratchet effect was found to be masked by external noise.

In the best DC configuration, Fig. 2.2, all of the three mentioned effects were observed, in a fair agreement with the expectations, as reported in [P11]. The good agreement provides overwhelming evidence of the picture of uncorrelated, non-Gaussian shot noise.

4.4 Interband (Landau-Zener) tunneling

A two-level quantum system may change its state if the level spacing $\omega_{01} = E_1 - E_0$ depends on time [99,100] (note that in Ref. [100], the minimum band gap is denoted by $2V$). The probability of this (Landau-) Zener tunneling is:

$$P_Z = \exp\left(\frac{-\pi(\hbar\Omega_{01})^2}{2\hbar D\dot{\varphi}}\right) \tag{4.26}$$

where Ω_{01} is the minimum of ω_{01} in the parameter space, and $D = \hbar\,\partial\omega_{01}/\partial\varphi$. Operation principle of the BOT (Sec. 4.3.2) is based on using this basic property of two-level quantum systems. For a single isolated JJ, the probability of Zener tunneling becomes exponentially small if $E_J/E_{C0} \gtrsim 1$ because ω_{01} grows.

In a second device application discussed in this work, namely the L-SET (see the next chapter), non-adiabaticity would be *harmful* for operation in the regime of small oscillations. Since the operation of the L-SET happens close to $q_g = \pm 1$ and $\varphi = \pm\pi$, where the two lowest bands 0 and 1 of a symmetric SCPT are degenerate and hence ω_{01} is small, adiabaticity is an important issue to consider. In Fig. 4.6 (a) we plot the quantities Ω_{01}, Ω_{01}^2, and D computed numerically from the two lowest bands of SCPT, at the optimal gate DC working point which maximizes the L-SET transfer function. We may see that D reduces faster towards small E_J/E_C than Ω_{01}^2.

We thus have the somewhat counterintuitive result that in the case of the L-SET, Zener tunneling is exponentially suppressed in the most interesting

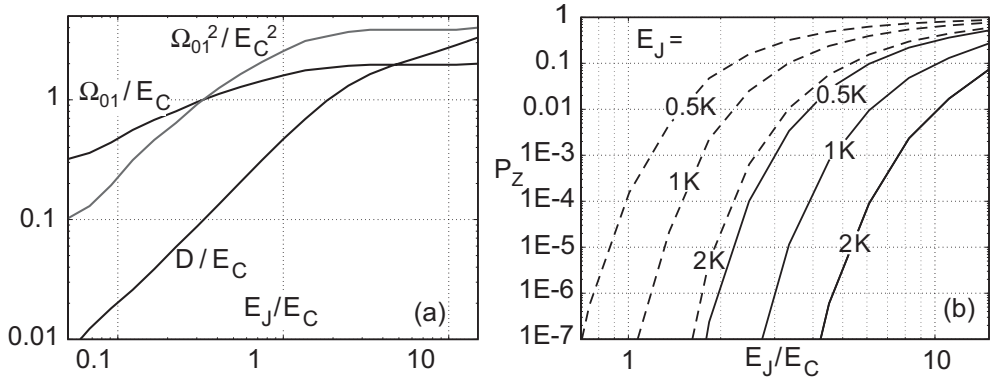

Figure 4.6: (a) Minimum band gap between two lowest bands (Ω_{01} and Ω_{01}^2), and difference of their derivatives (D), at the L-SET optimal working point; (b) the corresponding Zener tunneling probability supposing a 2π p-p drive. Full lines: $f_p = 1$ GHz. Dashed lines: $f_p = 5$ GHz.

case of low E_J/E_C (Fig. 4.6 (b)), and is therefore of little harm for the LSET in the regime of small oscillations.

Chapter 5

Quantum inductance

JOSEPHSON junctions store energy in the form of inertia of the flow of Cooper pairs. Thereby, they can be used as reactive circuit components. Whether a circuit containing JJs appears as an inductive or capacitive reactance, depends on the point of observation in the circuit, and whether the drive is in the linear regime or not. From the Josephson equations we find $V = \hbar\dot{I}/(2eI_C\cos(\varphi))$ which means that a JJ behaves as a nonlinear inductor,

$$L_J(\varphi) = \frac{\hbar}{2eI_C\cos(\varphi)}. \tag{5.1}$$

Let us denote the value $L_J(\varphi = 0)$ simply by L_J. The following linear-regime relations are useful:

$$E_J = \frac{h\Delta}{8e^2R_T} \tag{5.2}$$

$$I_C = \frac{2e}{\hbar}E_J = \frac{2\pi}{\Phi_0}E_J = \frac{\pi\Delta}{2eR_T} \tag{5.3}$$

$$L_J = \frac{\hbar}{2eI_C} = \frac{\Phi_0}{2\pi}\frac{1}{I_C} = \left(\frac{\Phi_0}{2\pi}\right)^2\frac{1}{E_J} \tag{5.4}$$

In general, a system which has an inductance defined via $V = \dot{\Phi} = L\dot{I}$ may feature an arbitrary dependence of the energy on phase $E(\varphi)$, where $\varphi = (2\pi/\Phi_0)\Phi$ (for a classical JJ, $E(\varphi) = -E_J\cos(\varphi)$, but quantum effects may renormalize this expression as shown in the following). Changes of flux and energy are then related by $dE = Id\Phi$. We then have immediately

$$L = \left(\frac{d^2E}{d\Phi^2}\right)^{-1} = \left(\frac{\Phi_0}{2\pi}\right)^2\left(\frac{d^2E}{d\varphi^2}\right)^{-1}. \tag{5.5}$$

In the rest of this chapter, we will apply this general concept of inductance to a secondary quantum-mechanical object, namely the band structure of the single Cooper-pair transistor. Relying on these results, we will establish a device application for extremely sensitive and fast measurement of the electric charge. We call this device "L-SET" (L for inductive), much in the same way as the inductively read nonhysteretic RF-SQUID [101–105] has been coined "L-SQUID" [90].

5.1 Inductance of the single Cooper-pair transistor

In short, the principle of the L-SET is to tune the resonant frequency of the circuit shown in Figs. 2.6 and 5.1 (a) by gate modulation of the effective Josephson inductance L_J^* of an SCPT:

$$L_J^* = \left(\frac{\Phi_0}{2\pi}\right)^2 \left(\frac{d^2 E_0}{d\varphi^2}\right)^{-1}. \tag{5.6}$$

Here, we have supposed adiabatic operation at the lowest energy band E_0 of the SCPT. The SCPT is coupled in parallel to an LC oscillator resonant at the frequency $f_0 = 1/(2\pi)(LC)^{-1/2}$, roughly at 600 MHz in our experiments. The total system has a gate-dependent plasma resonance at $f_p = 1/(2\pi)(L_{\rm tot}C)^{-1/2} > f_0$, where $L_{\rm tot} = L \parallel L_J^*$.

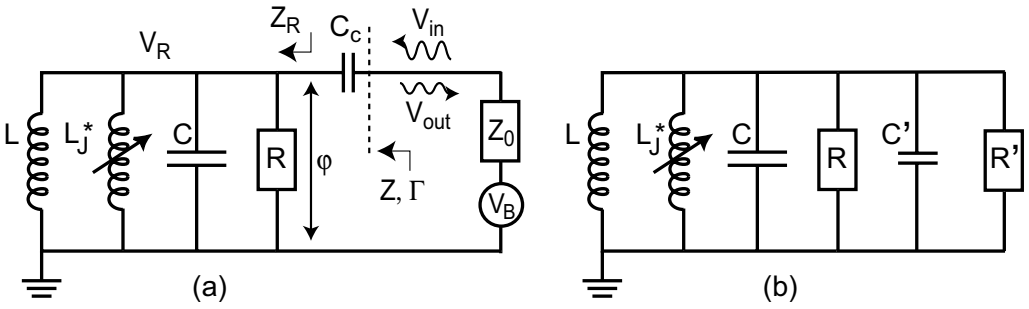

Figure 5.1: (a) The L-SET circuit; (b) an equivalent circuit (without bias).

In Fig. 5.2 we plot the second derivative of E_0 with respect to the phase. According to Eq. (5.6), L_J^* is inversely proportional to this quantity. As seen in the figure, L_J^* can have a sharp dependence on both control parameters, φ and q_g. Here, however, the phase dependence is not relevant because φ is used for drive.

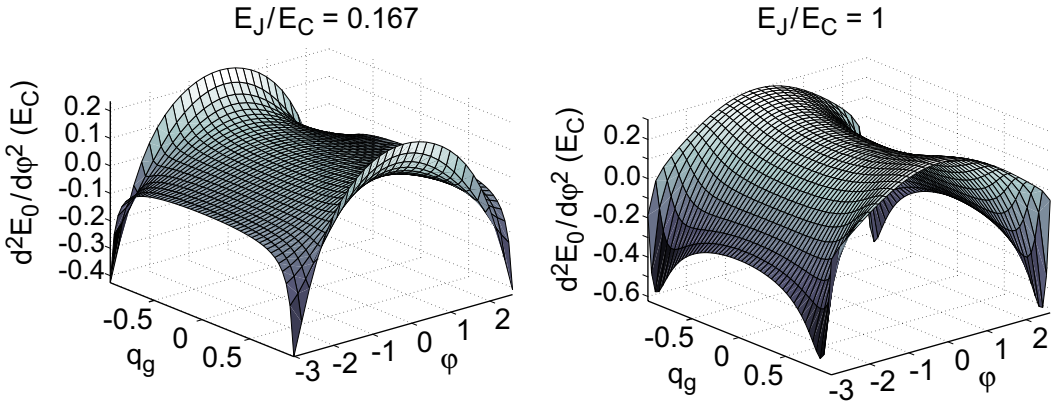

Figure 5.2: Second derivative of E_0 with respect to φ of the SCPT lowest band, at $E_J/E_C = 0.167$ (left) and $E_J/E_C = 1$ (right). The axes have been truncated before $q_g = \pm 1$ and $\varphi = \pm\pi$ to avoid divergencies.

If we choose $L \gtrsim L_J^*$ and $E_J/E_C \lesssim 1$, f_p in the L-SET layout is highly sensitive to the gate charge q_g, easily having a peak-to-peak modulation of hundreds of MHz. This may be appreciated by examining Figs. 5.3 (a) and 5.4 (a) which display the gate dependence of L_J^*.

Note that a simple way of interpreting the inductance modulation as arising from the well-known gate modulation of the critical current of an SCPT [69,70,106,107], giving rise to modulation of the Josephson inductance via the first form of Eq. (5.4), is not correct. The critical current I_C^* and the Josephson inductance L_J^* of an SCPT are not linked as simply as in Eq. (5.4) which holds only for a sinusoidal energy vs. phase relationship, and deviations from it are significant if $E_J/E_C \lesssim 1$.

5.2 L-SET circuit

Charge detection is performed by exposing the L-SET circuit, via the coupling capacitor C_c, to monochromatic microwaves of an amplitude $V_{\rm in}$ and a frequency $\sim f_p$. The voltage reflection coefficient Γ, Eq. (2.1), then depends on the impedance of the circuit,

$$Z = \frac{1}{\mathrm{i}\omega C_c} + \left(\mathrm{i}\omega C + \frac{1}{\mathrm{i}\omega L} + \frac{1}{\mathrm{i}\omega L_J^*} + \frac{1}{R}\right)^{-1}, \tag{5.7}$$

and the reflected voltage wave $V_{\rm out} = |\Gamma| V_{\rm in} \cos(\omega_p t + \arg(\Gamma))$ consequently carries information about L_J^*. Notice that the tank resonator is not similarly necessary for doing an impedance match as in the RF-SET. Namely, at low

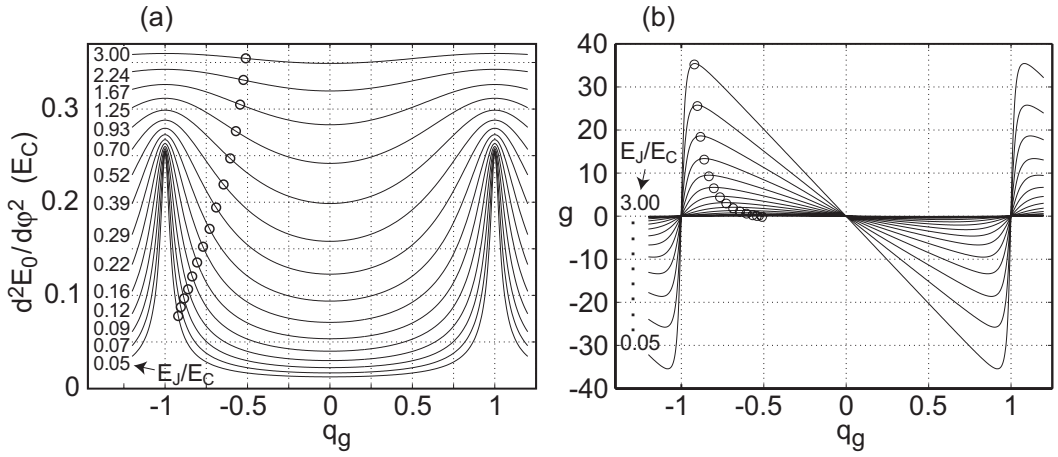

Figure 5.3: (a) Second derivative of E_0 with respect to φ of the SCPT lowest band at $\varphi = 0$, for logarithmically spaced values of E_J/E_C; (b) the electrometer gain g, Eq. 5.14, for the same values of E_J/E_C. The circles mark the optimal gate DC operation points which maximize g.

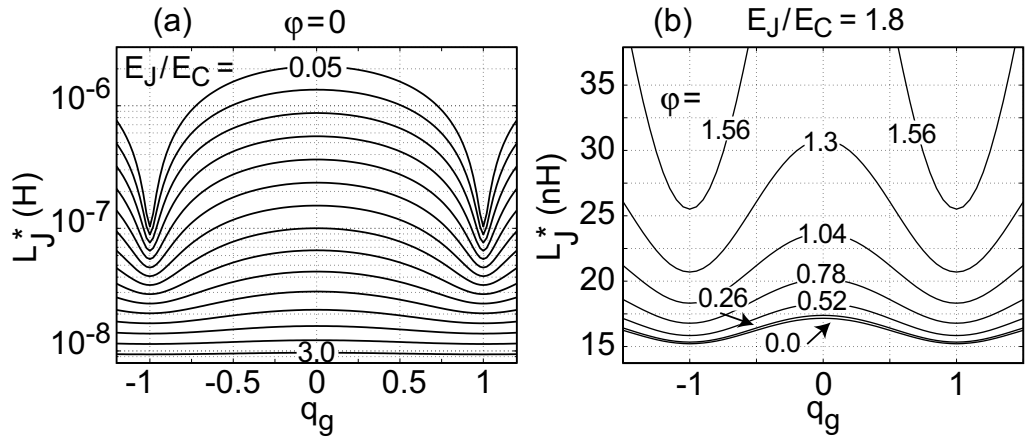

Figure 5.4: (a) Josephson inductance at $\varphi = 0$ of a typical SCPT made of Al ($E_J \times E_C = 1.8$ K^2). The curves are for the same values of E_J/E_C as in Fig. 5.3 (a), but now from bottom to top. (b) L_J^* at different values of phase bias, for $E_J/E_C = 1.8$.

energies when the SCPT behaves as an inductance, typically $L_J^* \sim 10-50$ nH, its impedance is close to the typical transmission line impedance $Z_0 = 50\,\Omega$ for $f_p \sim 1$ GHz.

The resonator has, nevertheless, an important role in filtering out the noise both at low and high frequencies. Without filtering, even thermal noise of Z_0 at $T = 50$ mK, over $B = 10$ GHz, would cause noise $\delta V_{\rm in} =$

$\sqrt{4k_BTZ_0B} \sim 1\mu$V. Depending on the circuit, this would then convert into a voltage over the SCPT of the order the critical voltage V_{CV} (see Eq. 3.7), which is clearly intolerable.

It can be useful to convert the actual L-SET circuit, loaded by the external $50\,\Omega$ via the coupling capacitor (Fig. 5.1 (a)) into an equivalent parallel resonator (Fig. 5.1 (b)). Component values of the equivalent circuit are given by

$$C' = \frac{C_c}{\omega^2 C_c^2 Z_0^2 + 1} \simeq C_c \tag{5.8}$$

$$R' = Z_0 \left(1 + \frac{1}{\omega^2 C_c^2 Z_0^2}\right) \simeq \frac{1}{\omega_0^2 C_c^2 Z_0}. \tag{5.9}$$

The resonant frequency is shifted from $\omega_0 = (L_{\rm tot}C)^{-1/2}$ because C_c becomes approximately added in parallel with C as shown in Fig. 5.1. By differentiation we get $d\omega_0/(dC) = -\omega_0/(2C)$, and a relation is written for the loaded resonance frequency $\omega_p = \omega_0 - d\omega_0 = \omega_0(1 - dC/(2C))$:

$$f_p = f_0 \left(1 - \frac{C_c}{2C(Z_0^2(2\pi f_p)^2 C_c^2 + 1)}\right) \simeq f_0 \left(1 - \frac{C_c}{2C}\right). \tag{5.10}$$

If $C_c < 0.1C$, the last form of Eq. (5.10) is accurate to within 0.5 %. A further correction is due to finite quality factor, which decreases f_p in Eq. (5.10) by a factor $\alpha \equiv \sqrt{1 - \frac{1}{4Q_L^2}} \simeq 1 - \frac{1}{8Q_L^2}$, which implies here, however, a shift of only a few hundred kHz for a typical $Q_L \sim 15$.

A short expression of the full loaded resonance frequency, accurate enough for all calculations does not seem to exist. In practice, it is calculated numerically from the first form of Eq. (5.10), multiplied by α (note that Q_L depends on f_p).

Classical dynamics of the phase φ in the L-SET setup can be understood using the concepts of the familiar RCSJ model [108,109]. Now, however, there is a parabolic background $U_L = \Phi^2/(2L)$ (we also define $E_L = \Phi_0^2/(8\pi^2 L)$) in the potential due to the shunting L (see Fig. 5.5), and in the absence of a bias the potential is

$$U = U_L + E_0 \simeq \frac{\Phi_0^2}{8\pi^2 L}\varphi^2 - E_J^* \cos(\varphi). \tag{5.11}$$

Note that this is not exact because even the lowest band of the SCPT deviates from sinusoidal, but the error is typically a few %. It has been discovered in this work that a "switching" resembling that of a DC-biased junction happens

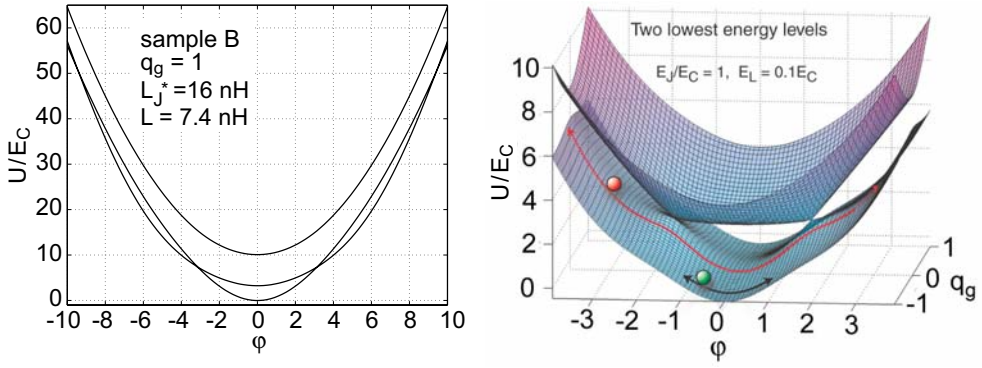

Figure 5.5: Potential experienced by the fictitious phase particle in the L-SET setup, with three (two) lowest bands of the SCPT included on left (on right). Left: Eq. (5.11) plotted using parameters of sample B ($E_J^*/E_L \sim 1.0$); Right: Classical picture of the phase dynamics. "Anharmonic mode" of non-linear oscillations is also illustrated.

in the "RCLSJ" -model (similar findings in a slightly different system were recently reported in Refs. [110, 111]). Now, however, the phenomenon is in AC, and it happens at a certain critical voltage (not current) given by Eqs. (3.4), (3.5), depending on the biasing scheme. The dynamics are analyzed in more detail in Publications [P7] and [P8] in terms of experimental data, analytical calculations, and simulations.

5.3 Charge sensitivity

We will now consider the charge sensitivity s_q possible to achieve using the L-SET. We treat only the regime of harmonic oscillations (accurate considerations of sensitivity in the "anharmonic" mode are left for future research). The way to think is in accord to the analysis presented in the literature for the sequential tunneling SET, or for that in the RF-SET mode [112–115].

We aim at finding out what would be the noisy gate charge (with the amplitude spectral density s_q) that would cause the amount of voltage noise detected in our spectrum analyzer. In other words, we convert the detected voltage noise (amplitude spectral density s_V) to the input of our L-SET.

In principle, one could read either amplitude or phase of the reflected wave. Here we find that the optimal figures of merit are the same for both cases; therefore, we concentrate on the amplitude readout which allows for an important analytical derivation. We suppose the detection of one sideband. For amplitude readout, we thus have to evaluate [P10] , [115]

$$s_q = \frac{s_V}{\frac{\partial V_{\rm out}}{\partial q_g}} = \frac{\sqrt{2k_B T_N^* Z_0}}{V_{\rm in}\frac{\partial|\Gamma|}{\partial q_g}} \tag{5.12}$$

where T_N^* is the equivalent noise temperature referred to 1st stage amplifier input, consisting of noise due to both the resonator itself, and the amplifier contribution T_N. As argued in [P10] , the sample noise is negligible, that is, $T_N^* \simeq T_N$.

Unfortunately, the analysis turns out to be complicated, for two main reasons. First, the circuit is more complex than in the RF-SET for instance. Second, the modulation depth of the SCPT Josephson inductance is a non-trivial function which needs to be calculated numerically from the band structure of a SCPT, for a given E_J/E_C. The final results are not easy to interpret in terms of simple arguments.

5.3.1 Transfer function

We begin by decomposing the "gain" derivative in the second form of Eq. (5.12) into terms that are conveniently substituted for terms due to the tank circuit and SCPT:

$$\frac{\partial|\Gamma|}{\partial q_g} = \frac{\partial|\Gamma|}{\partial\omega_p}\frac{\partial\omega_p}{\partial L_J^*}\frac{\partial L_J^*}{\partial q_g}. \tag{5.13}$$

The last derivative $\partial L_J^*/\partial q_g$ in Eq. (5.13) is due to the SCPT band structure. It is useful to scale it into dimensionless form. Then it will be called the electrometer gain, or transfer function. Several possible normalizations exist; we will mention two of them.

$$g \equiv \frac{\partial L_J^*}{\partial q_g}\frac{e}{L_{J0}} = \frac{\partial}{\partial q_g}\left(\frac{\partial^2 E_0}{\partial\varphi^2}\right)^{-1}\frac{e}{L_{J0}} \tag{5.14}$$

is scaled according to the minimum (vs. gate, at $q_g = \pm 1$; see Fig. 5.4 (a)), $L_{J0} \equiv \min\left(\frac{\partial^2 E_0}{\partial\Phi^2}\right)^{-1}$ of the SCPT Josephson inductance. It is the derivative of inductance modulation of Fig. 5.3 (a), and its gate dependence is plotted in Fig. 5.3 (b). Alternatively, $\overline{g} \equiv \frac{\partial L_J^*}{\partial q_g}\frac{e}{L_J^*}$, which is scaled according to the value of SCPT Josephson inductance at the (best) *operation point*.

As evident in Fig. 5.3 (a), (b), the gain has a strong gate dependence and it also grows rapidly for $E_J/E_C \lesssim 1$, when the Coulomb effect is strong. We denote its maximum value with respect to gate by g_m, that occurring at the values of q_g marked by circles in Fig. 5.3. As seen in Fig. 5.6 (a), g_m grows fast, like $(E_J/E_C)^{-1}$ at low E_J/E_C, which favors a low E_J/E_C for a

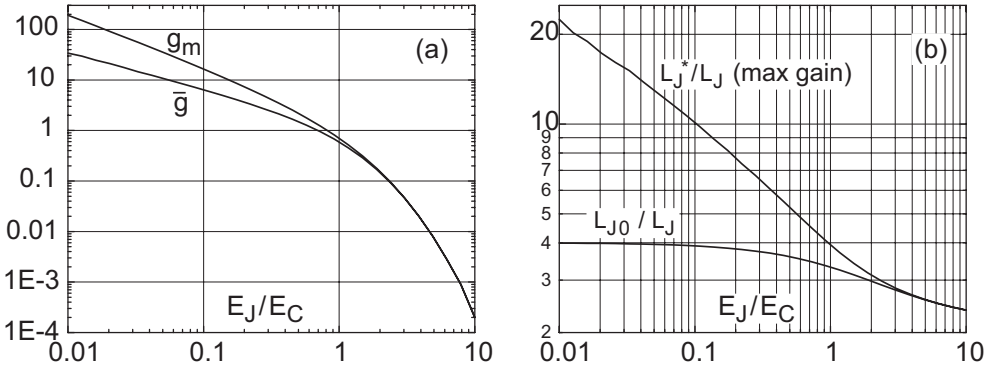

Figure 5.6: Important quantities to L-SET performance. (a) Two possible definitions of the electrometer gain; (b) Ratio of the Josephson inductance of SCPT to the "bare" Josephson inductance of a classical single junction, for two important gate DC values: $q_g = \pm 1$ (L_{J0}), and that giving the maximum gain.

most sensitive device. The rapidly growing L_J^* towards low E_J/E_C, as seen Figs. 5.6 (b) and 5.7, nevertheless, to some extent cancels the benefit of the growing gain.

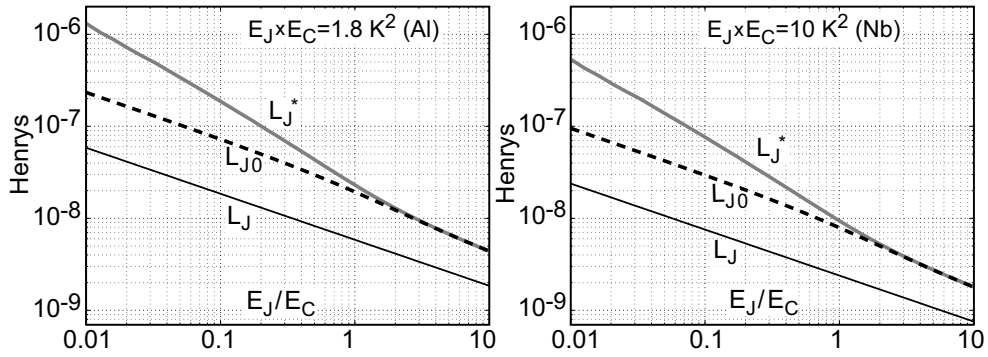

Figure 5.7: Numerical values of SCPT Josephson inductance L_{J0} and L_J^* for Al (left) and Nb (right). Also shown is the "bare" single junction value L_J.

The amplitude of the incoming wave $V_{\rm in}$ in Eq. (5.12) is related in a complicated manner to V_R, the voltage over the SCPT (see the discussion preceding Eq. 3.15):

$$V_R = V_{\rm in} \left| \frac{2\, Z_R}{Z + Z_0} \right| . \tag{5.15}$$

Here, Z is the impedance of the whole resonator, Eq. (5.7), and Z_R is the impedance of the parallel resonator only (without C_c). The voltage division,

Eq. (5.15), is illustrated in Fig. 5.8.

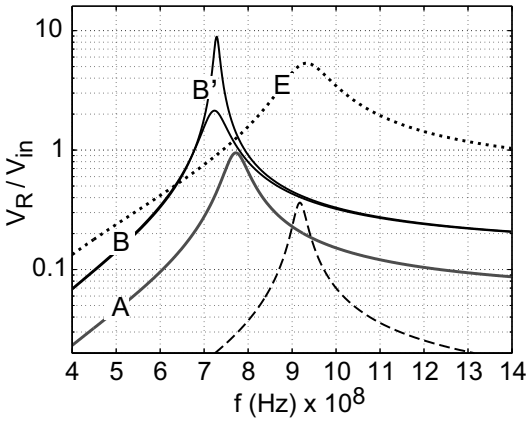

Figure 5.8: Voltage ratio in the L-SET circuit, Eq. (5.15), plotted for samples A, B and E. The curve labelled B' is for sample B in the high-drive "anharmonic" mode, with $Q_i \sim 200$. In addition, the dashed curve is for: $Q_i = 40$, $L = 100$ pH, $C = 300$ pF, $C_c = 2$ fF (see the beginning of Sec. 5.3.5).

5.3.2 Analytical calculation for critical coupling

Fortunately, analytical expression for the charge sensitivity in amplitude readout can be derived in an important limit. We assume critical coupling $Z = Z_0$ (in practice, a suitably chosen C_c). Though it is not obvious based on the following analysis, this also turns out to be the optimal tank circuit for any kind of SCPT. We will examine the stated optimality later on using numerical calculations.

Since we assumed critical coupling, half the power is dissipated in the resonator, and hence $R = Q_i/(\omega_p C) = R'$, and $Q_L = 1/2Q_i$. Using Eq. (5.9), we find

$$C_c = \sqrt{\frac{C}{\omega_p Q_i Z_0}}. \tag{5.16}$$

Similarly, $1/(\mathrm{i}\omega_p C_c) + Z_R = Z_0$, and thus $Z_R = Z_0 + \mathrm{i}/(\omega_p C_c)$. Equation (5.15) then becomes

$$V_R = V_{\mathrm{in}}\sqrt{1 + \frac{1}{\omega_p^2 C_c^2 Z_0^2}} \approx \frac{V_{\mathrm{in}}}{\omega_p C_c Z_0} = V_{\mathrm{in}}\sqrt{\frac{Q_i}{\omega_p Z_0 C}}. \tag{5.17}$$

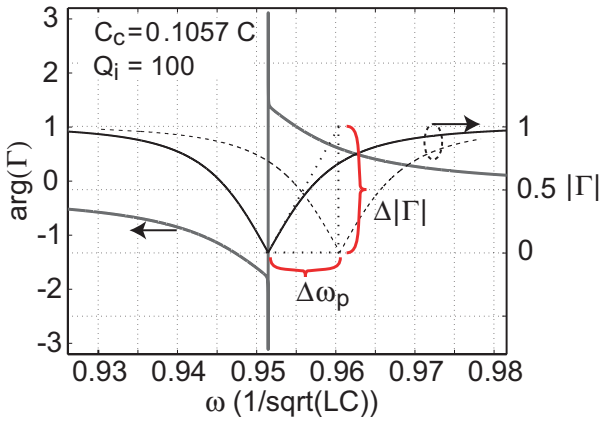

Figure 5.9: Illustration of "tuned-to-slope" operation of the L-SET in amplitude readout, $Z \simeq Z_0$. Gate charge affects the resonance frequency ω_p, which affects $|\Gamma|$. $\arg(\Gamma)$ is also plotted, with gray line.

Here, the second form holds for a reasonably large Q_i, and for the last form, we have substituted the condition for C_c from Eq. (5.16).

In the linear regime (harmonic mode), the best sensitivity is obviously at the largest possible value of the probing voltage $V_{\rm in}$ where linearity still holds reasonably well. This is the case when an AC current of critical peak value flows through the SCPT, and the phase swing is π peak-to-peak. Then, V_R in Eq. (5.17) equals the universal critical voltage of a Josephson junction, Eq. (3.7), $V_{CV} = \pi\hbar\omega_p/(4e)$, and we get

$$V_{\rm in} = \frac{\pi\hbar\omega_p^2 C_c Z_0}{4e} \simeq \frac{\pi\hbar\omega_p^{3/2}\sqrt{Z_0 C}}{4e\sqrt{Q_i}}, \tag{5.18}$$

which is a rather strong function of ω_p due to (1) decreasing voltage amplification, Eq. (5.17), and (2) increasing V_{CV}.

Also the three derivatives in Eq. (5.13) have to be evaluated at critical coupling. For the second derivative we easily find, using $\omega_p = (L_{\rm tot}C)^{-1/2}$,

$$\frac{\partial\omega_p}{\partial L_J^*} = \frac{1}{\sqrt{C}}\frac{1}{2(L_J^*)^2\sqrt{1/L + 1/L_J^*}}. \tag{5.19}$$

The first derivative $\partial|\Gamma|/\partial\omega_p$ in Eq. (5.13) means that the more change in Γ for a given change in ω_p, the better, as illustrated in Fig. 5.9. It improves with increasing quality factor, and weakens with increasing ω_p.

In the book of Kajfez [116], a formula has been derived for Γ close to resonance:

$$\Gamma \simeq \left[1 - \frac{1}{1 + \mathrm{i} Q_L 2 \frac{\omega - \omega_p}{\omega_0}} \right], \tag{5.20}$$

which reduces to $\Gamma \simeq \mathrm{i} Q_L 2(\omega - \omega_p)/\omega_0$ and yields

$$\partial|\Gamma|/\partial\omega_p = 2Q_L/\omega_0 \simeq Q_i/\omega_p. \tag{5.21}$$

Note that this results contradicts a "rule of thumb" that the FWHM of a resonance is frequency divided by the *loaded* quality factor. The basic rule does not hold because we are not dealing with the response directly. Equation (5.21) holds reasonably well also clearly off from critical coupling. For arbitrary coupling, the value of Q_L could also be easily evaluated using $Q_L^{-1} = \omega_p L_{\mathrm{tot}}/R + \omega_p L_{\mathrm{tot}}/R'$, and we find $Q_L = Q_i/(Q_i \omega_p^3 C_c^2 Z_0 L_{\mathrm{tot}} + 1)$.

Observe the discontinuous phase jump in Fig. 5.9 at $\omega = \omega_p$; the sharp feature is peculiar to critical coupling, but it does not give advantage for detection because the reflected signal is zero, or vanishingly small. Note also that the reflected signal being small does not matter for amplitude readout, because then only the *change* is important.

In the remaining expressions, L_J^* should be understood as its value at the optimum gate operation point. Through insertion of Eqs. (5.18), (5.19) and (5.21) into Eq. (5.12), C and Z_0 cancel, and we are left with a rather simple expression for the charge sensitivity in this particular case of amplitude readout and critical coupling:

$$s_q = \frac{8e(L_J^*)^2 \sqrt{\frac{1}{L} + \frac{1}{L_J^*}} \sqrt{2k_B T_N}}{g_m \pi \hbar L_{J0} \sqrt{\omega_p Q_i}} \quad \text{[CLASSICAL]} \tag{5.22}$$

in units of $[e/\sqrt{\mathrm{Hz}}]$. Clearly, it is best to omit the shunting inductor, i.e., $L \to \infty$ in the classical case. Also, the operation frequency should be high. If an alternate gain definition is used $\overline{g} \equiv \frac{\partial L_J^*}{\partial q_g} \frac{e}{L_J^*}$, a particularly simple formula can be derived for the ultimate sensitivity:

$$s_q = \frac{8e\sqrt{2k_B T_N L_J^*}}{\overline{g} \pi \hbar \sqrt{\omega_p Q_i}} \quad \text{[CLASSICAL]} \tag{5.23}$$

5.3.3 Quantum corrections to the sensitivity

An important issue still needs to be addressed. Equation (5.18) holds strictly in the limit of a classical oscillator. In our case, however, typically $\hbar\omega_p \sim k_B T$, and quantum effects may play a role. Energy due to vacuum fluctuations $E_Q = \frac{1}{2}\hbar\omega_p$ can be comparable to the energy required to drive the

L-SET oscillator into the nonlinear regime. This is equivalent to say that quantum phase fluctuations become of the order $\langle\pi\rangle$, or, that phase becomes more or less delocalized.

In terms of energy, the threshold energy of delocalization is of the order $\sim E_J^* = (\Phi_0/2\pi)^2(L_J^*)^{-1}$ which, as we emphasize, is significantly smaller at low E_J/E_C than the "bare" single junction E_J due to quantum suppression of Josephson tunneling. We get $E_J^* = \frac{1}{2}\hbar\omega_p$ if $L_J^* \sim 300$ nH and $\omega_p \sim 1$ GHz. Using Fig. 5.7, this high L_J^* is met at $E_J/E_C \sim 0.06$, or ~ 0.02, for an SCPT made out of Al or Nb, respectively. These fundamental limits were calculated for $L \gg L_J^*$.

Even before this "switching" into nonlinear regime happens, quantum noise has the effect of reducing the detector performance because less energy can be supplied in the form of drive, that is, $V_{\rm in}$ in Eq. (5.12) is lower. This can be calculated in a somewhat semiclassical manner as follows. Energy of the oscillator is due to the drive (E_D) and noise (we stay in the linear regime):

$$E = \frac{\Phi_O^2}{8\pi^2 L_{\rm tot}}\varphi^2 = E_D + E_Q = \frac{\Phi_O^2}{8\pi^2 L_{\rm tot}}(\varphi_D)^2 + \frac{1}{2}\hbar\omega_p \qquad (5.24)$$

where the phases are in RMS, φ is the total phase swing, and φ_D is that due to drive. Solving for the latter, we get

$$\varphi_D = \sqrt{\varphi^2 - \frac{4\pi^2\hbar\omega_p L_{\rm tot}}{\Phi_0^2}}. \qquad (5.25)$$

Now, Eq. (5.25) is to be evaluated when the total swing φ corresponds to critical drive. This was defined in Sec. 3 to take place at the "critical" amplitude $\sqrt{2}\varphi_C = \pi/2$. Critical voltage is simply proportional to φ_C: $V_{CV} \equiv \gamma\varphi_C$, where $\gamma = \hbar\omega_p/(2e)$ and $\gamma = 4\hbar\omega_p/(\pi^2 e)$, for voltage and current bias, respectively, from Eqs. (3.7) and (3.5). The critical voltage is then reduced by the factor

$$\beta \equiv \frac{V_{D,C}}{V_{CV}} = \frac{\varphi_{D,C}}{\varphi_C} = \frac{\sqrt{2}\sqrt{\varphi_C^2 - 4\pi^2\hbar\omega_p L_{\rm tot}}/\Phi_0^2}{\varphi_C} = \sqrt{1 - \frac{32\hbar\omega_p L_{\rm tot}}{\Phi_0^2}}. \qquad (5.26)$$

Note that $V_{D,C} \to 0$ at large $L_{\rm tot}$ or at large ω_p. $L_{\rm tot}$ becomes large at low E_J/E_C. We thus expect there to be an optimum with respect to both ω_p and E_J/E_C.

We now proceed identically as when arriving at Eq. (5.22), but substitute $V_{\rm in}$ in Eq. (5.18) by $\beta V_{\rm in}$. The fully correct form of Eq. (5.22) taking into account zero-point fluctuations is finally

$$s_q = \frac{8e(L_J^*)^2\sqrt{\frac{1}{L}+\frac{1}{L_J^*}}\sqrt{2k_BT_N}}{\beta g_m \pi\hbar L_{J0}\sqrt{\omega_p Q_i}}, \tag{5.27}$$

where β is from Eq. (5.26). This expression should be used when evaluating the ultimate performance of L-SET. The classical result, Eq. (5.22), is valid when the occupation number of the oscillator $\gg 1$. Equation (5.27) is, unfortunately, quite complicated. Only one tendency is evident: charge sensitivity improves as the inverse square root of Q_i. The best E_J/E_C is not easy to determine. Considering Fig. 5.6, we see the following. The gain g_m in the denominator grows like $(E_J/E_C)^{-1}$. However, L_J^* in several places in Eq. 5.27 grows as well (as $\sim (E_J/E_C)^{-0.4}$), but L_{J0} does not change a lot.

Nonetheless, by differentiation with respect to ω_p and L, we find that the absolute minimum of Eq. (5.27) occurs when the following relation holds:

$$\omega_p = \frac{\Phi_0^2(L_J^*+L)}{64\hbar L_J^* L} \tag{5.28}$$

This minimum value turns out to be independent of L:

$$s_q^{QL} = \frac{64\sqrt{2}e(L_J^*)^2\sqrt{2k_BT_N}}{g\pi\sqrt{\hbar}\Phi_0 L_{J0}\sqrt{Q_i}}. \tag{5.29}$$

In other words, whatever shunting L we choose, we achieve the ultimate charge sensitivity s_q^{QL} when operating at the frequency given by Eq. (5.28).

It is also evident that L_J^* should be small. At a given E_J/E_C, this happens if E_JE_C is high. However, one should stay below $E_C < \Delta$ to avoid quasiparticle poisoning [117,118]. In practice, this limitation prohibits $E_J/E_C \lesssim 0.2$ in the case of a good Al SCPT. Sample E, see Table 2.2, came in fact very close to this limit. By using materials with high Δ, nevertheless, the quasiparticle threshold is substantially relieved and even lower E_J/E_C can be usable.

5.3.4 Optimization of charge sensitivity

Next we display quantities which are numerically optimized from the original Eq. (5.12) without any assumptions regarding the coupling strength. To illustrate the effect of the operation frequency, we plot a number of characteristic curves, each at different ω_p, in Fig. 5.10.

We see that the optimal charge sensitivity is reached around $E_J/E_C \simeq 0.2...0.3$, almost independent of drive frequency, and only weakly depending on Δ. At smaller E_J/E_C, operation frequency (Fig. 5.11) matters a bit more. The caustic of the curves in Fig. 5.10 is the ultimate limit of Eq. (5.29) (the small difference is due to numerics).

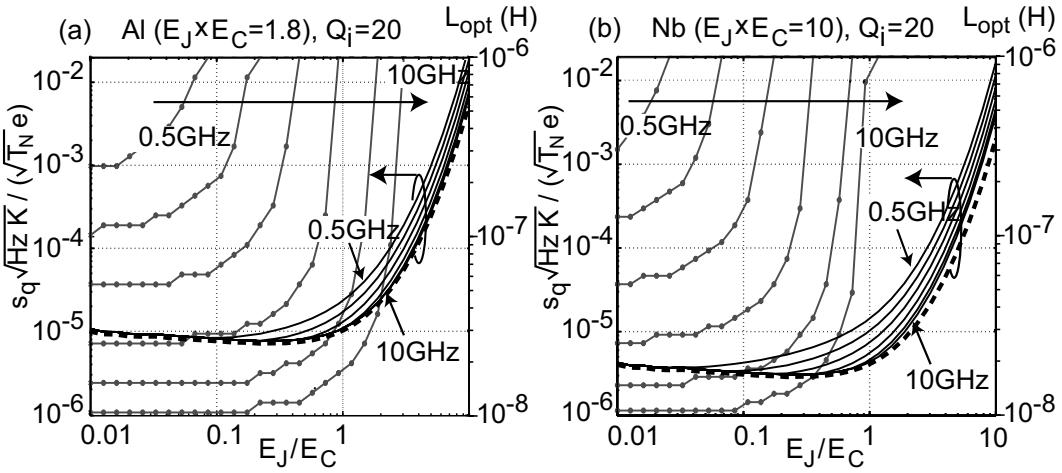

Figure 5.10: Numerically optimized (from Eq. (5.12)) charge sensitivity for L-SET, at the following operation frequencies (from top to bottom): $f_p/(1\text{GHz}) = 0.5; 1; 2; 4; 7; 10$. (a) Aluminium device; (b) Niobium device. Also shown is the optimal shunting inductor L in each case. The fundamental limit, Eq. (5.29), is indicated with dotted lines.

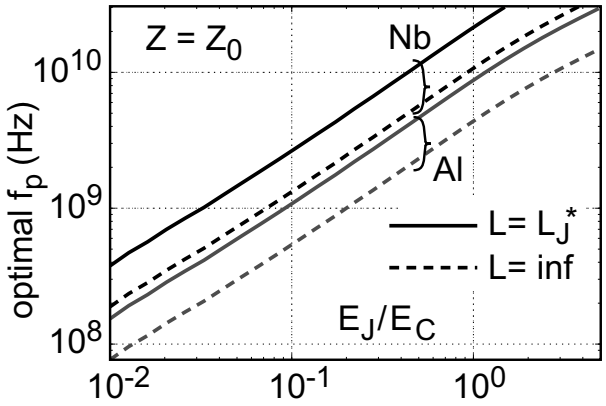

Figure 5.11: Optimal operation frequency of the L-SET from the point of view of charge sensitivity, c.f. Eq. (5.28).

As discussed in [P10], Eq. (5.27), with $L = \infty$, predicts the optimal sensitivity correctly down to the quantum regime.

By direct numerical calculations we find that the minimum is reached always at critical coupling, $Z = Z_0$. In an wide number of numerical evaluations, we have found no exceptions to this tendency. A similar conclusion holds also for the RF-SET [119] and hence it seems rather universal.

We conclude that with present Q_i of ~ 20, $s_q \sim 10^{-5} e/\sqrt{\text{Hz}}$ is reachable

with an Al SCPT and a system noise of 3 K (almost independent of the operation frequency). Using Nb [120–122] and a realistic 1 K [123] would yield $s_q \sim 3 \times 10^{-6} e/\sqrt{\text{Hz}}$. By increasing Q_i to ~ 1000 and using a SQUID amplifier [124] which have the best demonstrated $T_N \lesssim 200$ mK [125, 126], the sensitivity would improve to the level of $s_q \sim 10^{-7} e/\sqrt{\text{Hz}}$, which figure of merit is better than that of any other electrometer considered. We note that in the present experiment, see Sec. 5.5, $Q_i \sim 20$ likely due to the effect of external noise.

5.3.5 Discussion on sensitivity

A relevant question is whether the detector performance would improve, and how much, by choosing a different L. It would be particularly interesting to operate with a very small L when doing reactive readout of the charge-phase qubit (see Sec. 5.4), because of the more efficient shunting of phase fluctuations. We note that although the power levels are substantially higher when $L \ll L_J^*$ (the voltage ratio V_R/V_{in}, Eq. 5.15, becomes < 1, see the dashed curve in Fig. 5.8), sensitivity decreases because the modulation of L_{tot} becomes vanishingly small.

Referring to Fig. 3 in [P10] , which displays the sensitivity as a function of detuning L and C_c off from the optimum, we see that close to optimal values, the dependence is weak. Continuing the figure down to $L = 100$ pH, we calculate as good as $s_q \sim 6 \times 10^{-4} e/\sqrt{\text{Hz}}$, for the same C_c and Q_i. Thereby, we expect promising prospects for operating also with a strong inductive shunting.

As stated above, the best detector performance is at critical coupling. One might naively think of further reducing, maybe significantly, the power dissipation in the resonator itself (at the expense of perhaps a bit reduced sensitivity), by heavily overcritical coupling. Then, $|\Gamma| \sim 1$ but phase changes by 2π, and it is feasible if $C_c \sim C$. The procedure does not help, nonetheless. Simply, in-resonator power dissipation $P_{D,C} = V_{CV}^2/(2R)$ does not depend on the coupling. Moreover, since the best detector performance is at critical coupling, $P_{D,C}$ would only increase at a given sensitivity.

All the above analysis was performed without phase bias, that is, at $\langle\varphi\rangle = 0$. As seen in Fig. 5.4 (b), the inductance modulation can be a lot stronger with a phase bias. However, it is questionable whether this gives a real advantage for detection, because the maximum tolerable drive strength is reduced as well.

Thus far, operations were supposed to take place at the gate DC value which maximizes the transfer function, i.e., yields $g = g_m$. To be accurate, the optimum sensitivity is *not* at this point, but typically some % towards the

degeneracy, $q_g = \pm 1$. This is because a lowering L_J^* offers a slight advantage over a reducing g_m. However, the difference is only a few %, and can be neglected in practice.

By numerical investigations we found that readout of $\arg(\Gamma)$ offers within numerical accuracy the same optimized figures of merit as the discussed readout of $|\Gamma|$.

5.4 Quantum measurement

The L-SET configuration could potentially be used for several fundamentally different operations or measurements in the quantum limit. This section contains plausible ideas that are still at the level of speculation because experimental verification is lacking.

5.4.1 Nondestructive readout of the charge-phase qubit

For some years, the control of quantum states of mesoscopic superconducting junctions has been a subject of intensive research. These "superconducting qubits" may offer a controllable approach to implement a real quantum information processing. The first suggestions in this field are due to Bouchiat [72] and Shnirman *et al.* [127] in 1997. Since then, various qubits based either on the charge or phase degree of freedom have been proposed [128–134], and implemented [59, 135–140]. So far, two coupled superconducting qubits (or equivalent) have been successfully operated [141–144].

The L-SET setup might qualify as an integrated qubit plus a detector, much in a similar fashion as suggested by Zorin [145] in a different readout scheme. It has become clear that the measurement of qubits must be done avoiding quasiparticle generation [146, 147]. The L-SET "internal qubit" would naturally be read by measuring inductance which depends on whether the SCPT (qubit) is in the lowest band (qubit state $|0\rangle$), or in the first excited band (qubit state $|1\rangle$). This design would implement a highly non-invasive readout of the charge-phase qubit [135], since the physical structure is basically the same, although in the L-SET the shunting L is typically larger. In fact, the property of low back-action, as discussed below, could make the scheme come close to a QND (Quantum Non-Demolition) measurement [148–151].

For example, if $E_J/E_C \sim 1$ and at the degeneracy point $\varphi = 0$, $q_g = \pm 1$, then according to Fig. 5.12, the qubit state $|1\rangle$ would correspond to an inductance ~ -35 nH, while the state $|0\rangle$ has ~ 20 nH (Fig. 5.4). By choosing L suitably, the total inductance $L_{\rm tot}$ would then be either very small,

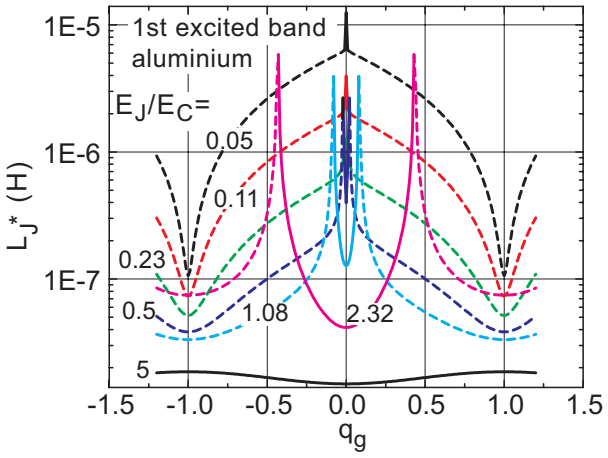

Figure 5.12: Josephson inductance in the 1st excited band at $\varphi = 0$ of a typical SCPT made of Al. Negative values are marked by dashed lines.

or $\sim 2L$, depending on the qubit state. This would result in a huge difference in f_p, or, in practice, a high sensitivity in a CW reflection measurement.

The discrimination (or measurement) time needed to pick up enough information to distinguish $|0\rangle$ from $|1\rangle$ is

$$T_m = \frac{s_V^2}{(\Delta V_{\rm out})^2} = \frac{2k_B T_N Z_0}{V_{\rm in}^2 |\Delta\Gamma|^2}. \tag{5.30}$$

Using $V_{\rm in} \sim 1\,\mu$V, and $|\Delta\Gamma| \sim 1$ (see the experimental data, Fig. 5.16 (a), where the two absorption dips due to positive and negative inductance, corresponding to the two lowest bands, show up clearly), we get $T_m \sim 3$ ns. Hence the measurement time is rather limited by the oscillator response time ($\gtrsim 10$ ns).

To calculate the SNR achievable in this design, we will estimate the relaxation time $(\Gamma_R)^{-1}$ of the state $|0\rangle$ or $|1\rangle$ into a thermal mixture state, when the measurement is on. Both the qubit operations and the measurement are supposed to be performed at $q_g = \pm 1$ and $\langle\varphi\rangle = 0$ (notice that the measurement involves a sinusoidal drive in the phase direction).

Dephasing and relaxation are determined by the fluctuations in direction and magnitude of the effective "magnetic field" $2E_J \cos(\varphi/2)\vec{x} + 4E_C(1-q_g)\vec{z}$ formed by the two control parameters, φ and q_g. The angle between the field and the z-axis is denoted by Θ; $\sin(\Theta) \equiv 2E_J \cos(\varphi/2)/(\hbar\omega_{01})$, where $\hbar\omega_{01} = E_1 - E_0$. Thus, $\Theta = \pi/2$ at the degeneracy point, and $\Theta \to 0$ at $q_g = 0$. If q_g is tuned by an amount Δq_g off from the degeneracy, using Eq. (4.15) we find $\cos(\Theta) = 2\Delta q_q E_C/(E_J \cos(\varphi/2))$ if $E_J/E_C \ll 1$.

By reducing coupling to the charge control line, the effects of fluctuations

in the gate lead can be made negligible. However, for the fluctuations of φ, the case is not so. The relaxation rate is then determined by the spectrum of voltage fluctuations at the level-spacing frequency ω_{01} [152–154]; $\Gamma_R \propto s_V'^2(+\omega_{01})$. Here, $s_V'^2$ is the unsymmetrized power spectral density,

$$s_V'^2 = \hbar\omega \mathrm{Re}(Z_S)\left[\coth\left(\frac{\hbar\omega}{2k_BT}\right)+1\right] \tag{5.31}$$

where $Z_S = (1/(\mathrm{i}\omega L_{\mathrm{tot}}) + \mathrm{i}\omega C + 1/R + 1/(Z_0 + 1/(\mathrm{i}\omega C_c)))^{-1}$ is the impedance seen by the SCPT between its source and drain (Fig. 5.13). In Ref. [155], it is evaluated that

$$\begin{aligned}\Gamma_R \simeq & \frac{4\pi E_J^2}{\hbar^2\omega_{01}}\frac{\mathrm{Re}(\mathrm{Z_S}(\omega_{01}))}{R_K}\times \\ & \times\left\{\cos^2(\Theta)\left[\sin^2\left(\frac{\varphi}{2}\right)+d^2\cos^2\left(\frac{\varphi}{2}\right)\right]+\frac{4d^2E_J^2}{\hbar^2\omega_{01}^2}\right\}\end{aligned} \tag{5.32}$$

At the degeneracy point, Eq. (5.32) reduces to

$$\Gamma_R \simeq \frac{2\pi d^2 E_J}{\hbar}\frac{\mathrm{Re}(\mathrm{Z_S}(\omega_{01}))}{R_K}. \tag{5.33}$$

Eq. (5.33) means that a symmetric ($d = 0$) SCPT is decoupled from fluctuations due the environment (in the first order) at this point.

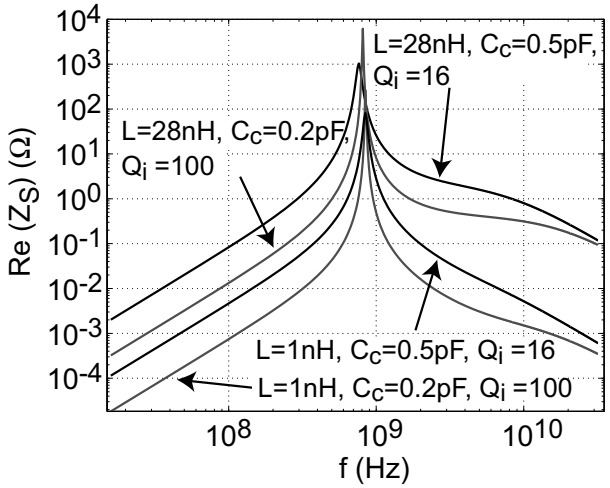

Figure 5.13: Real part of the impedance Z_S seen by SCPT in L-SET circuit. All the curves are computed using the values $f_p = 850$ MHz, $L_J^* = 45$ nH.

Now, the measurement involves a sinusoidally varying φ. At the degeneracy point $\Theta = \pi/2$, the term in front of square brackets in Eq. 5.32 is zero, and the relaxation rate would again be given by Eq. 5.33. In practice, however, q_g cannot be tuned arbitrarily accurately to the degeneracy, but it remains offset by an amount Δq_g. Then, the effect of φ varying from $\varphi = 0$ due to the measurement becomes the most important source of relaxation. Eq. 5.32 yields

$$\Gamma_R \simeq \frac{2\pi E_J}{\hbar} \frac{\mathrm{Re}(\mathrm{Z_S}(\omega_{01}))}{R_K} \left(\frac{2E_C}{E_J} \Delta q_g \right)^2 \left\langle \tan^2(\varphi/2) \right\rangle . \tag{5.34}$$

Here, we have neglected terms containing d^2. Performing a simple average between $\varphi = -\pi/2 ... \pi/2$ we find

$$\Gamma_R \simeq \frac{1.7 E_J}{\hbar} \frac{\mathrm{Re}(\mathrm{Z_S}(\omega_{01}))}{R_K} \left(\frac{2E_C}{E_J} \Delta q_g \right)^2 . \tag{5.35}$$

To estimate numbers in a real situation, let us take $d = 0.1$, $E_J/E_C = 0.5$ and $E_J = 1$ K. From Fig. 5.13 we see $\mathrm{Re}(\mathrm{Z_S}) \sim 0.1\,\Omega$ at the level spacing frequency $f_{01} \sim 10 - 50$ GHz. Using Eq. (5.35) we find $\Gamma_R \gtrsim 10\,\mu$s. Even in a real situation, relaxation due to the external circuit and the measurement is thus negligible, and an amplitude SNR of $\sim 10^3$ in qubit measurement is possible.

To gain further confidence that the relaxation caused by the measurement is negligible, we note that the measurement drive has no effect on the high-frequency spectrum - it just contributes a narrow peak at f_p. We also note that the mixing of power to the higher harmonics is only tens of % at the optimal drive level, as discussed in [P10]. Especially, since $\omega_{01} \gg \omega_p$, the drive should not contribute to the high-frequency spectrum. This is in a striking contrast to the sequential tunneling SET, where a white spectrum of shot noise results.

The presented readout method would be particularly important for a qubit having a strong inductive shunt which offers more immunity to phase noise [156]. If $L = 100$ pH, we computed that in Eq. (5.30), $|\Delta\Gamma| \sim 0.1$, and $V_{\mathrm{in}} \sim 10\,\mu$V, and hence the measurement time is comparable to that discussed previously. Therefore, the readout would also work even with an almost mesoscopic loop size.

5.4.2 Back-action in charge measurements

Let us now discuss an issue conceptually very different from the internal qubit, that of measuring charge on the gate capacitor. This operation mode

of the detector has been discussed in detail in this thesis. So far, however, we have only treated the "output" noise. This treatment is valid only in the limit where the SCPT gate is driven with a voltage source of zero internal impedance, that is, a classical source. In this case, potential fluctuations of the SCPT island, the back-action, will not affect the measurement accuracy [89].

For practical purposes, however, the source is a mesoscopic object having a clearly finite source impedance. Then, the back-action from the L-SET will affect accuracy of the measurement, and the back-action will also potentially disturb the system by inducing relaxation.

Let us denote the island charge by Q_I, island voltage by V_I, and their amplitude spectral densities by s_{QI} and s_{VI}, respectively. The back-action charge noise, the "input" noise, is due to fluctuations of the island potential [106, 157]. We define the input energy sensitivity:

$$\epsilon_I = \frac{s_{QI}}{2C_\Sigma} = \frac{1}{2} C_\Sigma \, s_{VI}^2. \tag{5.36}$$

Next, one should calculate s_{VI}. Definitely, fluctuations on the SCPT island are due to voltage fluctuations s_V across the SCPT. The question is, how s_V causes s_{VI}, in particular, when the measurement is on (sinusoidal phase swing). The issue is quite involved. Here s_{VI} *is not one half* of s_V as one might naively assume, but one must think in terms of the SCPT band structure:

$$V_I = \frac{dE}{dq_g}. \tag{5.37}$$

Now, fluctuations of φ couple to V_I so that dE/dq_g depends in general on φ. Only at $\varphi = 0$, there is no dependence. Therefore, if φ fluctuates, so does $dE/dq_g = V_I$. s_V is computed in the L-SET circuit according to the fluctuation-dissipation theorem [158], with the symmetrized power spectrum ($\omega > 0$):

$$s_V^2 = 2\hbar\omega \mathrm{Re}(Z_S) \coth\left(\frac{\hbar\omega}{2k_B T}\right) \tag{5.38}$$

Using s_V, the amplitude spectral density s_φ is obtained as $s_\varphi = \frac{2e}{\hbar\omega} s_V$. Examples of the spectra are shown in Fig. 5.14.

The frequencies relevant to back-action are those at which the signal is read, namely low frequencies $\ll f_p$. Nonlinear dependence of dE/dq_g on φ (see Fig. 5.15) mixes the spectrum, centered around f_p, partially into the low frequencies. We now make the following *rough, worst case estimate*

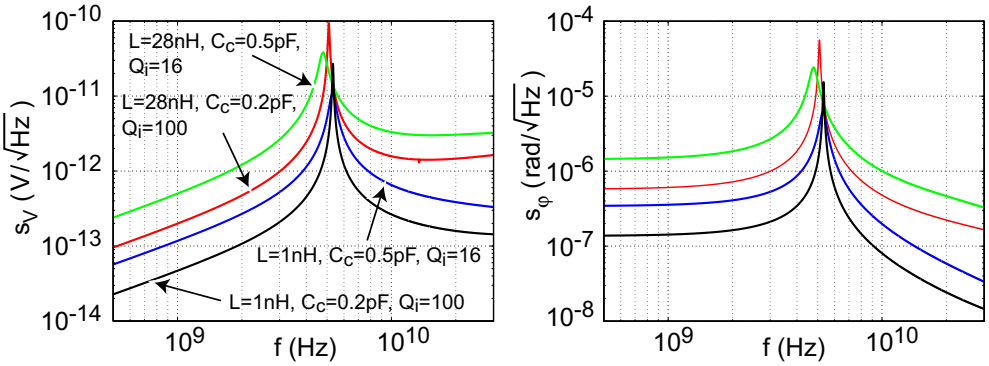

Figure 5.14: Calculated spectra of voltage fluctuations across the SCPT in the L-SET setup (left), and the corresponding curves for phase fluctuations (right).

of the low-frequency back-action by estimating it with the noise around f_p. Using Fig. 5.15, we observe that in a linear approximation, if φ has an RMS fluctuation $\langle\varphi\rangle \sim 0.5$ rad which is a typical quantum-limited value, then $V_I = dE/dq_g$ fluctuates between about $-1.50\,E_C/e ... -1.45\,E_C/e$, at $E_J/E_C = 0.17$. Denoting the peak-to-peak fluctuation of V_I, $\sim 0.05\,E_C/e$, by $k\,E_C/e$, we thus have

$$s_{VI} \sim \frac{kE_C}{e} s_\varphi = \frac{2kE_C}{\hbar\omega} s_V. \tag{5.39}$$

and

$$s_{QI} = C_\Sigma S_{VI} = \frac{2C_\Sigma kE_C}{\hbar\omega} s_V \;\Rightarrow\; \epsilon_I = \frac{2C_\Sigma (kE_C)^2}{(\hbar\omega)^2} s_V^2 \tag{5.40}$$

Inserting $C_\Sigma = 1$ fF, $E_C = 1$ K, $s_\varphi = 5\times10^{-5}$ rad$/\sqrt{\text{Hz}}$ (Fig. 5.14), we obtain $s_{VI} \sim 0.2$ nV$/\sqrt{\text{Hz}}$. This number is an order of magnitude lower than the typical figures for a sequential tunneling SET [159, 160], where wide-band shot noise dominates the spectrum. The low back-action of the L-SET is important for several research applications.

From Eq. (5.40) we find the input energy sensitivity $\epsilon_I \sim 0.2\,\hbar$. The full energy sensitivity is given by (neglecting correlation between ϵ_O and ϵ_I) by [161]

$$\epsilon = \sqrt{\epsilon_O \epsilon_I}, \tag{5.41}$$

where the uncoupled energy sensitivity is $\epsilon_O = s_q^2/(2C_\Sigma)$. From Fig. 5.10 we get for an Al SCPT $s_q/\sqrt{T_N} \simeq 8\times10^{-6} e/\sqrt{\text{K Hz}}$, and thus $\epsilon_O \sim 8\,T_N\hbar/\text{K}$. Finally, $\epsilon \sim 0.6\,\hbar$ at $T_N = 0.2$ K. According to the rough estimate, thereby,

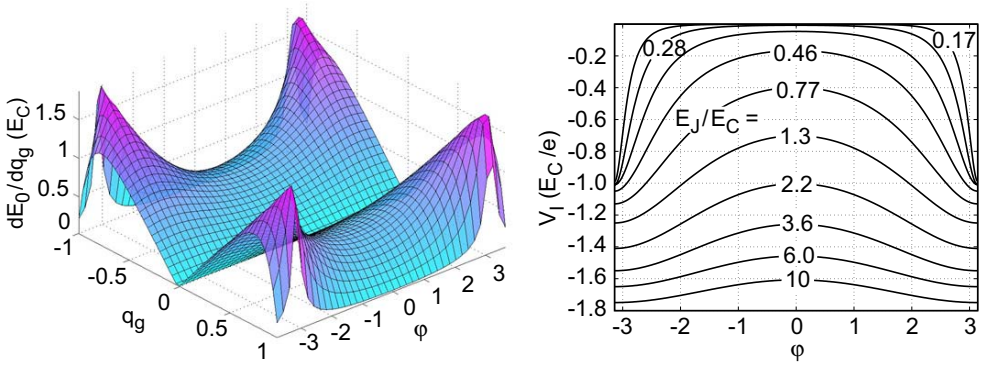

Figure 5.15: Island voltage of a SCPT, dE/dq_g, for $E_J/E_C = 1$ (left), and its phase dependence at the optimal q_g for different E_J/E_C.

the L-SET comes close the Heisenberg limit $\epsilon = \frac{1}{2}\hbar$ for phase-insensitive linear amplifiers [161–164] (this restriction does not hold, however, in the parametric mode of the L-SET, see Sec. 5.6).

Notice also how the uncertainty principle is "forced" upon in the scheme: one can substantially improve ϵ_O by increasing Q_i, but this decreases ϵ_I because $\mathrm{Re}(Z_S)$ simultaneously increases.

A detailed analysis which takes properly into account the frequency dependence of the island spectrum, as well as the operator properties of the island quantities [160, 165], would be worth the effort.

5.5 Experimental results and analysis

In this section we review experimental data measured in the L-SET configuration. We show data mostly from our two best samples, B and E. Some data from sample A has been displayed in [P7] and [P8]. All the measured and functioning samples, and a summary of their measurements, are listed in Table 2.2 (Sec. 2.2).

In all the shown L-SET responses, including those displayed in publications, a background ripple of a couple of dB has been subtracted for clarity. The ripple was due to reactance of the LC filters and circulators. The background was constructed from either low-power or high-power response, or in some cases, combined from them.

The responses have also been normalized by making the reasonable assumption that considerably off the resonance, $|\Gamma| = 1$. Note that it is difficult to obtain this information directly from the experiment. Rare points where it seems that $|\Gamma| > 1$ are due to failures in the normalization.

While starting the L-SET experiments, it was difficult to make the plasma resonance match the quite narrow frequency window $\sim 600 - 900$ MHz set mostly by the circulators. The problem was circumvented by installing the shunting inductor, because the tank resonance could then be seen all the way during cooldown. Indeed, we often experienced contact problems which caused the signal to disappear, and it saved a lot of wasted time to recognize this at an early stage.

5.5.1 The need for noise isolation

Let us first briefly emphasize the need for an isolator (or circulator, backwards isolation S_{12}) between the sample and the amplifier chain. Part of the back-action noise of the 1st stage amplifier is dissipated in the sample:

$$P_D = S_{12} k_B T_N \int \mathrm{d}\omega \left(1 - |\Gamma(\omega)|^2\right). \tag{5.42}$$

The integrand is peaked around ω_p. P_D should be much less than the dissipated power that makes the junction switch:

$$P_{D,C} = \left(\frac{V_{CV}}{\sqrt{2}}\right)^2 \frac{1}{R} = \frac{\pi^2 \hbar^2 \omega_p}{32 e^2 Q_i L_{\mathrm{tot}}}. \tag{5.43}$$

Note that this quantity differs from the critical power P_C. $P_{D,C}$ is the power dissipated in sample when it is probed with P_C. In the case of critical coupling, $P_C = 2\,P_{D,C}$. Otherwise, P_C needs to be computed using Eq. (5.15).

Without isolator, i.e., $S_{12} = 1$, we get $P_D/P_{D,C} \sim 1.2$ and ~ 10 for samples B and E, respectively, which are clearly unacceptable values. With $S_{12} = -15$ dB (a modest number for a single device), these numbers are 0.03 and 0.5. The latter is not OK (therefore, we installed a second circulator in series when measuring sample E).

5.5.2 Gate modulation of the Josephson plasma resonance

Sample E had quite a low $E_J/E_C \sim 0.3$. Therefore, the Coulomb effect is strong, and we expect a 300 % modulation of the Josephson inductance, and a strong gate dependence of the system resonant frequency f_p. The resonance is visible in the reflection measurement as the well-known absorbtion dip around f_p. Indeed, the resonance moves as much as 115 MHz as seen clearly in Figs. 5.16, 5.17 which show the experimental data. The values of f_p (Fig. 5.18 (a)), inferred from the measured position of the resonance dip, also

reasonably fulfill the theoretical expectation of the gate modulation pattern calculated from Eq. (5.10).

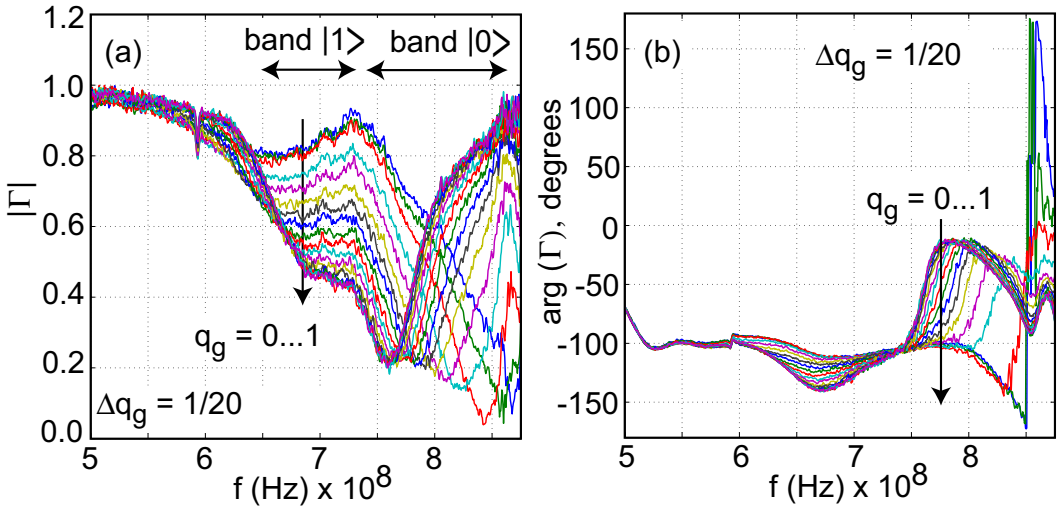

Figure 5.16: Measured response of sample E at different gate charges spaced by $\Delta q_g = 1/20$, linear regime (-125 dBm); (a) amplitude $|\Gamma|$; (b) phase $\arg(\Gamma)$. In (a), the absorption dips due to the two lowest energy bands of the SCPT are marked. Note how the system goes through critical coupling around 850 MHz (the coupling changes because L_J^* changes).

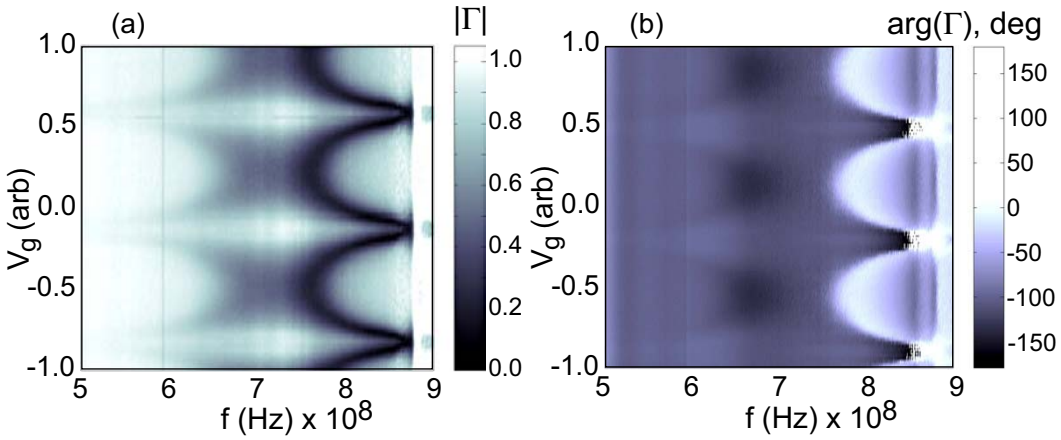

Figure 5.17: Data of Fig. 5.16 plotted as isosurfaces (sample E).

An interesting feature in Figs. 5.16 and 5.17 is a second, weaker resonance dip at a frequency *smaller* than f_0. The second resonance also moves with q_g, and forms almost a mirror image of the main plasma resonance w.r.t.

the location of f_0. The second resonance must correspond to a *negative inductance*, which, as seen in Fig. 5.12, is a characteristic property of the 1st excited band of the SCPT. A calculation of f_p for the two lowest bands is plotted in Fig. 5.18 (b). By comparing to experiment (Fig. 5.17), the reader can verify that the second resonance is due to the excited band.

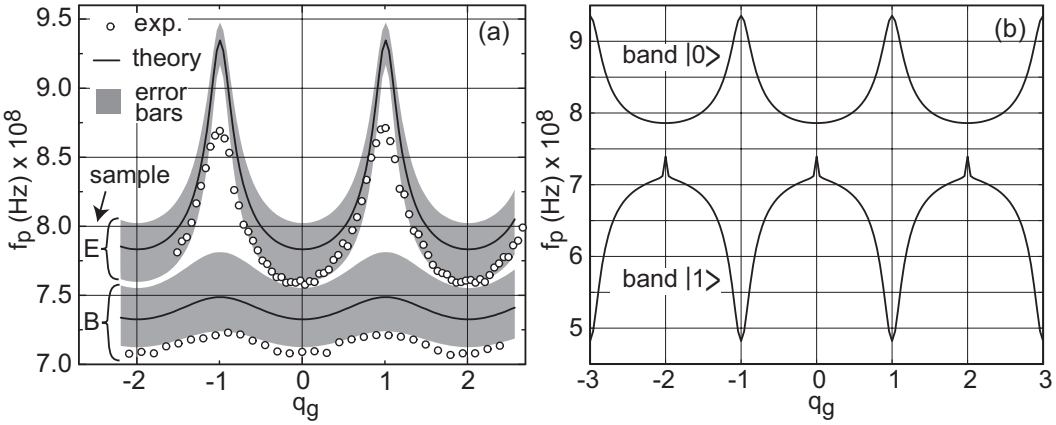

Figure 5.18: (a) Gate modulation of the L-SET resonant frequency for samples E and B. Theoretical predictions are plotted with full lines, and estimated error margins with gray. For discussion, see text. (b) predicted f_p for sample E, for the two lowest energy levels of the SCPT.

Influence of external noise

Some questions concerning the data can still remain. The measured values of L_J^* are regularly some $20-30$ % larger than expected. This is seen in Fig. 5.18 (a) where the values of f_p are detectably low within the error bars, and in Table 2.2. One may also wonder why the SCPT is in an excited state for a significant part of time quite uniformly for all gate values, although no high-frequency pumping had been applied. The latter cannot solely be due to Zener tunneling, which was found in Sec. 4.4 to be insignificant except at the degeneracy points.

Third, we see that in all the samples, Q_i has been not more than ~ 20. This corresponds to about $10\,\Omega$ in series with the SCPT [166]. Because Q_i increases strongly in most samples at higher drive when the SCPT current channel becomes effectively blocked (see [P6]), we are assured that the dissipation is residing within the SCPT. Notice that the SCPT tunnel resistance $2\,R_T \sim 10-20\,\mathrm{k}\Omega$ does not shunt the resonator, because the BCS gap acts as an exponential barrier for quasiparticle tunneling at voltages and frequencies $\ll \Delta$.

We interpret that the mentioned non-idealities are due to external noise whose source is not clear. Noise around f_p would increase L_J^* due to non-linearity. At a much higher frequency, noise would cause excitation and relaxation, and hence also dissipation which would reduce Q_i.

5.5.3 Detector performance

Charge sensitivity of the L-SET was measured by applying to the gate a small sinusoidal signal of frequency f_m and magnitude $\Delta q_{\mathrm{RMS}} \sim 0.01\,e$, and measuring the height of the amplitude-modulated sidebands such as those in Fig. 5.19 (a) by spectrum analyzer over a resolution bandwidth $B = 1$ kHz. The (amplitude) signal-to-noise ratio SNR was determined as the ratio of the sideband height to the noise floor. The RMS charge sensitivity is then given by

$$s_q = \frac{\Delta q_{\mathrm{RMS}}}{\mathrm{SNR}\sqrt{B}} \tag{5.44}$$

(neglecting that in fact there is also phase modulation which complicates the analysis).

Input bandwidth of the L-SET is expected to be $\sim f_p/Q_L$. For the harmonic (anharmonic) mode, this amounts to ~ 80 MHz (~ 100 MHz) for sample E, based on Q_L deduced from the measured frequency response. We made a direct measurement, Fig. 5.19 (b), where we stepped f_m. In the harmonic mode, we got about one half (40 MHz) of the expectation, after which the response rapidly weakens 20 dB/decade. In the anharmonic mode, the band does not end sharply, but a very usable $s_q \sim 10^{-4}\,e/\sqrt{\mathrm{Hz}}$ is reached at 100 MHz. In both modes, the detector gives some signal even at 300 MHz.

In fact, the charge sensitivities in Fig. 5.19 (b) were not directly measured, only the height of the side bands. We then made a reasonable approximation by scaling these values according to a separately measured sensitivity.

The best charge sensitivities for each of the samples were listed earlier, in Table 2.2. The numbers were limited by a white noise whose level agreed with the supposed amplifier noise. The measured values are typically somewhat weaker than predicted. For samples C and D, the difference is large, and is clearly attributable to quasiparticle poisoning (see further discussion in Sec. 5.7).

However, samples B and E come to within a factor of ~ 2 from the prediction. The rest is easily explained as being due to noise: the maximum slope of gate modulation for sample E (Fig. 5.18 (a)), for example, is one half of the expected, likely due to the unwanted excitation. Also, because the maximum energy one can supply to the oscillator is limited, less energy

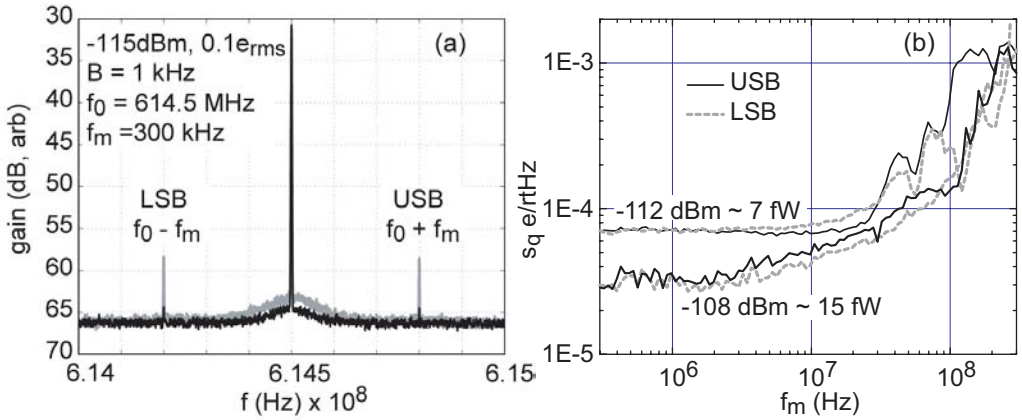

Figure 5.19: (a) Sample B: typical spectrum measured when gate DC was tuned to $g \simeq g_m$ (gray), and $g \sim 0$ (black); (b) Sample E: Illustration of the measured L-SET charge sensitivity as a function of input signal frequency. For discussion, see text.

can be supplied in the form of drive if low-frequency noise energy is present, similarly as in Eq. (5.24). This also agrees with the measured critical voltage being clearly less than expected (see Sec. 3.2) for most of the samples.

The $1/f$ properties of the L-SET were quite similar to previous single-electron devices [167–169]); $1/f$ noise extended up to a few hundred kHz. For sample B, however, interesting and highly complex $1/f$ properties (Fig. 5.20) were seen at nonlinear drive. The data were measured using mixer phase detection (amplitude readout gave qualitatively similar results). We also used a gate marker signal of $\sim 0.15\, e_{\rm RMS}$, at $f_m = 300$ kHz, and stepped the gate DC. Notice how $1/f$ behaves non-monotonically with respect to drive strength. Sometimes the noise source is residing at the detector output and sometimes at the input. This is seen in that in some graphs, the noise level does not depend on gain (height of the marker). In the last graph (-97 dBm), noise (the bump around 30 kHz) occurs solely in the output.

We argue that the peculiar $1/f$ features are due to chaotic Josephson dynamics [170–172]. Although it is clear that this type of noise would be highly detrimental for applications of the "anharmonic" mode, such effects were not seen in (the best) sample E. The nonlinear dynamics apparently depend sensitively on the E_J^*/E_L ratio.

5.5.4 The regime of anharmonic oscillations

Next we display data measured at higher drive amplitudes, in the "anharmonic" operation mode of the L-SET. As seen in Figs. 5.21, 5.22 and 5.23,

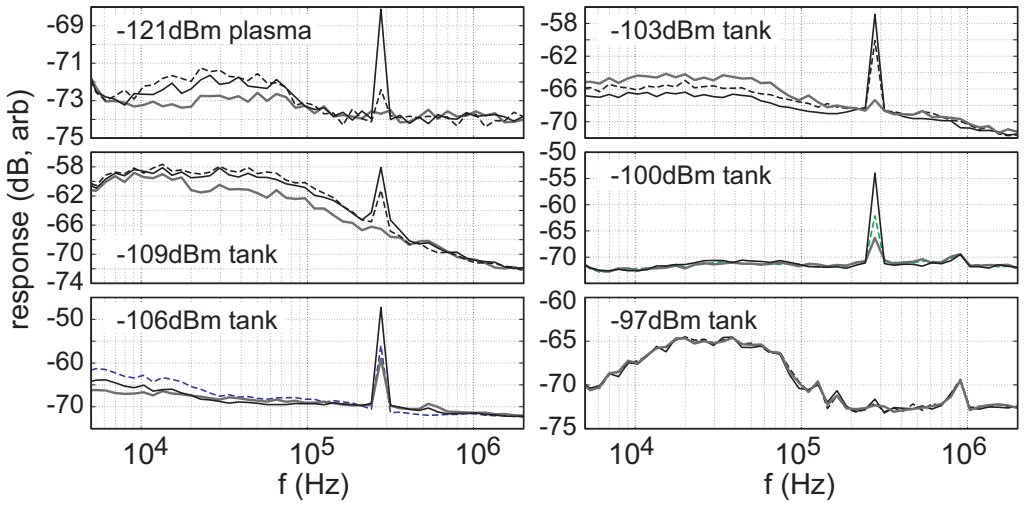

Figure 5.20: Sample B: measured $1/f$ noise spectra for different drive strengths. Upper left graph (marked plasma) is measured at $f_p = 715$ MHz, with a linear drive. Other graphs are at $f_0 = 614$ MHz, with a high (non-linear) drive. Black lines: maximum gain; dashed lines: intermediate gain; gray lines: minimum gain.

significant gate modulation persists much beyond the end of the linear regime which is roughly at the critical power $P_C \simeq -116$ dBm or -112 dBm, for samples B and E. Gate modulation was observed clearly up to a drive that corresponds to a peak-to-peak swing of $50 \times 2\pi$.

As seen in the experimental data, mainly what depends on gate is the coupling strength (depth of the resonance dip). At high Q_i, coupling is quite sensitive to Q_i, Eq. (5.17). Therefore, changes in dissipation in the SCPT affect Q_i which affects coupling. To account for a 20 % change in coupling as in the data at the last row of Fig. 5.23, for example, Q_i should change between about 120 and 90.

In contrast to the RF-SET, the anharmonic mode is hence not *directly* based on the control of dissipation, but rather, it relies on inducing a large change in coupling via a small change in dissipation. We also stress that the voltages are still in the μV range, and hence no quasiparticles are created. Also the power levels are extremely small: for sample E, the best $s_q = 3 \times 10^{-5} e/\sqrt{\text{Hz}}$ was measured at -110 dBm $= 10$ fW, which is far from the typically pW range of an RF-SET yielding a similar performance.

Preliminary attempts were made to explain the dependence of the high-drive response on L_J^*. Two explanations were tested. First, the effect could be due to interband transitions and relaxations, quite similar to operation of the BOT (Sec. 4.3.2): The relaxation rate caused by quantum fluctuations in the

environment depends sensitively on q_g, Eq. (5.32). Another process is then needed for excitation. This could be the Zener tunneling, the probability of which becomes reasonably large at a high drive. This model fits qualitatively some features in data, like the "double-dip" structure around $q_g = \pm 1$ at the last row of Fig. 5.22. However, the relaxation rate required to explain the dissipation and its changes seems large.

A second possibility is that the dynamics could be similar to the (hysteretic) RF-SQUID [39, 90, 173]. For hysteresis to appear, it is required that the hysteresis parameter $\beta_L = 2\pi(LI_C^*/\Phi_0) > 1$. In our samples β_L varies as a function of q_g between 0.5...1.0 and 0.2...1.3 for samples B and E, respectively, However, it is not fully clear if even the largest values are > 1 (considering error margins). More work is clearly needed to properly explain the "anharmonic mode".

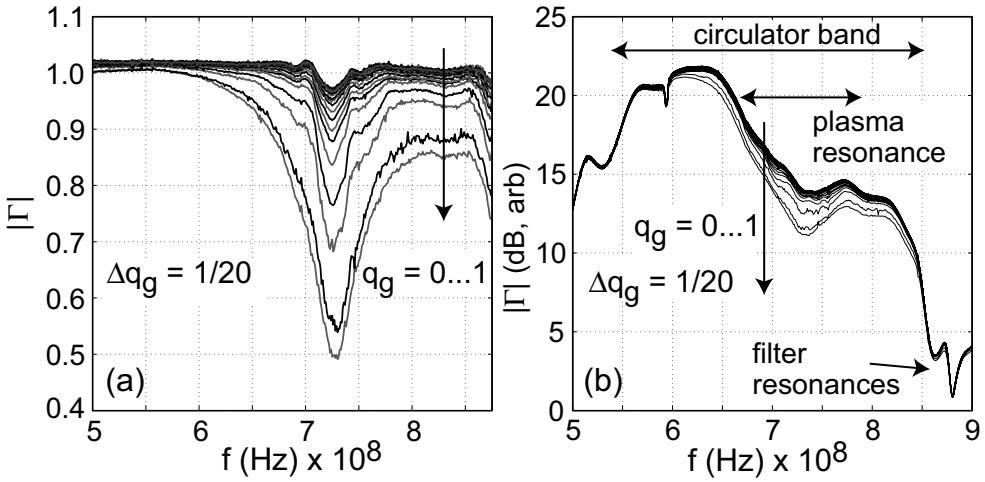

Figure 5.21: Frequency response of sample E at a high drive. (a) -106 dBm; (b) -101 dBm (original data, as it looks when measured in network analyzer).

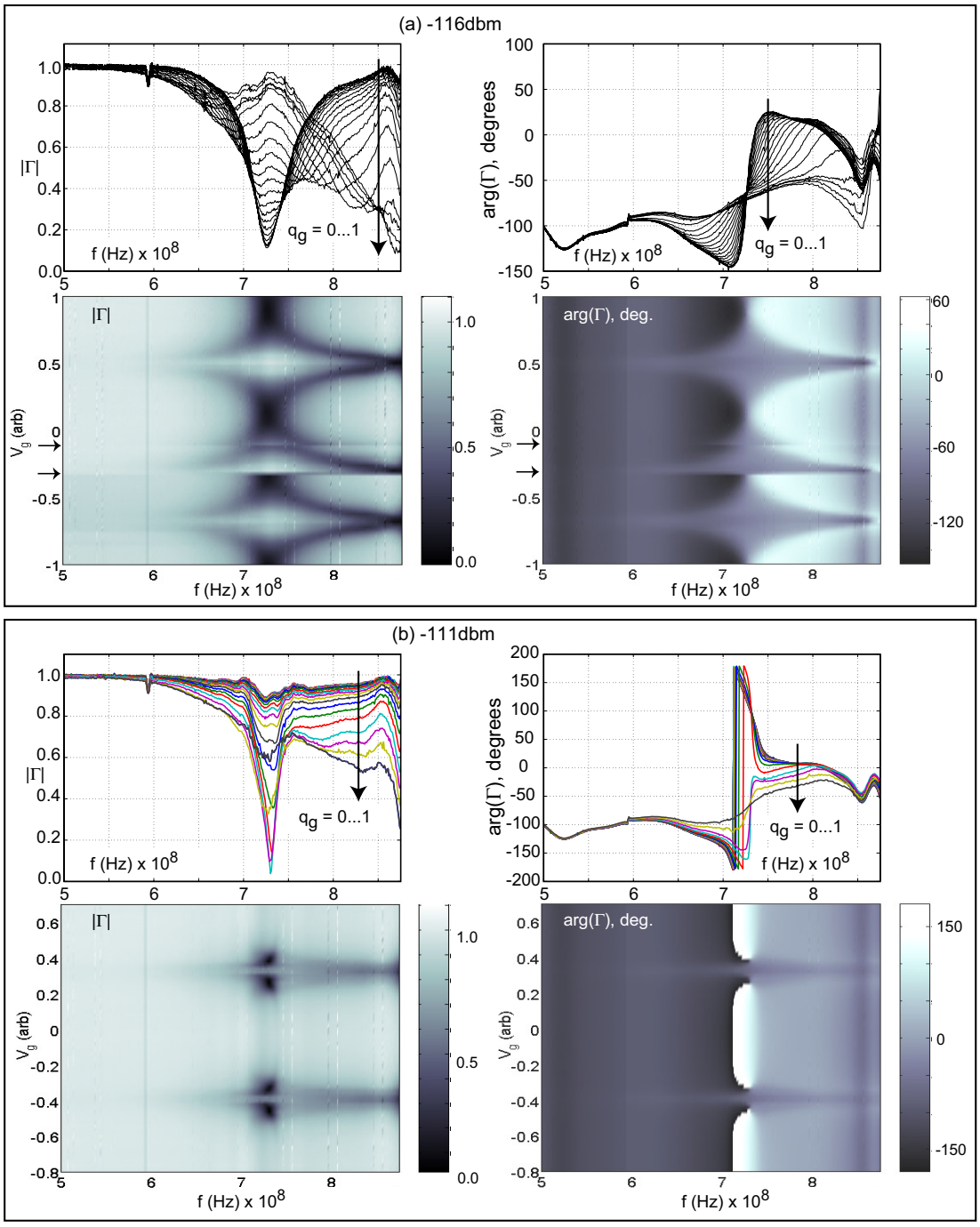

Figure 5.22: Frequency response of sample E as a function of increasing drive strength. Critical power for min L_J^* was about -112 dBm, between graphs of (a) and (b). The short arrows denote jumps of background charge. $\Delta q_g = 1/20$.

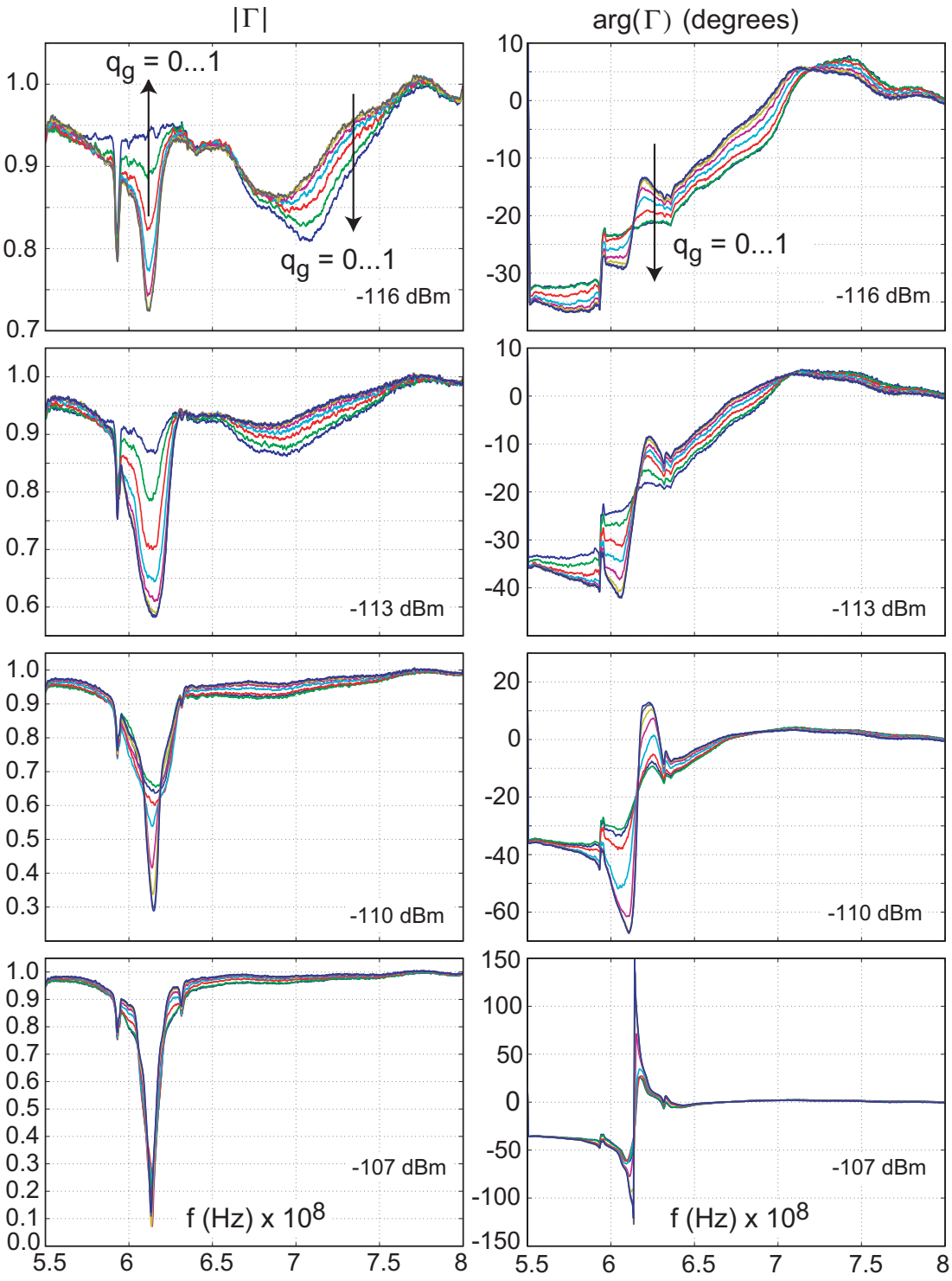

Figure 5.23: Frequency response of sample B as a function of increasing drive strength. $\Delta q_g = 0.15$. The arrows in the upper graphs indicate growing q_g (the tendency is the same in all graphs). Notice different scales.

5.6 Phase-sensitive detection

A parametric amplifier is a system which converts energy from a "pump" frequency to a different signal frequency [174–176]. A means of storing energy is required, which in electrical applications is a capacitor or an inductor. The conversion of power between frequencies can either be created through nonlinearity (intermodulation), or by parametric excitation which phenomenon takes place in children's swing for example.

In general, parametric amplifiers are a phase-sensitive amplifiers, that is, they amplify more one quadrature of an input signal than the other. In the quantum regime, this property has been used to demonstrate the squeezing of quantum noise by a Josephson junction parametric amplifier based on a classical junction [177, 178].

Josephson parametric amplifiers based on intermodulation gain have been studied quite extensively since the late 1960's [178–183]. However, to our knowledge, no experimental demonstrations whatsoever of a Josephson parametric device based on *parametric excitation* have been presented. Here we show how a mesoscopic analog of the Inductive Kinetic Amplifier (IKA) [184] [1], based on pumping of the effective Josephson energy of a JJ, can be implemented in the same scheme as the L-SET.

The original IKA proposal employs flux modulation of $E_J(\Phi)$ of SQUID junctions, however, here we achieve the same effect by gate modulation of $E_J^*(q_g)$ in the L-SET. Taking the modulation be $E_J^*(q_g) = E_{J0}^* - \Delta E_J^* \cos(\pi q_g)$, we get from the classical equation of motion of the L-SET, Eq. (1) in [P7], a linearized equation

$$C\frac{\hbar}{2e}\ddot{\varphi} + \frac{\hbar}{2eR}\dot{\varphi} + \frac{\Phi_0}{2\pi L_{\rm tot}}\varphi + \frac{2\pi}{\Phi_0}\Delta E_J^* \cos(\pi q_g)\varphi = I_{ext}, \tag{5.45}$$

where $q_g = \Delta q_g \cos(\omega_m t)$, I_{ext} is the carrier excitation, and the modulation amplitude $\Delta q_g > 1$. Eq. 5.45 can be cast in the form of Mathieu equation which describes a parametric amplifier, similar to Ref. [184].

The schematics is shown in Fig. 5.24. Via the gate of the SCPT, we modulate L_J^* at a frequency of $\omega_0/2$ and with a high amplitude $\sim 5 - 10\, e$. The system is probed by a reflection measurement quite similar to the L-SET. The reflected carrier signal at roughly the tank circuit frequency ω_0 is detected by a mixer. In order to see the dependence on the phase of the carrier wave, we modulate the local oscillator (LO) phase $\Delta\theta$ before detection. As a final stage of the experiment, we also applied a low-frequency (f_m) signal to the gate.

[1] We propose the name MIKA (Mesoscopic IKA) for the new concept.

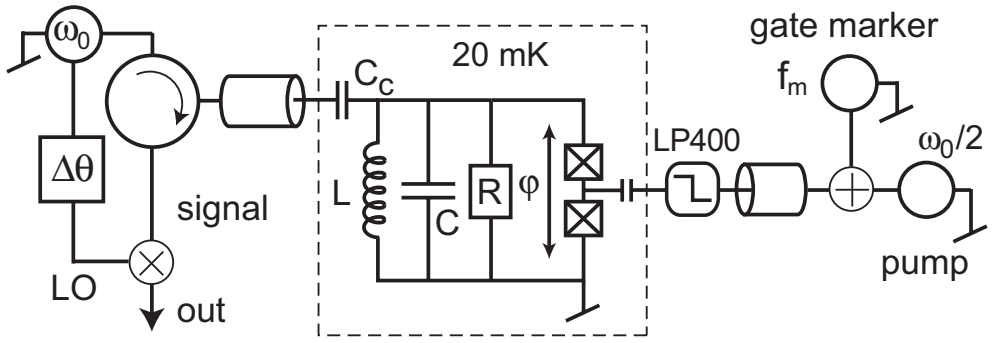

Figure 5.24: Setup when L-SET is used as a parametric amplifier. The effective Josephson energy of the SCPT is pumped via gate at half the resonant frequency $\omega_0/2$.

We first characterized the setup as a reflection amplifier to the carrier at $\sim \omega_0$. At very low carrier amplitudes, parametrically generated reflection gains as high as 15 dB were observed. As seen in the left panels of Fig. 5.25, the gain depended on the DC value of q_g. The right panels of Fig. 5.25 display the reflection gain at a fixed $\omega_0/(2\pi) = 614.3$ MHz as a function of the LO phase. We observe substantial amplification as well as deamplification.

We carried out several test to verify the authenticity of the observations. A simple explanation that the parametric gain would simply be due to cross-coupling from the gate to bias the SCPT, thus in fact making the device to work as an ordinary Josephson parametric amplifier and not as an IKA, was ruled out by repeating the $\omega_0/2$ pumping at the input side, via the coupling capacitor. No parametric excitation was observed this way. However, some cross-coupling is inevitable, and it can make the approximation $\sin(\varphi) \simeq \varphi$ used to arrive at Eq. 5.45 not fully sound.

To test that the observed phase dependence is not solely due to the 2nd harmonic generated through intermodulation of the gate pump signal, we repeated the measurement with only the gate pump applied. In this case, no phase dependence was seen.

To go further, we measured the phase dependence of a small-amplitude gate marker signal at $f_m = 30$ kHz. The detection was now performed from the amplitude-modulated carrier at the frequency $f_0 \pm f_m$. We observed phase dependence also of this gate marker signal, see Fig. 5.26. However, the charge sensitivities were not improved. This is understandable since the charge sensitivity is limited by the maximum amount of energy in the oscillator, scale of which is set simply by E_J^*. Pumping cannot increase this value.

We also demonstrated squeezing of noise at the frequency of the reflected

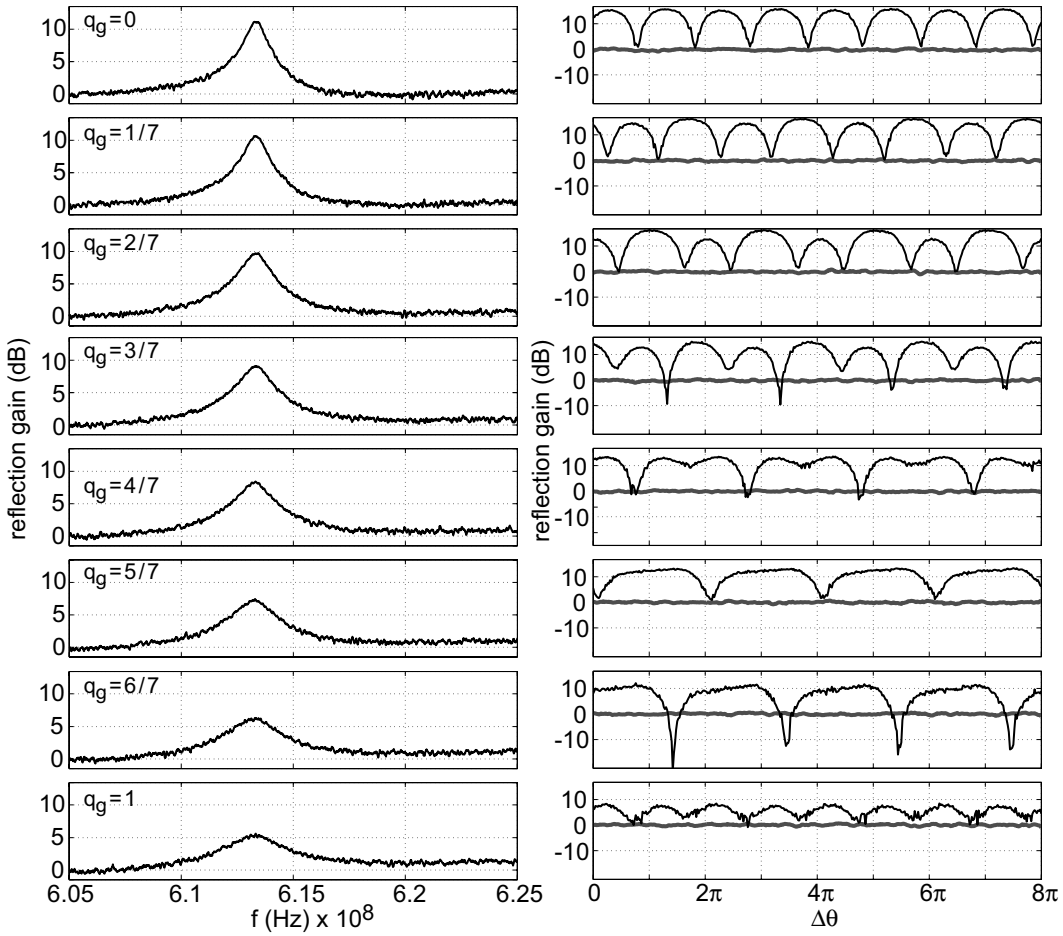

Figure 5.25: Sample B: Measured parametric gain in the L-SET setup, with an $\omega_0/2$ pump applied to the gate. Carrier power = -130 dBm. Each row is with certain q_g. Left column: frequency response in the active region for parametric excitation, around $\omega_0/(2\pi) = 614.3$ MHz. Right column: corresponding phase-sensitive gain at ω_0 as a function of the LO phase $\Delta\theta$, with pump (black) and without pump (gray).

carrier, ω_0. As discovered in Sec. 5.5.3, the noise is fully dominated by a low-frequency noise which is mixed to ω_0, i.e., by the $1/f$ background charge noise. In Fig. 5.26 (b) we show the sine and cosine quadrature components of the measured noise at three different values q_g. We thus see that even 400 % squeezing of $1/f$ noise is possible. Though this squeezing is only that of classical noise, i.e., its amount is far more than that limited by the uncertainty principle, it can provide a route to reduce the effect of $1/f$ noise by putting the noise into one quadrature only.

As a summary of this section, we have demonstrated for the first time

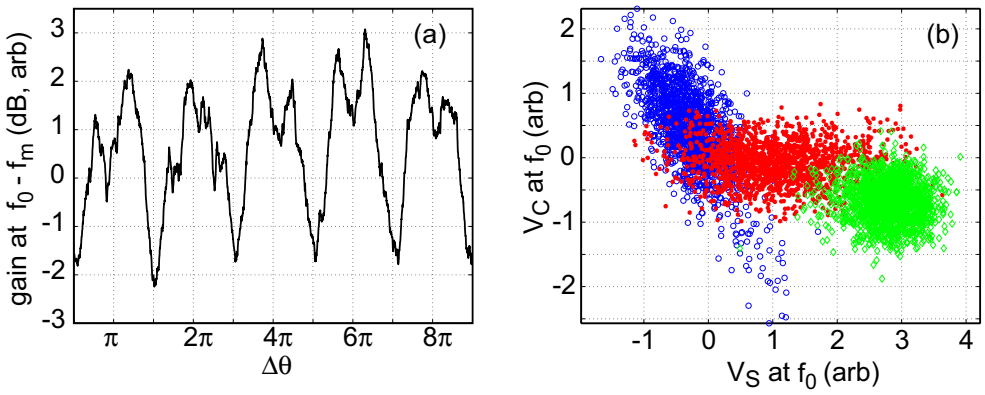

Figure 5.26: Sample B: (a) Gate signal amplitude measured as a function of the LO phase $\Delta\theta$. (b) squeezing of $1/f$ noise at the drive frequency ω_0, for three values of q_g.

parametric amplification in a truly mesoscopic device. The experiment also constitutes the first observation of parametric effects in a charge measurement. Moreover, we have demonstrated squeezing of $1/f$ charge noise. The findings are likely to have impact on future exotic quantum measurements in the solid state.

5.7 Quasiparticle poisoning

It has been known since the first experiments on the Cooper-pair transistor [185] that its gate periodicity changes sensitively from $2e$ to e due to disturbances in the form of, for example, temperature or external noise [69,117,186–188]. If the period is $2e$, all the single-electron excitations (quasiparticles) on the island are paired, whereas the e case corresponds to the presence of a single unpaired electron on the island, and hence to an energy higher by Δ.

In thermal equilibrium it holds that below temperatures $T \sim 300$ mK in a typical sample, there are no unpaired electrons if $E_C < \Delta$ [69]. This is because, as seen in Fig. 5.27 (a), the "quasiparticle band" is the amount Δ higher than the lowest band. In our L-SET experiment, samples B and E fell below this limit (E only marginally in fact), and, indeed, they were purely $2e$. The periodicity was tested by raising temperature. Sample D was e, which we attribute to external noise since the LP1000 filter in Fig. 2.6 was lacking.

The following discussion is based on the experimental data from sample C. Here, $E_C > \Delta$, but the period should, nevertheless, be partially $2e$. In

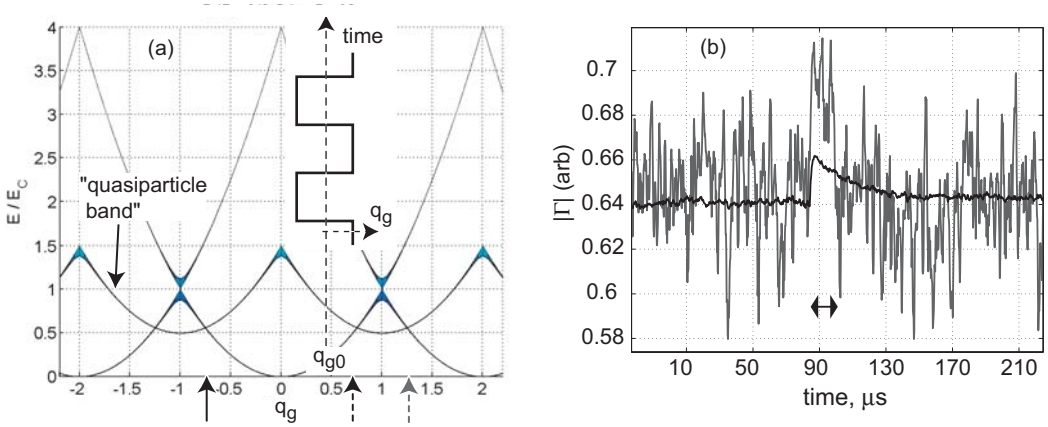

Figure 5.27: (a) The scheme of pulsed measurements used for real-time monitoring of quasiparticle poisoning (see text), the lowest arrows refer to Fig. 5.30. The bands are as for sample C ($E_C/\Delta \sim 2$); (b) Sample C: an individual quasiparticle tunneling event (between the arrows) detected in real-time in the L-SET, and an ensemble average showing the exponentially decaying envelope.

the experiment, however, only e was seen if we swept V_g slowly. By faster sweeping of V_g we managed to turn the gate response noticeably towards $2e$ (Fig. 5.28) at sweep rates of already $\sim$ 10 kHz (per gate period). This indicates the timescale of significant quasiparticle poisoning is as low as in the sub-millisecond range.

The dynamics of the quasiparticle poisoning was studied in more detail by direct measurements of the quasiparticle tunneling rate as a function of q_g. Via a coaxial cable, we applied to the gate a 100 Hz square-wave voltage about the gate point q_{g0}, see the inset of Fig. 5.27 (a). The square wave signal had a fast rise time of about 100 ns, and hence the system will follow non-adiabatically the present energy band until a quasiparticle tunneling, slower than the rise time, makes it to relax.

Employing this configuration in the experiment, we undoubtedly saw individual events of single-electron tunneling (see see Fig. 5.27 (b)). An average over an ensemble of $\sim 10^5$ events for each q_{g0} was then measured in order to determine the statistics of the tunneling process as a function of the gate point. Examples of data obtained this way are shown in Fig. 5.29 (a). The fit to an decaying exponential is faultless as seen in Fig. 5.29 (b). To our knowledge, this is the first time the simple picture of tunneling in a mesoscopic junction has been verified accurately in a direct measurement. Single-electron events, such as that in Fig. 5.27 (b), however, have been observed in time-domain several times previously [189–191].

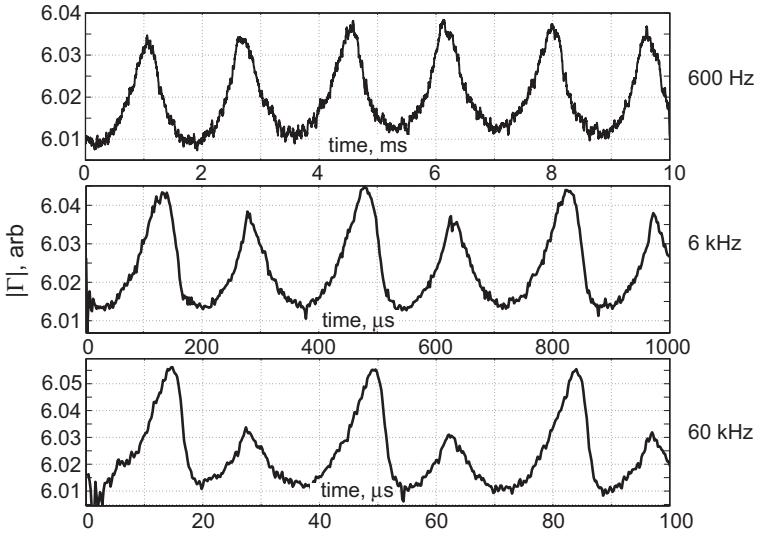

Figure 5.28: Sample C: response measured at $f_0 = 645$ MHz, versus V_g, for increasing frequency of a triangular V_g-sweep. Notice how the period doubles when the frequency increases.

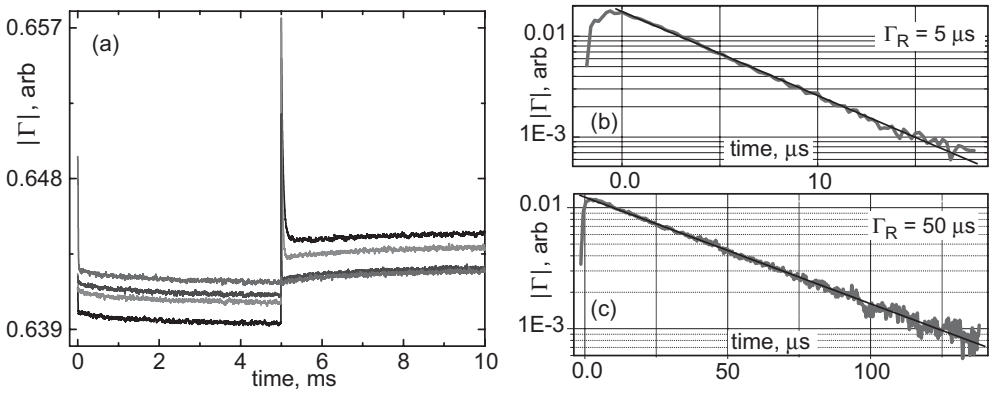

Figure 5.29: Sample C: (a) averaged response to a square pulse sequence applied to the gate in the configuration of Fig. 5.27 (a), for q_{g0} spaced by $0.025\,e$. (b), (c) Details of the data after the step at $5\,\mu$s, with fitted exponential decays, with q_{g0} spaced by $0.05\,e$.

Finally, in Fig. 5.30 we display the directly measured relaxation time Γ_R as a function of gate. It is important to be careful as to how read the graphs. The value of q_{g0} as indicated by the x-axes is the average, and the $1e$ peak-to-peak square modulation happens about it, see Fig. 5.27 (a). The sharp increases of quasiparticle tunneling rates are identified with the degeneracies between the quasiparticle band and the lowest band, as indicated by the

arrows in Figs. 5.30 and 5.27 (a). The small discrepancy can be due to inaccuracy in the determination of E_C/Δ.

Interesting features are also the two different time constants in some of the curves of Fig. 5.29 (a). These are also marked in Fig. 5.30, as twin data points. We interpret that these are due to competition between relaxation and excitation between the lowest band and the quasiparticle band.

The value of background charge was established by measuring a gate sweep as in Fig. 5.28 and identifying the largest peaks with $q_g = \pm 1$. A possible drift was excluded since a similar calibration measurement at the last stage gave the same result.

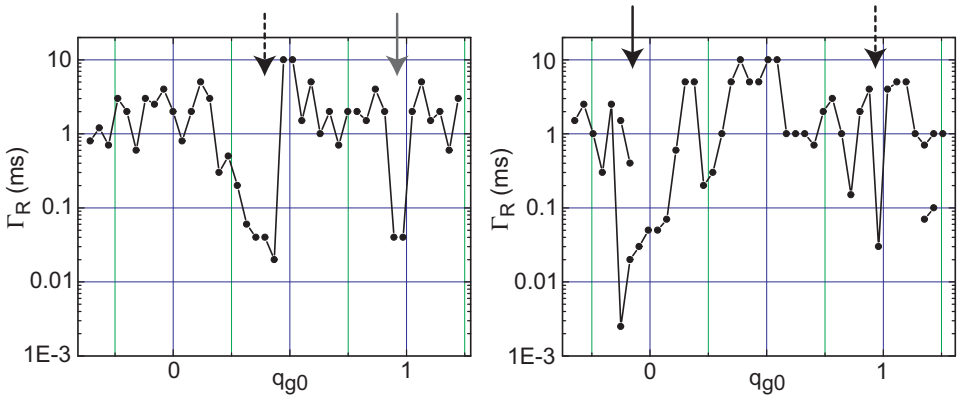

Figure 5.30: Sample C: Quasiparticle relaxation times extracted from the data measured in the configuration of Fig. 5.27 (a). The square pulse had a peak-to-peak amplitude of $1e$. (a) rising edge of pulse (towards positive q_g); (b) lowering edge of pulse (towards negative q_g).

Chapter 6

Quantum capacitance

IN the L-SET setup (Sec. 5) we have experimentally demonstrated driven oscillations of the phase in an SCPT. Since the band structure of an SCPT is actually a function of two external variables, the phase φ and the gate charge q_g, a natural question arises on the possibility of driven oscillations in the direction orthogonal to phase, namely along q_g-axis. In general, one might also consider an arbitrary oscillatory pattern of motion involving both directions [192–194].

If the voltage has to be increased by an amount dV in order to bring a charge dQ into a system, the differential capacitance is

$$C = \frac{dQ}{dV}. \tag{6.1}$$

If the electrostatic potential were originally V, the work so done is $dE = VdQ$, which immediately yields an important relation

$$V = \frac{dE}{dQ} \tag{6.2}$$

for a general dependence of energy E on charge Q. Differentiating Eq. (6.2) with respect to Q and combining with Eq. (6.1) we find

$$\frac{d^2E}{dQ^2} = \frac{1}{C} \tag{6.3}$$

which means that the effective differential capacitance is the inverse second derivative of energy with respect to charge.

The band energies of an SCPT depend on the (gate) charge, and an SCPT is thus predicted to behave like a capacitance with respect to changes of the gate charge. In order to calculate this effective capacitance C_{eff}, we have to be careful in what is meant by gate charge. In Eq. (6.3), Q is a real charge on

a capacitor. In the case of an SCPT, the commonly used parameter q_g *is not* a real charge, but just an acronym for $q_g = C_g V_g/e$. The real charge on the gate capacitor is $Q_g = C_g(V_g - V_I)$, where $V_I = \partial E_0/\partial q_g = 1/C_g(\partial E_0/\partial V_g)$ is the island voltage.

Using Eq. (6.1) with $V = V_g$ and $Q = Q_g$, we obtain:

$$\begin{aligned} C_{\text{eff}} &= \frac{\partial}{\partial V_g}\left(C_g V_g - C_g V_I\right) = C_g - C_g\frac{\partial V_I}{\partial V_g} = C_g - \frac{\partial^2 E}{\partial V_g^2} \\ &= C_g - C_g^2\frac{\partial^2 E_0}{e^2 \partial q_g^2} = C_g - \frac{C_g^2}{C_Q}, \end{aligned} \tag{6.4}$$

where we have defined a "quantum capacitance" $C_Q^{-1} = \partial^2 E_0/(e^2\partial q_g^2)$ due to the SCPT band structure directly. In contrast to inductance, this quantity is not directly observable. In order to see this, one must look into an SCPT from the gate, and then one observes the C_{eff} in Eq. (6.4). It is the input capacitance of an SCPT (and also of the single Cooper-pair box, see also Ref. [195]). We also note that the observable capacitance is *inversely* proportional to the "quantum capacitance".

In the following, we will plot quantities related to the quantum capacitance and its phase dependence. We typically use both dimensionless units for the general results, and compute numerical examples using typical values in SI units as an aid for the quantum engineer.

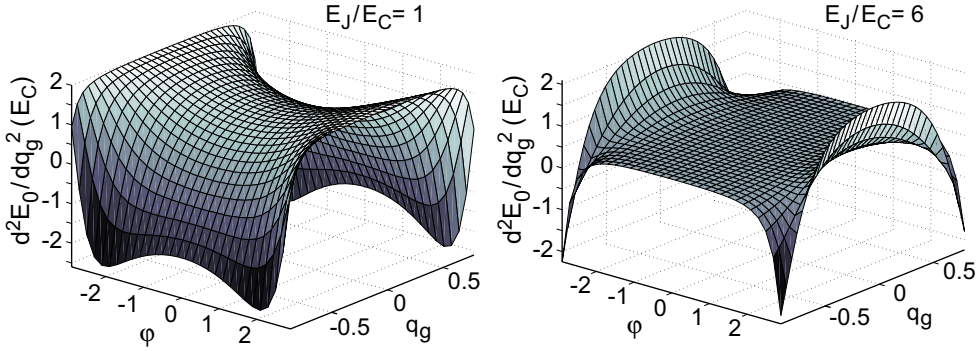

Figure 6.1: Second derivative with respect to q_g of the SCPT 1st band, at $E_J/E_C = 1$ (left) and $E_J/E_C = 6$ (right). The axes have been truncated just before $q_g = \pm 1$ and $\varphi = \pm\pi$ to remove divergencies. Compare with Fig. 5.2.

We begin by considering the dependence of the second derivative with respect to gate charge, on both of the external parameters, see Fig. 6.1. As evident, the observable capacitance has quite a strong dependence on both

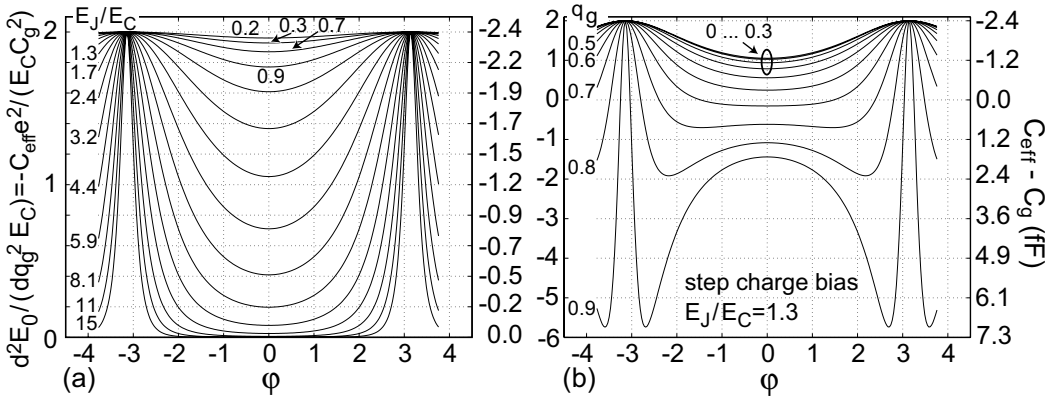

Figure 6.2: Second derivative with respect to gate charge of the SCPT 1st band *(left scales)*: (a) at different E_J/E_C, without charge bias ($q_g = 0$); (b) at fixed $E_J/E_C = 1.27$, but now stepping the charge bias. The *right scales* are the observable capacitance $C_{\rm eff} - C_g$, computed for illustration using: $C_g = 1.5$ fF, $E_C = 1$ K.

control parameters if $E_J/E_C > 1$. It is also important to note that close to $q_g = \pm 1$, the capacitance even changes sign.

Modulation of the observable capacitance, Eq. (6.4), is displayed in Fig. 6.2 (the constant term $-C_g$ was dropped). It may be useful to compare Figs. 6.2 (a) and 5.3 (a).

6.1 CSET

Since the input capacitance of an SCPT has a strong dependence on source-drain phase difference φ, this dependence could be used for phase detection. The device proposal, somewhat dual to the L-SET, is presented in [P9] . Here we derive formulas for its detector performance, taking into account that we are now using a notation different from that in [P9] for both E_J/E_C ratio and the gate charge. The correspondence is: $E_J \triangleq E_J/2$, $E_C \triangleq E_{CP}/4$, $E_J/E_C \triangleq 2E_J/E_{CP}$, between the present notation and that of [P9] , respectively.

The most important figure of merit is the transfer function which tells the change of observable capacitance, Eq. (6.4), per a unit change of phase. We aim at defining a dimensionless transfer function, or "gain" g_m which indicates the linearized relative modulation of the quantity (here the capacitance) per one period of the control parameter (phase). Here we denote directly its maximum value versus gate by g_m. From Eq. (6.4) we have

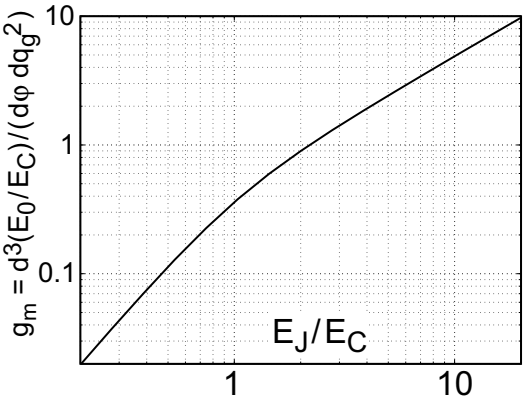

Figure 6.3: Normalized gain g_m of the CSET phase detector, see Eq. (6.5).

$$\frac{\partial C_{\text{eff}}}{\partial \varphi} = \frac{C_g^2 E_C}{e^2} \frac{\partial^3 (E_0/E_C)}{\partial \varphi \partial q_g^2} = \frac{C_g^2 E_C}{e^2} g_m \tag{6.5}$$

which serves as the definition of g_m (Fig. 6.3). By comparing Figs. 5.6 and 6.3, we see that the strength of capacitance modulation as a function of E_J/E_C behaves opposite to that of inductance modulation which decreases when E_J/E_C grows.

In the following, we refer to the configuration of Fig. 1 in [P9] . The SCPT is coupled to a resonant circuit formed by an inductor L and a shunting capacitance C_0. The total capacitance is thus $C = C_0 + C_{\text{eff}}$, where typically $C_{\text{eff}} \ll C_0$ due to technological limitations. The capacitance modulation by $\Delta C = (\partial C_{\text{eff}}/\partial \varphi)\Delta\varphi$ in power units is defined as the information power:

$$P_i \simeq Q_L \left(\frac{\Delta C}{C}\right)^2 \frac{f_0 e^2 C}{2C_g^2}. \tag{6.6}$$

Note a subtle issue here: the values of Q_L and f_0 in Eq. (6.6) in general depend on each other. Therefore, we substitute Eq. (6.6) with their expressions. Using Eq. (6.5), $Q_L = \omega L/Z_0 = \sqrt{L/C}/Z_0$, and assuming $C \simeq C_0$ we obtain

$$P_i(\Delta\varphi) \simeq \frac{g_m^2 E_C^2 \Delta\varphi^2}{4\pi\, Z_0 e^2} \left(\frac{C_g}{C_0}\right)^2. \tag{6.7}$$

Phase sensitivity s_φ limited by system noise $s_N^2 = k_B T_N$ is

$$s_\varphi = \sqrt{\frac{s_N}{P_i(1\text{rad})}} = 2\sqrt{\pi} e \left(\frac{C_0}{C_g}\right) \frac{\sqrt{k_B T_N Z_0}}{g_m E_C} \simeq \frac{4\sqrt{\pi} C_0 \sqrt{k_B T_N Z_0}}{g_m e} \tag{6.8}$$

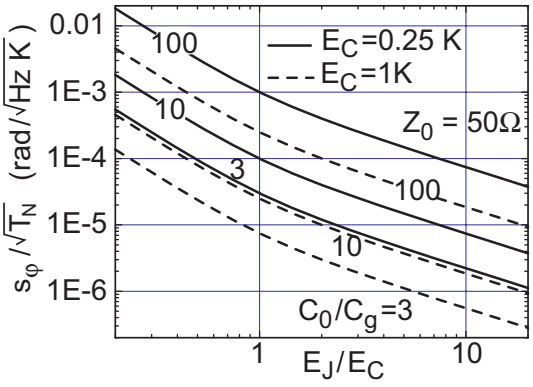

Figure 6.4: Phase sensitivity predicted for the CSET, Eq. (6.8), first form, for different capacitance ratios, and at two values of E_C.

where the last form of Eq. (6.8) follows from the assumption that at high E_J/E_C, charging energy is limited by the large gate capacitance ~ 2 fF. This is the ultimate limit with advanced junction fabrication (very thin oxide). The predicted phase sensitivity is plotted in Fig. 6.4.

6.2 Qubit proposal

Similarly to the discussion in Sec. 5.4.1 on how the two lowest energy bands E_0 and E_1 of the SCPT in the L-SET setup might constitute a qubit, these two SCPT bands might work as a qubit also in the CSET scheme. The CSET internal qubit would now be read through a capacitance measurement via gate. In analogy to Fig. 5.12, C_Q (and hence C_{eff}) has a substantial dependence on whether the qubit is $|0\rangle$ or $|1\rangle$. Capacitive measurements would offer the additional benefit of the possibility to use a higher E_J/E_C (more tolerance to $1/f$ [196]), and a stronger inductive shunting (similarly as in the original charge-phase qubit design).

Another possibility is to use the CSET as a separate detector to measure the state of the charge-phase qubit in the layout of Fig. 6.5. The procedure is discussed in detail in [P9] .

In the rest of this chapter, we will focus in some detail on decoherence in the setup of a separate qubit and a CSET detector, and show that the system may qualify even better as a qubit and detector than the original charge-phase qubit and its switching detector [135].

First of all, low power dissipation in the CSET detector means a low rate of quasiparticle generation, which is essential for low back-action and fast recovery from the measurement. Second, since the circuit is galvanically

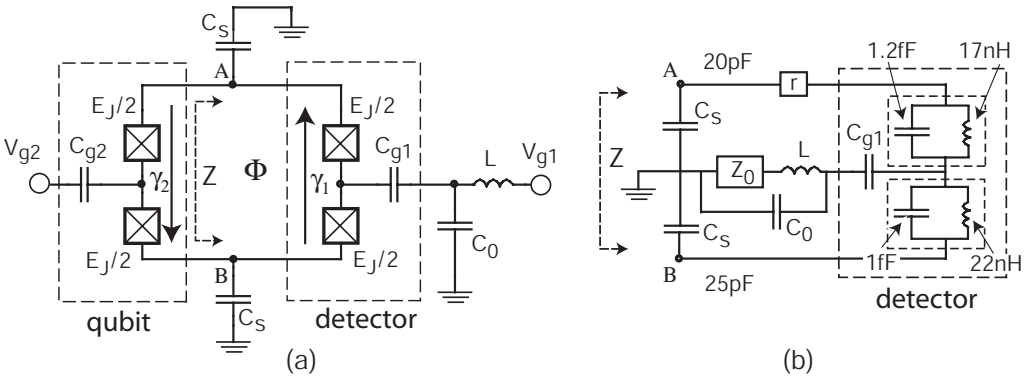

Figure 6.5: (a) CSET coupled to charge-phase qubit; (b) Illustration of the impedance Z seen by the qubit (between points A and B). The values are those used for calculating the impedances in Fig. 6.6.

isolated, it is free from external quasiparticle injection. Third, the system is fully symmetrized with respect to the SCPT island also on the detector side.

6.2.1 Dephasing and relaxation

Dephasing (rate Γ_φ) and relaxation (rate Γ_R) are caused by fluctuations in the control parameters q_g and φ. Their combined effect is to make quantum effects disappear at the decoherence rate

$$\Gamma_D = \Gamma_\varphi + \Gamma_R/2. \tag{6.9}$$

Either Γ_φ or Γ_R can thus be the bottleneck.

While qubit readout is off, decoherence comes from three primary sources: (1) qubit gate lead; (2) qubit source-drain circuit; (3) $1/f$ background charge noise. As we will argue below, each of these except (3) are negligible in the proposed design of a separate qubit and CSET measuring device.

The effect of the qubit gate lead can be made as small as desired by reducing C_{g2}. This operation is not likely to have adverse side effects.

In order to analyze issue (2) above, let Z denote the impedance seen by the qubit between the points A and B in Fig. 6.5. The ultimate limit for coherence is then set by Johnson-Nyquist noise, having the power spectrum given by Eq. (5.38). For the single-junction Cooper-pair box [57], decoherence due to the Johnson-Nyquist noise coupling through the gate has been discussed widely in the literature (see, e.g., Refs. [127,153]). Now fluctuations couple transversely, to the phase φ, what makes these well-known formulas not directly applicable. Here we review and adopt the results derived in

Ref. [155]. The formulas hold strictly only in the limit $E_J \ll E_C$, but the error is not expected to be large in our case $E_J \sim E_C$.

Due to low-frequency noise, memory of the initial phase of a superposition state is lost at the dephasing rate Γ_φ

$$\Gamma_\varphi \simeq \frac{\mathrm{Re(Z(0))}}{32\pi R_K}\frac{k_B T}{\hbar}\sin^2(\Theta)\left[\sin^2\left(\frac{\varphi}{2}\right) + d^2\cos^2\left(\frac{\varphi}{2}\right)\right]. \tag{6.10}$$

At the relaxation rate Γ_R, Eq. (5.32), an excited state undergoes a transition into the ground state. Equations (5.32), (6.10) mean that a symmetric ($d = 0$) charge-phase qubit (here just a nickname for an SCPT), is decoupled from its environment to the first order at the degeneracy point $\varphi = 0$, $q_g = 1$ ($\Theta = \pi/2$). At this working point, we get the previously stated Eq. (5.33), and from Eq. (6.10):

$$\Gamma_\varphi \simeq \frac{d^2\mathrm{Re(Z(0))}}{32\pi R_K}\frac{k_B T}{\hbar}. \tag{6.11}$$

The quantity relevant for decoherence, Re(Z), is plotted in Fig. 6.6 as a function of frequency. The (small) resistance r in the loop is a model for radiative losses in the loop, in order to demonstrate that Re(Z) remains small even when making a worst case estimate. An attractive property of the proposed qubit design is apparent: Because of the symmetry of the circuit *on the detector side*, noise from Z_0 in the detector gate lead is only a common-mode signal. This is equivalent to that Re(Z) = 0 in a fully symmetrical case of similar detector junctions and the C_S's, and with $r = 0$.

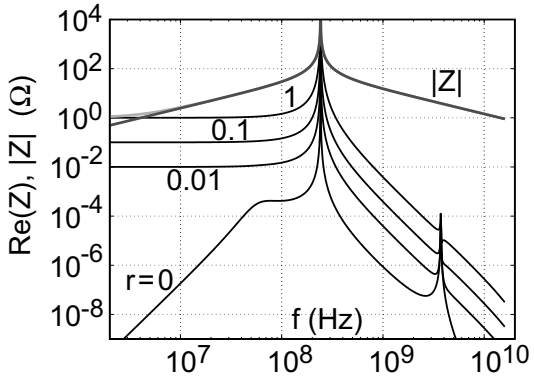

Figure 6.6: Re(Z) seen by the charge-phase qubit in the design of Fig. 6.5. $|Z|$ is also plotted for comparison (gray line). The curves are for different values for the supposed small resistance r in the loop.

Asymmetry of the whole structure weakens the noise protection property. However, as a check that even in a realistic case $\mathrm{Re}(Z)$ remains small, Fig. 6.6 was calculated assuming a randomly chosen 20 % asymmetry in the individual component values (the result was not sensitive to the choice made). Thereby, we conclude that $\mathrm{Re}(Z) \ll 1$ mΩ both at low frequency ($f < 1$ GHz) relevant for dephasing, and at the level-spacing frequency ($10 - 50$ GHz) relevant for relaxation, if $r = 0$. Even with a pessimistic choice for $r = 1\ \Omega$, we calculate from Eqs. (6.11) and (5.33), assuming a realistic $d = 0.1$, that both T_φ, $T_R > 1$ millisecond.

Therefore, decoherence is probably limited by $1/f$ background charge noise as often is the case with charge qubits [197–199]. This is the same noise observed ubiquitously in single-charge devices, and it typically has a spectrum

$$S_q(f) = \frac{e^2 k}{f} \tag{6.12}$$

where k is in the range $k \sim 10^{-6}...10^{-7}$ (Refs. [167–169]). Qubit coherence is then proportional to [199, 200]

$$\exp\left[-8\cos^2(\Theta)\left(\frac{E_C t}{\hbar}\right)^2 k \ln\left(\frac{\tau}{t}\right)\right], \tag{6.13}$$

where τ is the averaging time. Note that Eq. (6.13) is not an exponential decay. However, we see that at the degeneracy point ($\Theta = \pi/2$), coherence is lost roughly at a rate

$$\Gamma_{\varphi,1/f} \simeq \frac{\sqrt{8k}E_C\cos(\Theta)}{\hbar} \simeq \frac{2\sqrt{8k}}{\hbar}\frac{E_C^2}{E_J}\Delta q_g, \tag{6.14}$$

where for the last form we have used Eq. (4.15). Equation (6.14) yields $T_{\varphi,1/f} \sim 1\ \mu$s. Here we have assumed a reasonable accuracy $\Delta q_g = 0.01$ of gate charge adjustment from $q_g = 1$. This number can be significantly improved by using a higher E_J/E_C.

As a summary of this section, we conclude that the coherence time of the proposed qubit setup should not at least be inferior to the original charge-phase qubit. As compared to the Saclay design, the proposed setup offers the advantages of, first of all, non-dissipative readout, and also an even more symmetrized and galvanically fully isolated circuit.

Chapter 7

Summary and outlook

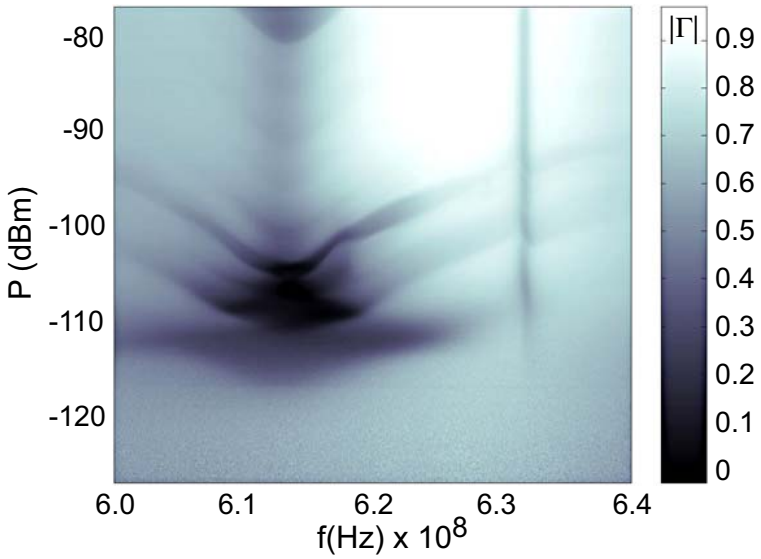

Figure 7.1: Frequency response of the L-SET (experimental data, sample B).

THIS work presents a study of a class of novel mesoscopic quantum effects, some of which even have quite an artistic appearance, see Fig. 7.1. The field is considered from the points of view of both basic and applied research, and methods of extremely sensitive measurements are introduced. The findings are particularly important for quantum computation with superconducting qubits. The concepts developed by the author may offer a solution for performing a delicate quantum measurement on the qubit. Presumably, quantum information will to some extent replace digital information in a distant future, in a manner much similar to how digital technology is presently replacing analog technology. This thesis may hence be viewed as a

contribution towards a "quantum information society".

In the field of basic research, the new procedures will be especially powerful in their own discipline, namely in the study of mesoscopic electron transport. At the most fundamental level of research, non-invasive quantum measurements are needed in testing the basic theories of physics that form the foundations of our world view. In particular, the interface between the microscopic quantum coherent world and our macroscopic world is not yet properly understood [201]. Quite soon hopefully, there will be experiments in this direction, such as the test of Bell inequalities [202–204] on the macroscopic scale.

One may also consider interdisciplinary applications. A scanning L-SET could be employed to probe the molecular electronic structure which has significance in biology, even in study of the mechanisms of life. Going further, one might speculate with the detection of gravitational radiation, or of charged elementary particles.

References

[1] E. Schrödinger, Naturwissenschaften **23**, 807 (1935).

[2] J. Bardeen, L. N. Cooper, and J. R. Schrieffer, Phys. Rev. **108**, 1175 (1957).

[3] B. D. Josephson, Phys. Lett. **1**, 251 (1962).

[4] R. Feynman, Intl. J. Theor. Phys. **21**, 467 (1982).

[5] Thin film Ni barrier resistors RN73 from Meggitt.

[6] A. B. Zorin, Rev. Sci. Instr. **66**, 4296 (1995).

[7] Spectrum Control, 51-353-007 (2 kHz), or 54-786-028 (100 kHz).

[8] Cable type: UT 085 SS SS; both inner and outer conductors are made of stainless steel.

[9] *LC* filters from Minicircuits, such as SLP1000 or SHP450.

[10] S. Ijima, Nature **354**, 56 (1991).

[11] R. Schoelkopf *et al.*, Science **280**, 1238 (1998).

[12] T. A. Fulton and G. J. Dolan, Phys. Rev. Lett. **59**, 109 (1987).

[13] D. M. Pozar, *Microwave engineering*, 1st ed. (Addison-Wesley, New York, 1990).

[14] A. Aassime *et al.*, Appl. Phys. Lett. **79**, 4031 (2001).

[15] G. J. Dolan, Appl. Phys. Lett. **31**, 337 (1977).

[16] J. Simmons, J. Appl. Phys. **34**, 1793 (1963).

[17] H. Brenning, S. Kubatkin, and P. Delsing, J. Appl. Phys. **96**, 6822 (2004).

[18] P. Delsing, T. Claeson, K. K. Likharev, and L. S. Kuzmin, Phys. Rev. B **42**, 7439 (1990).

[19] NP0 surface-mount capacitor from Philips Components.

[20] J. Aumentado, M. W. Keller, J. M. Martinis, and M. H. Devoret, Phys. Rev. Lett. **92**, 066802 (2004).

[21] R. B. Pettit and J. Silcox, Phys. Rev. B **13**, 2865 (1976).

[22] B. Abeles, R. W. Cohen, and G. W. Gullen, Phys. Rev. Lett. **17**, 632 (1966).

[23] R. W. Cohen and B. Abeles, Phys. Rev. **168**, 168 (1968).

[24] J. P. Pekola, K. P. Hirvi, J. P. Kauppinen, and M. A. Paalanen, Phys. Rev. Lett. **73**, 2903 (1994).

[25] S. Gueron *et al.*, Phys. Rev. Lett. **77**, 3025 (1996).

[26] K. Matsumoto *et al.*, Jpn. J. Appl. Phys. **34**, 1387 (1995).

[27] B. Irmer, M. Kehrle, H. Lorenz, and J. P. Kotthaus, Appl. Phys. Lett. **71**, 1733 (1997).

[28] I. Giaever, Phys. Rev. Lett. **5**, 147 (1960).

[29] V. T. Petrashov, V. N. Antonov, S. V. Maksinov, and R. S. Shaikhaidarov, Phys. Rev. B **59**, 551 (1994).

[30] M. Giroud *et al.*, Phys. Rev. B **58**, 872 (1998).

[31] T. Heikkilä, personal communication.

[32] K. D. Usadel, Phys. Rev. Lett. **25**, 507 (1970).

[33] W. Belzig *et al.*, Superlattices Microstruct. **25**, 1251 (1999).

[34] H. Chen and S. M. Heald, J. Appl. Phys. **66**, 1793 (1989).

[35] D. Gupta, D. R. Campbell, and P. S. Ho, *Thin Films - Interdiffusion and Reactions* (Wiley, New York, 1978).

[36] I. O. Kulik, Sov. Phys. JETP **30**, 944 (1970).

[37] P. H. Bagwell, Phys. Rev. B **46**, 573 (1992).

[38] S. Shapiro, Phys. Rev. Lett. **11**, 80 (1963).

[39] A. Barone and G. Paterno, *Physics and applications of the Josephson effect* (Wiley, New York, 1982).

[40] K. K. Likharev, *Dynamics of Josephson Junctions and Circuits* (Gordon and Breach, New York, 1986).

[41] M. Tinkham, *Introduction to Superconductivity* (McGraw-Hill, New York, 1996).

[42] A. J. Dahm *et al.*, Phys. Rev. Lett. **20**, 859 (1968).

[43] D. A. Vincent and B. S. Deaver, Phys. Rev. Lett. **32**, 212 (1974).

[44] R. Rifkin and B. S. Deaver, Phys. Rev. B **13**, 3894 (1976).

[45] T. Fulton and L. Dunkleberger, Phys. Rev. B **9**, 4760 (1974).

[46] M. H. Devoret, J. M. Martinis, D. Esteve, and J. Clarke, Phys. Rev. Lett. **53**, 1260 (1984).

[47] R. Kautz and J. Martinis, Phys. Rev. B **42**, 9903 (1990).

[48] A. O. Caldeira and A. J. Leggett, Ann. Phys. **149**, 374 (1983).

[49] J. Clarke *et al.*, Science **239**, 992 (1988).

[50] R. T. Voss and R. A. Webb, Phys. Rev. Lett. **47**, 265 (1981).

[51] L. D. Jackel *et al.*, Phys. Rev. Lett. **47**, 697 (1981).

[52] R. H. Koch, D. J. V. Harlingen, and J. Clarke, Phys. Rev. Lett. **47**, 1216 (1981).

[53] J. M. Martinis, M. H. Devoret, and J. Clarke, Phys. Rev. Lett. **55**, 1543 (1985).

[54] J. M. Martinis, M. H. Devoret, and J. Clarke, Phys. Rev. B **35**, 4682 (1987).

[55] T. M. Eiles and J. M. Martinis, Phys. Rev. B **50**, 627 (1994).

[56] D. J. Flees, S. Han, and J. E. Lukens, Phys. Rev. Lett. **78**, 4817 (1997).

[57] V. Bouchiat *et al.*, Physica Scripta **76**, 165 (1998).

[58] D. V. Averin and K. K. Likharev, in *Mesoscopic Phenomena in Solids*, edited by B. L. Altshuler, P. A. Lee, and R. A. Webb (Elsevier, Amsterdam, 1991), p. 173.

[59] Y. Nakamura, Y. A. Pashkin, and J. S. Tsai, Nature **398**, 786 (1999).

[60] M. A. Nielsen and I. L. Chuang, *Quantum computing and quantum information* (Cambridge University Press, Cambridge, 2000).

[61] P. W. Anderson, in *Lectures in the Many Body Problem*, edited by E. Caianello (Academic, New York, 1964), p. 3.

[62] V. Ambegaokar, U. Eckern, and G. Schön, Phys. Rev. Lett. **48**, 1745 (1982).

[63] M. Iansiti *et al.*, Phys. Rev. Lett. **59**, 489 (1987).

[64] M. Iansiti, A. T. Johnson, C. J. Lobb, and M. Tinkham, Phys. Rev. Lett. **60**, 2414 (1988).

[65] L. J. Geerligs *et al.*, Phys. Rev. Lett. **63**, 326 (1989).

[66] K. Likharev and A. Zorin, J. Low. Temp. Phys. **59**, 347 (1985).

[67] D. V. Averin, A. B. Zorin, and K. Likharev, Sov. Phys. JETP **61**, 407 (1985).

[68] E. Mathieu, J. Math. Pure Appl. **13**, 137 (1868).

[69] P. Joyez *et al.*, Phys. Rev. Lett. **72**, 2458 (1994).

[70] P. Joyez, Ph.D. thesis, l'Universite Paris 6, Saclay, Paris, 1995.

[71] M. Born and R. Oppenheimer, Ann. Phys. **84**, 457 (1927).

[72] V. Bouchiat, Ph.D. thesis, CEA-Saclay, 1997.

[73] Y. Nakamura, C. D. Chen, and J. S. Tsai, Phys. Rev. Lett. **79**, 2328 (1997).

[74] J. R. Friedman *et al.*, Nature **406**, 43 (2000).

[75] C. H. van der Wal *et al.*, Science **290**, 773 (2000).

[76] S. M. Girvin *et al.*, Phys. Rev. Lett. **64**, 3183 (1990).

[77] M. H. Devoret *et al.*, Phys. Rev. Lett. **64**, 1824 (1990).

[78] G. Ingold and Y. Nazarov, in *Single Charge Tunneling*, edited by H. Grabert and M. Devoret (Plenum Press, New York, 1992).

[79] T. Holst, D. Esteve, C. Urbina, and M. H. Devoret, Phys. Rev. Lett. **73**, 3455 (1994).

[80] G.-L. Ingold and H. Grabert, Europhys. Lett. **14**, 371 (1991).

[81] A. Schmid, Phys. Rev. Lett. **51**, 1506 (1983).

[82] L. S. Kuzmin *et al.*, Phys. Rev. Lett. **67**, 1161 (1991).

[83] J. S. Penttilä *et al.*, Phys. Rev. Lett. **82**, 1004 (1999).

[84] D. Averin and K. Likharev, J. Low. Temp. Phys. **62**, 345 (1986).

[85] J. Hassel and H. Seppä, IEEE Trans. Appl. Supercond. **11**, 260 (2001).

[86] J. Delahaye *et al.*, Physica E **18**, 15 (2003).

[87] J. Hassel, H. Seppä, J. Delahaye, and P. Hakonen, J. Appl. Phys. **95**, 8059 (2004).

[88] J. Hassel, Ph.D. thesis, VTT Information Technology, 2004.

[89] M. H. Devoret and R. J. Schoelkopf, Nature **406**, 1039 (2000).

[90] T. Ryhänen, H. Seppä, R. Ilmoniemi, and J. Knuuttila, J. Low Temp. Phys. **76**, 287 (1989).

[91] G. Schön and A. Zaikin, Phys. Rep. **198**, 237 (1990).

[92] J. Delahaye *et al.*, J. Phys. Soc. Jpn. **72**, 187 (2003).

[93] B. Reulet, J. Senzier, and D. Prober, Phys. Rev. Lett. **91**, 196601 (2003).

[94] J. Tobiska and Y. V. Nazarov, Phys. Rev. Lett. **93**, 106801 (2004).

[95] J. P. Pekola, Phys. Rev. Lett. **93**, 206601 (2004).

[96] Y. M. Blanter and M. Büttiker, Phys. Rep. **336**, 1 (2000).

[97] J. Delahaye *et al.*, cond-mat/0209076 (2002).

[98] E. B. Sonin, Phys. Rev. B **70**, 140506 (2004).

[99] C. Zener, Proc. R. Soc. London, Ser. A **137**, 696 (1932).

[100] L. D. Landau and E. M. Lifshitz, *Quantum Mechanics* (Pergamon Press, Oxford, 1976).

[101] P. K. Hansma, J. Appl. Phys. **44**, 4191 (1973).

[102] D. Pascal and M. Sauzade, J. Appl. Phys. **45**, 3085 (1974).

[103] R. Rifkin, D. A. Vincent, and B. S. Deaver, J. Appl. Phys. **47**, 2645 (1976).

[104] O. H. Soerensen, J. Appl. Phys. **47**, 5030 (1976).

[105] S. N. Erné, H.-D. Hahlbohm, and H. Lübbig, J. Appl. Phys. **47**, 5440 (1976).

[106] A. B. Zorin, Phys. Rev. Lett. **76**, 4408 (1996).

[107] P. Ågren, J. Walter, and D. B. Haviland, Phys. Rev. B **66**, 014510 (2002).

[108] W. C. Stewart, Appl. Phys. Lett. **12**, 277 (1968).

[109] D. E. McCumber, J. Appl. Phys. **39**, 3133 (1968).

[110] I. Siddiqi *et al.*, cond-mat/0312553.

[111] I. Siddiqi *et al.*, Phys. Rev. Lett. **93**, 207002 (2004).

[112] A. Korotkov, D. Averin, K. Likharev, and S. Vasenko, in *Single-Electron Tunneling and Mesoscopic Devices*, edited by H. Koch and H. Lübbig (Springer-Verlag, Berlin, 1992).

[113] A. N. Korotkov, Appl. Phys. Lett. **69**, 2593 (1996).

[114] A. N. Korotkov and M. A. Paalanen, Appl. Phys. Lett. **74**, 4052 (1999).

[115] L. Roschier *et al.*, J. Appl. Phys. **95**, 1274 (2004).

[116] D. Kajfez, *Q Factor* (Vector Fields, Oxford, 1994).

[117] M. T. Tuominen, J. M. Hergenrother, T. S. Tighe, and M. Tinkham, Phys. Rev. Lett. **69**, 1997 (1992).

[118] P. Lafarge *et al.*, Phys. Rev. Lett. **70**, 994 (1993).

[119] V. O. Turin and A. N. Korotkov, Appl. Phys. Lett. **83**, 2898 (2003).

[120] A. B. Pavolotsky *et al.*, J. Vac. Sci. Technol. B **17**, 230 (1999).

[121] P. Dubos *et al.*, J. Vac. Sci. Technol. B **18**, 122 (2000).

[122] N. Kim *et al.*, J. Vac. Sci. Technol. B **20**, 386 (2002).

[123] N. Wadefalk *et al.*, IEEE Trans. Microwave Theory Tech. **51**, 1705 (2003).

[124] M. Mück *et al.*, Appl. Phys. Lett. **72**, 2885 (1998).

[125] M.-O. André *et al.*, Appl. Phys. Lett. **75**, 698 (1999).

[126] M. Mück, J. B. Kycia, and J. Clarke, Appl. Phys. Lett. **78**, 967 (2001).

[127] A. Shnirman, G. Schön, and Z. Hermon, Phys. Rev. Lett. **79**, 2371 (1997).

[128] D. V. Averin, Solid State Commun. **105**, 659 (1998).

[129] Y. Makhlin, G. Schön, and A. Shnirman, Nature **398**, 305 (1999).

[130] J. E. Mooij *et al.*, Science **285**, 1036 (1999).

[131] T. P. Orlando *et al.*, Phys. Rev. B **60**, 15398 (1999).

[132] L. B. Ioffe *et al.*, Nature **398**, 679 (1999).

[133] A. Zazunov *et al.*, Phys. Rev. Lett. **90**, 087003 (2003).

[134] M. V. Feigel'man *et al.*, Phys. Rev. Lett. **92**, 098301 (2004).

[135] D. Vion *et al.*, Science **296**, 886 (2002).

[136] Y. Yu *et al.*, Science **296**, 889 (2002).

[137] J. M. Martinis, S. Nam, J. Aumentado, and C. Urbina, Phys. Rev. Lett. **89**, 117901 (2002).

[138] I. Chiorescu, Y. Nakamura, C. J. Harmans, and J. E. Mooij, Science **299**, 1869 (2003).

[139] E. Il'ichev *et al.*, Phys. Rev. Lett. **91**, 097906 (2003).

[140] T. Duty, D. Gunnarsson, K. Bladh, and P. Delsing, Phys. Rev. B **69**, 140503 (2004).

[141] T. Yamamoto *et al.*, Nature **425**, 941 (2003).

[142] I. Chiorescu *et al.*, Nature **431**, 159 (2004).

[143] A. Wallraff *et al.*, Nature **431**, 162 (2004).

[144] K. B. Cooper *et al.*, Phys. Rev. Lett. **93**, 180401 (2004).

[145] A. B. Zorin, Physica C **368**, 284 (2002).

[146] K. M. Lang *et al.*, IEEE Trans. Appl. Supercond. **13**, 989 (2003).

[147] J. Männik and J. E. Lukens, Phys. Rev. Lett. **92**, 057004 (2004).

[148] C. M. Caves *et al.*, Rev. Mod. Phys. **52**, 341 (1980).

[149] V. B. Braginsky and F. Y. Khalili, *Quantum Measurement* (Cambridge University Press, Cambridge, 1992).

[150] V. B. Braginsky and F. Y. Khalili, Rev. Mod. Phys. **68**, 1 (1996).

[151] D. V. Averin, Phys. Rev. Lett. **88**, 207901 (2002).

[152] A. J. Leggett *et al.*, Rev. Mod. Phys. **59**, 1 (1987).

[153] Y. Makhlin, G. Schön, and A. Shnirman, Rev. Mod. Phys. **73**, 357 (2001).

[154] R. J. Schoelkopf *et al.*, in *Quantum Noise*, edited by Y. V. Nazarov and Y. M. Blanter (Kluwer Academic, Dordrecht, 2003).

[155] A. Cottet, Ph.D. thesis, CEA-Saclay, 2003.

[156] R. Fazio, F. W. J. Hekking, and J. P. Pekola, Phys. Rev. B **68**, 054510 (2003).

[157] A. B. Zorin, Phys. Rev. Lett. **86**, 3388 (2001).

[158] H. B. Callen and T. A. Welton, Phys. Rev. **83**, 34 (1951).

[159] A. Aassime *et al.*, Phys. Rev. Lett. **86**, 3376 (2001).

[160] A. Käck, G. Wendin, and G. Johansson, Phys. Rev. B **67**, 035301 (2003).

[161] V. V. Danilov, K. K. Likharev, and A. B. Zorin, IEEE Trans. Magn. **19**, 572 (1983).

[162] C. M. Caves, Phys. Rev. D **26**, 1817 (1982).

[163] R. F. Voss, Appl. Phys. Lett. **38**, 182 (1981).

[164] R. H. Koch, D. J. V. Harlingen, and J. Clarke, Appl. Phys. Lett. **38**, 380 (1981).

[165] A. Shnirman and G. Schön, Phys. Rev. B **57**, 15400 (1998).

[166] M. Sillanpää, J. Penttilä, M. Paalanen, and P. Hakonen, Physica B **284-288**, 1826 (2000).

[167] G. Zimmerli, T. Eiles, R. Kautz, and J. Martinis, Appl. Phys. Lett. **61**, 237 (1992).

[168] V. Krupenin *et al.*, J. Appl. Phys. **84**, 3212 (1998).

[169] B. Starmark *et al.*, J. Appl. Phys. **86**, 2132 (1999).

[170] B. A. Huberman, J. P. Crutchfield, and N. H. Packard, Appl. Phys. Lett. **37**, 750 (1980).

[171] R. F. Miracky, J. Clarke, and R. H. Koch, Phys. Rev. Lett. **50**, 856 (1983).

[172] R. K. Ritala and M. M. Salomaa, Phys. Rev. B **29**, 6143 (1984).

[173] A. H. Silver and J. E. Zimmerman, Phys. Rev. **157**, 317 (1967).

[174] L. A. Blackwell, *Semiconductor-diode parametric amplifiers* (Prentice-Hall, Englewood Cliffs, 1961).

[175] P. Penfield, *Varactor applications* (M.I.T. Press, Cambridge, 1962).

[176] K. K. Chang, *Parametric and tunnel diodes* (Prentice-Hall, Englewood Cliffs, 1964).

[177] R. Movshovich *et al.*, Phys. Rev. Lett. **65**, 1419 (1990).

[178] B. Yurke *et al.*, Phys. Rev. A **39**, 2519 (1989).

[179] H. Zimmer, Appl. Phys. Lett. **19**, 515 (1971).

[180] P. L. Richards, in *SQUID '76*, edited by H. D. Hallbohm and H. Lubbig (de Gruyter, Berlin, 1977).

[181] N. F. Pedersen, in *SQUID '80*, edited by H. D. Hallbohm and H. Lubbig (de Gruyter, Berlin, 1980).

[182] B. Yurke, J. Opt. Soc. Am. B **4**, 1551 (1987).

[183] B. Yurke *et al.*, Phys. Rev. Lett. **60**, 764 (1988).

[184] M. Jeffery and E. Goto, J. Appl. Phys. **75**, 7550 (1994).

[185] L. J. Geerligs, V. F. Anderegg, J. Romijn, and J. E. Mooij, Phys. Rev. Lett. **65**, 377 (1990).

[186] J. M. Hergenrother, Ph.D. thesis, Harvard University, 1995.

[187] M. Tinkham, J. M. Hergenrother, and J. G. Lu, Phys. Rev. B **51**, 12649 (1995).

[188] J. G. Lu, J. M. Hergenrother, and M. Tinkham, Phys. Rev. B **53**, 3543 (1996).

[189] A. Fujiwara, Y. Takahashi, K. Murase, and M. Tabe, Appl. Phys. Lett. **67**, 2957 (1995).

[190] T. Fujisawa *et al.*, Appl. Phys. Lett. **84**, 2343 (2004).

[191] O. Astafiev *et al.*, Phys. Rev. B **69**, 180507 (2004).

[192] M. V. Berry, Proc. R. Soc. Lond. A **392**, 45 (1984).

[193] J. P. Pekola *et al.*, Phys. Rev. B **60**, 9931 (1999).

[194] G. Falci *et al.*, Nature **407**, 355 (2000).

[195] D. V. Averin and C. Bruder, Phys. Rev. Lett. **91**, 057003 (2003).

[196] A. Cottet *et al.*, Physica C **367**, 197 (2002).

[197] Y. Nakamura, Y. A. Pashkin, T. Yamamoto, and J. S. Tsai, Phys. Rev. Lett. **88**, 047901 (2002).

[198] E. Paladino, L. Faoro, G. Falci, and R. Fazio, Phys. Rev. Lett. **88**, 228304 (2002).

[199] A. Shnirman, Y. Makhlin, and G. Schön, Physica Scripta **T102**, 147 (2002).

[200] A. Cottet *et al.*, in *Macroscopic Quantum Coherence and Quantum Computing*, edited by D. V. Averin, B. Ruggiero, and P. Silvestrini (Kluwer/Plenum, New York, 2001), p. 111.

[201] W. H. Zurek, Rev. Mod. Phys. **75**, 715 (2003).

[202] A. Einstein, B. Podolsky, and N. Rosen, Phys. Rev. **47**, 777 (1935).

[203] J. S. Bell, Physics **1**, 195 (1964).

[204] A. Aspect, J. Dalibard, and G. Roger, Phys. Rev. Lett. **49**, 1804 (1982).

Abstracts of publications

[P1] We study the electronic density of states in a mesoscopic superconductor near a transparent interface with a ferromagnetic metal. In our tunnel spectroscopy experiment, a substantial density of states is observed at sub-gap energies close to a ferromagnet. We compare our data with detailed calculations based on the Usadel equation, where the effect of the ferromagnet is treated as an effective boundary condition. We achieve an excellent agreement with theory when non-ideal quality of of the interface is taken into account.

[P2] A new method to fabricate non-superconducting mesoscopic tunnel junctions by oxidation of Ti is presented. The fabrication process uses conventional electron beam lithography and shadow deposition through an organic resist mask. Superconductivity in Ti is suppressed by performing the deposition under a suitable background pressure. We demonstrate the method by making a single electron transistor which operated at $T < 0.4$ K and had a moderate charge noise of 2.5×10^{-3} $\mathrm{e}/\sqrt{\mathrm{Hz}}$ at 10 Hz. Based on nonlinearities in the current-voltage characteristics at higher voltages, we deduce the oxide barrier height of approximately 110 mV.

[P3] We used the band structure of a mesoscopic Josephson junction to construct low-noise amplifiers. By taking advantage of the quantum dynamics of a Josephson junction, i.e., the interplay of interlevel transitions and the Coulomb blockade of Cooper pairs, we created transistor-like devices, Bloch oscillating transistors, with considerable current gain and high-input impedance. In these transistors, the correlated supercurrent of Cooper pairs is controlled by a small base current made up of single electrons. Our devices reached current and power gains on the order of 30 and 5, respectively. The noise temperature was estimated to be around 1 Kelvin, but noise temperatures of less than 0.1 Kelvin can be realistically achieved. These devices provide quantum-electronic building blocks that will be useful at low temperatures in

low-noise circuit applications with an intermediate impedance level.

[P4] We have experimentally studied the energy levels of a mesoscopic superconducting quantum interference device (SQUID) using inelastic Cooper-pair tunneling. The tunneling in a small Josephson junction depends strongly on its electromagnetic environment. We use this fact to do energy-level spectroscopy of a SQUID loop by coupling it to a small junction. Our samples with strong quasiparticle dissipation are well described by a model of a particle localized in one of the dips in a cosine potential, while in the samples with weak dissipation we can see formation of energy bands.

[P5] We discuss the theory of the radio-frequency single-electron transistor and the measurements that use multiwalled carbon nanotubes as active elements. Our devices made of plasma-enhanced chemical-vapor-deposition nanotubes yield charge sensitivities of $10 - 20\ \mu e/\sqrt{\mathrm{Hz}}$.

[P6] We demonstrate a sensitive method of charge detection based on radio-frequency readout of the Josephson inductance of a superconducting single-electron transistor. Charge sensitivity $1.4 \times 10^{-4}\mathrm{e}/\sqrt{\mathrm{Hz}}$, limited by preamplifier, is achieved in an operation mode which takes advantage of the nonlinearity of the Josephson potential. Owing to reactive readout, our setup has more than two orders of magnitude lower dissipation than the existing method of radio-frequency electrometry. With an optimized sample, we expect uncoupled energy sensitivity below $\hbar$ in the same experimental scheme.

[P7] Using a classical equation of motion, dynamics of the phase is analyzed in the Inductive Single-Electron Transistor (L-SET) which is a promising new system suitable for quantum measurement with ultimate sensitivity and low back-action. In a regime of nonlinear dynamics, a shift of the oscillator resonant frequency is discovered which has a direct analogy to the switching of a dc-biased Josephson junction into voltage state. Results are reviewed for the predicted charge sensitivity, and it is shown that a performance challenging the best rf-SETs is foreseeable with the new device.

[P8] Phase dynamics has been measured in a driven mesoscopic Josephson oscillator where the resonance is tuned either by magnetic flux or by gate charge modulation of the Josephson inductance. Phenomena are analyzed in terms of a "phase particle picture", and by numerical circuit simulations. An analogy to switching of a DC-biased junction into voltage state is discussed. Operation principle of the recently demonstrated

Inductive Single-Electron Transistor (L-SET) based on the driven oscillator is reviewed. The obtained charge sensitivity implies that a performance comparable to the best rf-SETs has already been reached with the novel device.

[P9] We discuss how a single Cooper-pair transistor may be used to detect the superconducting phase difference by using the phase dependence of the input capacitance from gate to ground. The proposed device has a low power dissipation because its operation is in principle free from quasiparticle generation. According to the sensitivity estimates, the device may be used for efficient qubit readout in a galvanically isolated and symmetrized circuit.

[P10] We calculate the charge sensitivity of a recently demonstrated device where the Josephson inductance of a single Cooper-pair transistor is measured. We find that the intrinsic limit to detector performance is set by oscillator quantum noise. Sensitivity better than $10^{-6}\mathrm{e}/\sqrt{\mathrm{Hz}}$ is possible with a high Q-value $\sim 10^3$, or using a SQUID amplifier. The model is compared to experiment, where charge sensitivity $3 \times 10^{-5}\mathrm{e}/\sqrt{\mathrm{Hz}}$ and bandwidth 100 MHz are achieved.

[P11] We have investigated the influence of shot noise on the IV curves of a single mesoscopic Josephson junction. We observe a linear enhancement of zero-bias conductance of the Josephson junction with increasing shot-noise power. Moreover, the IV curves become increasingly asymmetric. Our analysis on the asymmetry shows that the Coulomb blockade of Cooper pairs is strongly influenced by the non-Gaussian character of the shot noise.